

**LABORATORY EXPERIMENTS ON COHESIVE SOIL
BED FLUIDIZATION BY WATER WAVES**

**PART I: RELATIONSHIP BETWEEN THE RATE OF BED
FLUIDIZATION AND THE RATE OF WAVE ENERGY DISSIPATION**

by

Jingzhi Feng and Ashish J. Mehta

**PART II: *IN-SITU* RHEOMETRY FOR DETERMINING THE
DYNAMIC RESPONSE OF BED**

by

David J.A. Williams and P. Rhodri Williams

December, 1992

REPORT DOCUMENTATION PAGE

1. Report No.		2.		3. Recipient's Accession No.	
4. Title and Subtitle LABORATORY EXPERIMENTS ON COHESIVE SOIL BED FLUIDIZATION BY WATER WAVES: PARTS I AND II				5. Report Date December, 1992	
7. Author(s) PART I: Jingzhi Feng and Ashish J. Mehta PART II: David J.A. Williams and P. Rhodri Williams				8. Performing Organization Report No. UFL/COEL-92/015	
9. Performing Organization Name and Address Coastal and Oceanographic Engineering Department University of Florida 336 Weil Hall Gainesville, FL 32611				10. Project/Task/Work Unit No.	
				11. Contract or Grant No. DACW39-90-K-0010	
12. Sponsoring Organization Name and Address U.S. Army Engineer Waterways Experiment Station 3909 Halls Ferry Road Vicksburg, MS 39180-6199				13. Type of Report Final	
				14.	
15. Supplementary Notes PART I: RELATIONSHIP BETWEEN THE RATE OF BED FLUIDIZATION AND THE RATE OF WAVE ENERGY DISSIPATION PART II: <i>IN-SITU</i> RHEOMETRY FOR DETERMINING THE DYNAMIC RESPONSE OF BED					
16. Abstract <p>A series of preliminary laboratory flume experiments were carried out to examine the time-dependent behavior of a cohesive soil bed subjected to progressive, monochromatic waves. The bed was an aqueous, 50/50 (by weight) mixture of a kaolinite and an attapulgite placed in a plexiglass trench. The nominal bed thickness was 16 cm with density ranging from 1170 to 1380 kg/m³, and water above was 16 to 20 cm deep. Waves of design height ranging from 2 to 8 cm and a nominal frequency of 1 Hz were run for durations up to 2970 min. Part I of this report describes experiments meant to examine the rate at which the bed became fluidized, and its relation to the rate of wave energy dissipation. Part II gives results on <i>in-situ</i> rheometry used to track the associated changes in bed rigidity.</p> <p>Temporal and spatial changes of the effective stress were measured during the course of wave action, and from these changes the bed fluidization rate was calculated. A wave-mud interaction model developed in a companion study was employed to calculate the rate of wave energy dissipation. The dependence of the rate of fluidization on the rate of energy dissipation was then explored.</p> <p>Fluidization, which seemingly proceeded down from the bed surface, occurred as a result of the loss of structural integrity of the soil matrix through a buildup of the excess pore pressure and the associated</p>					
17. Originator's Key Words Cohesive sediments Resuspension Energy dissipation Rheology Fluidization Rheometry Fluid mud Water waves Pore pressures				18. Availability Statement	
19. U. S. Security Classif. of the Report Unclassified		20. U. S. Security Classif. of This Page Unclassified		21. No. of Pages 148	22. Price

loss of effective stress. The rate of fluidization was typically greater at the beginning of wave action and apparently approached zero with time. This trend coincided with the approach of the rate of energy dissipation to a constant value. In general it was also observed that, for a given wave frequency, the larger the wave height the faster the rate of fluidization and thicker the fluid mud layer formed. On the other hand, increasing the time of bed consolidation prior to wave action decreased the fluidization rate due to greater bed rigidity. Upon cessation of wave action structural recovery followed.

Dynamic rigidity was measured by specially designed, *in situ* shearometers placed in the bed at appropriate elevations to determine the time-dependence of the storage and loss moduli, G' and G'' , of the viscoelastic clay mixture under 1 Hz waves. As the inter-particle bonds of the space-filling, bed material matrix weakened, the shear propagation velocity decreased measurably. Consequently, G' decreased and G'' increased as a transition from dynamically more elastic to more viscous response occurred. These preliminary experiments have demonstrated the validity of the particular rheometric technique used, and the critical need for synchronous, *in-situ* measurements of pore pressures and moduli characterizing bed rheology in studies on mud fluidization.

This study was supported by WES contract DACW39-90-K-0010.

LABORATORY EXPERIMENTS ON COHESIVE SOIL BED FLUIDIZATION BY
WATER WAVES

PART I: RELATIONSHIP BETWEEN THE RATE OF BED FLUIDIZATION AND
THE RATE OF WAVE ENERGY DISSIPATION

By

Jingzhi Feng and Ashish J. Mehta

PART II: *IN-SITU* RHEOMETRY FOR DETERMINING THE DYNAMIC RESPONSE
OF BED

By

David J.A. Williams and P. Rhodri Williams

SYNOPSIS

A series of preliminary laboratory flume experiments were carried out to examine the time-dependent behavior of a cohesive soil bed subjected to progressive, monochromatic waves. The bed was an aqueous, 50/50 (by weight) mixture of a kaolinite and an attapulgite placed in a plexiglass trench. The nominal bed thickness was 16 cm with density ranging from 1170 to 1380 kg/m³, and water above was 16 to 20 cm deep. Waves of design height ranging from 2 to 8 cm and a nominal frequency of 1 Hz were run for durations up to 2970 min. Part I of this report describes experiments meant to examine the rate at which the bed became fluidized, and its relation to the rate of wave energy dissipation. Part II gives results on *in-situ* rheometry used to track the associated changes in bed rigidity.

Temporal and spatial changes of the effective stress were measured during the course of wave action, and from these changes the bed fluidization rate was calculated. A wave-mud interaction model developed in a companion study was employed to calculate the rate of wave energy dissipation. The dependence of the rate of fluidization on the rate of energy dissipation was then explored.

Fluidization, which seemingly proceeded down from the bed surface, occurred as a result of the loss of structural integrity of the soil matrix through a buildup of the excess pore pressure and the associated loss of effective stress. The rate of fluidization was typically greater at the beginning of wave action and apparently approached zero with time. This trend coincided with the approach of the rate of energy dissipation to a constant value. In general it was also observed that, for a given wave frequency, the larger the wave height the faster the rate of fluidization and thicker the fluid mud layer formed. On the other hand, increasing the time of bed consolidation prior to wave action decreased the fluidization rate due to greater bed rigidity. Upon cessation of wave action structural recovery followed.

Dynamic rigidity was measured by specially designed, *in situ* shearometers placed in the bed at appropriate elevations to determine the time-dependence of the storage and loss moduli, G' and G'' , of the viscoelastic clay mixture under 1 Hz waves. As the inter-particle bonds of the space-filling, bed material matrix weakened, the shear propagation velocity decreased measurably. Consequently, G' decreased and G'' increased as a transition from dynamically more elastic to more viscous response occurred. These preliminary experiments have demonstrated the validity of the particular rheometric technique used, and the critical need for synchronous, *in-situ* measurements of pore pressures and moduli characterizing bed rheology in studies on mud fluidization.

This study was supported by WES contract DACW39-90-K-0010.

TABLE OF CONTENTS

SYNOPSIS	ii
PART I: RELATIONSHIP BETWEEN THE RATE OF BED FLUIDIZATION AND THE RATE OF WAVE ENERGY DISSIPATION	
LIST OF FIGURES	ii
LIST OF TABLES	v
CHAPTER	
1 INTRODUCTION	1
1.1 Brief Background	1
1.2 Objectives and Scope	2
1.3 Outline of Presentation	4
2 STUDY BACKGROUND AND METHODOLOGY	5
2.1 Fluid Mud Definition	5
2.2 Definition of Fluidization	7
2.3 Wave-induced Fluidization	10
2.4 Tasks	11
3 PRELIMINARY EXPERIMENTS	14
3.1 Sediment and Fluid Characterization	14
3.2 Rheological Experiments	19
3.2.1 Influence of Shear Rate	21
3.2.2 Influence of Shearing Time	30
3.2.3 Upper Bingham Yield Stress	31
3.2.4 Gelling	32
3.2.5 Summary	32
3.3 Instrumentation	33
3.3.1 Wave Gauges	33
3.3.2 Current Meter	34
3.3.3 Pressure Transducers	36
3.3.4 Data Acquisition System	37
3.4 Flume Characterization Tests	37
3.4.1 Test Conditions	43
3.4.2 Wave Spectra	46
3.4.3 Wave Reflection Estimation	46
3.4.4 Current Velocity	50

4	ESTIMATIONS OF FLUID MUD THICKNESS AND WAVE ENERGY DISSIPATION	53
4.1	Introduction	53
4.2	Effective Sheared Mud Thickness	53
4.3	Wave Energy Dissipation Rate	58
5	MUD BED FLUIDIZATION EXPERIMENTS	61
5.1	Test Conditions	61
5.2	Flume Data	63
5.2.1	Wave Time-series	63
5.2.2	Wave Spectra	64
5.2.3	Water/mud Interface	64
5.2.4	Density Measurement	64
5.2.5	Total and Pore Water Pressures	68
5.2.6	Bottom Pressure Gauge Data, Text # 9	70
5.2.7	Rms Pressure Amplitudes, Test #9	72
5.2.8	Pressure Recovery after End of Test	73
6	EXPERIMENTAL DATA ANALYSIS	76
6.1	Introduction	76
6.2	Wave-Mud Interaction Model Results	76
6.2.1	Wave Regime: Test Versus Model Conditions	76
6.2.2	Effective Sheared Mud Thickness	77
6.2.3	Wave Energy Dissipation	79
6.3	Flume Test Results	88
6.3.1	Effective Stress	88
6.3.2	Fluidized Mud Thickness	93
6.3.3	Rate of Fluidization	94
6.4	Comparison between Model Results and Experiments	98
6.4.1	Fluidized mud thickness, d_f , and Effective sheared mud thickness, d	98
6.4.2	Fluidization Rate as a Function of Wave Energy Dissipation Rate	100
7	CONCLUSIONS	104
7.1	Conclusions	104
7.2	Significance of the Study	105
	BIBLIOGRAPHY	107

PART II: *IN-SITU* RHEOMETRY FOR DETERMINING THE DYNAMIC RESPONSE OF BED

LIST OF FIGURES	ii
LIST OF TABLES	iii
CHAPTER	
1 INTRODUCTION	1
1.1 Preamble	1
1.2 Investigation	2
2 RHEOMETRY	3
2.1 <i>In-situ</i> Rheometry	3
2.2 Shear Wave Rig	4
2.3 Ancillary Equipment	5
2.4 Signal Processing and Data Analysis	6
3 THEORETICAL BASIS	7
3.1 Definitions of G' and G''	7
3.2 Shear Wave Velocity Determination	8
3.3 Voigt and Maxwell Models	10
4 EXPERIMENTAL CONSIDERATIONS	12
4.1 Materials	12
4.2 <i>In-situ</i> Rheometry	12
4.3 Shear Wave Velocities	12
5 FLUME EXPERIMENTS	16
5.1 Initial Condition	16
5.2 Preliminary Tests with 20 mm Water Waves	17
5.3 Tests with 40 mm Water Waves	17
5.4 Tests with 20 mm Water Waves	17
6 ANALYSIS AND DISCUSSION	19
6.1 Shear Wave Velocity	19
6.2 Temporal Response of Bed in Terms of Model Parameters	21
6.3 Concluding Remarks	22
BIBLIOGRAPHY	24
APPENDIX: SOLUTION FOR $V/V(0)$	25

PART I: RELATIONSHIP BETWEEN THE RATE OF BED FLUIDIZATION AND
THE RATE OF WAVE ENERGY DISSIPATION

By

Jingzhi Feng and Ashish J. Mehta

LIST OF FIGURES

2.1	Schematic of water column with a muddy bottom in terms of vertical profiles of sediment density and velocity, and vertical sediment fluxes . .	6
2.2	Soil mass subjected to stress loading	8
2.3	Definition sketch of soil stress terminology	9
2.4	Fluidization process of a soil bed at a given elevation	10
2.5	Influence of waves on shear resistance to erosion of kaolinite beds in flumes	11
3.1	SEM of dry agglomerates of attapulgite. Scale $1cm = 10\mu m$	18
3.2	SEM of dry agglomerates of bentonite. Scale $1cm = 10\mu m$	18
3.3	SEM of dry agglomerates of kaolinite. Scale $1cm = 10\mu m$	19
3.4	Shear stress, σ , versus shear rate, $\dot{\gamma}$, (K,A,B)	22
3.5	Shear stress, σ , versus shear rate, $\dot{\gamma}$, (AK,BK,AB)	23
3.6	Shear stress, σ , versus shear rate, $\dot{\gamma}$, (K,KS,A,AS,B,BS)	24
3.7	Shear stress, σ , versus shear rate, $\dot{\gamma}$, (BK,BKS,AK,AKS,AB,ABS) . . .	25
3.8	Viscosity, μ , versus shear rate, $\dot{\gamma}$, (K,KS,A,AS,B,BS)	26
3.9	Viscosity, μ , versus shear rate, $\dot{\gamma}$, (BK,BKS,AK,AKS,AB,ABS)	27
3.10	Calibration curves for the wave gauges	35
3.11	Calibration curve for the current meter	35
3.12	Calibration curves for the total pressure gauges	38
3.13	Calibration curves for the pore pressure gauges	39
3.14	Dynamic response of pressure gauges, and comparison with results from the linear wave theory: gauge elevations ranging from 0 to 4.9 cm . . .	40

3.15	Dynamic response of pressure gauges, and comparison with results from the linear wave theory: gauge elevations ranging from 7.5 to 14 cm	41
3.16	Example of instrument drift, in pore pressure measurement, with old and new amplifiers. Gauge #2 was connected to the "new" amplifier. Comparison is made with gauge #3 response connected to the "old" amplifier	42
3.17	Example of instrument drift, pore pressure gauge #1, Time range over which most of the pressure data were obtained is indicated.	42
3.18	Wave flume elevation profile and instrument locations	44
3.19	Examples of wave time-series (depth=20cm, period=1.0s) for flume characterization tests with a false bottom	45
3.20	Wave spectra, water depth=20cm; average wave height ranging from 3.9 to 4.6 cm, period ranging from 1 to 2 sec.	47
3.21	Wave spectra, water depth=20cm; average wave height ranging from 6.4 to 9.1 cm, period ranging from 1 to 2 sec.	48
3.22	Horizontal velocity profiles: comparison between experimental data (rms amplitudes) and linear wave theory (period T=1.0s)	52
4.1	Two-layered water-fluid mud system subjected to progressive wave action	54
4.2	Diagram of calculation process for effective sheared mud thickness, d .	57
5.1	Sketch of flume profile in the fluidization experiment	62
5.2	Wave time-series, Test #9	65
5.3	Wave spectra, Test #9	67
5.4	Time-variation of water-mud interface along the flume, Test #9	68
5.5	Examples of density profiles, Test #9. Dashed line indicates interfacial elevation	69
5.6	Wave-averaged total and pore water pressures, Test #9	71
5.7	Total pressure at the bottom of the flume, Test #9	72
5.8	Root-mean square pore water pressure amplitudes, Test #9	74
5.9	Root-mean square total pressure amplitudes, Test #9	75
6.1	Effective sheared mud thickness, d , Tests #1 through #3	80
6.2	Effective sheared mud thickness, d , Tests #4 through #7	81

6.3	Effective sheared mud thickness, d , Tests #8 through #11	82
6.4	Wave dissipation rate, ϵ_D , versus time: Tests #1 through #3	84
6.5	Wave dissipation rate, ϵ_D , versus time: Tests #4 through #7. Design wave heights are from Table 5.1	85
6.6	Wave dissipation rate, ϵ_D , versus time: Tests #8 through #11. Design wave heights are from Table 5.1	86
6.7	ϵ_D , k_i and a_x^2 versus time: Tests #9	87
6.8	Effective stress, σ' , variations with time: Test #8	89
6.9	Effective stress, σ' , variations with time: Test #9	90
6.10	Effective stress, σ' , variations with time: Test #10	91
6.11	Effective stress, σ' , variations with time: Test #11	92
6.12	Bed elevation, water/mud interface, and fluidized mud thickness in Tests #8 through #11	95
6.13	Fluidized mud thickness, d_f , variations with time	96
6.14	Bed fluidization rate, $\partial H_b/\partial t$, versus time	99
6.15	Comparison between fluidized mud thickness, d_f , and effective sheared mud thickness, d	101
6.16	Wave energy dissipation rate, ϵ_D , versus time for tests #9 and #10.	102
6.17	Fluidization rate, $\partial H_b/\partial t$, versus wave energy dissipation rate, ϵ_D , tests #9 and #10. Dashed lines indicate extrapolations	103

LIST OF TABLES

3.1	Chemical composition of kaolinite	15
3.2	Chemical composition of bentonite	15
3.3	Chemical composition of attapulgite (palygorskite)	15
3.4	Chemical composition of tap water	15
3.5	Size distribution of kaolinite	16
3.6	Size distribution of bentonite	17
3.7	Size distribution of attapulgite	17
3.8	Selected muds (clays and clay mixtures) for rheological tests	20
3.9	Parameters for the Sisko power-law model for viscosity	30
3.10	Shearing time effect on shear stress	31
3.11	Upper Bingham yield stress	32
3.12	Rheological parameters for power-law given by Equation 3.4	34
3.13	Wave conditions for the characterization tests	46
3.14	Wave reflection coefficient, k_r	50
5.1	Summary of test conditions	63
5.2	Wave heights, Test #9	64
6.1	Parameters for determining the water wave condition	77
6.2	Input parameters for calculating the effective sheared mud thickness	79
6.3	Values of the (representative) constant effective sheared mud thickness, d_s , $\dot{\gamma}$ and μ	83
6.4	Representative values of the wave energy dissipation rate, ϵ_{D_s}	88
6.5	Effective stress, σ' , at the beginning and end of Test #9	91

6.6 Bed elevation and fluidized mud thickness at different times 97

CHAPTER 1 INTRODUCTION

1.1 Brief Background

The interaction between unsteady flows and very soft muddy bottoms, a key process in governing coastal and estuarine cohesive sediment transport, is not well understood at present. What is quite well known, however, is that oscillatory water motion, by "shaking" and "pumping," generates fluid mud which is a high concentration near-bed slurry having non-Newtonian rheological properties. This mud therefore becomes potentially available for transport by uni-directional currents. The precise mechanism by which fluid mud is formed by water wave motion over cohesive soil beds is of evident interest in understanding and interpreting the microfabric of flow-deposited fine sediments in shallow waters, and hence the erodibility of muddy beds due to hydrodynamic forcing. Results from preliminary laboratory tests in a wave flume by Ross (1988), using known soil mechanical principles, indicated that the fluidization process is perhaps even more significant in generating potentially transportable sediment than previously realized. It was therefore decided in the present study to extend this work of Ross to examine the inter-relationship between soil mechanical changes and wave energy input, and to understand the bed fluidization process through these changes under loading by progressive, non-breaking water waves.

Unlike the boundary of soil beds composed of cohesionless material (e.g., sand), the cohesive soil bed boundary is often poorly defined, as it is not evident, e.g., from echosounder data, at what depth the near-bed suspension ends and the soil bed begins. The marine cohesive soil bed is primarily composed of flocculated, fine-grained sediment with a particle-supported structured matrix, hence a measurable shear strength. On the other hand, fluidized mud is a suspension which by definition is essentially fluid-supported. Parker

(1986) noted ambiguities when lead lines, echo-sounders or nuclear transmission or back-catter gauges were used to identify the cohesive soil bed boundary below a fluid-supported, high concentration sediment slurry.

Many investigators have identified fluid mud slurry in terms of a range of bulk density of the sediment-fluid mixture. For example, Inglis and Allen (1957) defined fluid mud by the density range of 1.03-1.30 g/cm^3 , while Krone (1962) used a density range of 1.01-1.11 g/cm^3 to define fluid mud. Wells (1983) specified a density range of 1.03-1.30 g/cm^3 , Nichols (1985), 1.003-1.20 g/cm^3 , and Kendrick and Derbyshire (1985) 1.12-1.25 g/cm^3 as fluid mud. These ranges are not congruent in general. In fact, to provide a quantitative definition for fluid mud based on a discrete density range is not possible because the effect is not simply dependent on the density, but also on the flow condition and the sediment properties. Thus, Ross et al. (1987) noted that due to the dynamic nature of the cohesive bed boundary which responds significantly to hydrodynamic forcing, e.g., waves, the density of the suspension by itself cannot be used either to identify the cohesive bed boundary or the fluid mud layer which occurs immediately above this boundary. The fluidization of the cohesive soil bed, accompanied by measurable degradation in soil geotechnical properties, should in fact be quantified by measuring soil pressures since the bed is characterized by the occurrence of a measurable effective stress, while the overlying fluid has practically none (Ross et al., 1987). Therefore the zero effective stress plane defines the bed surface. Given these soil characteristics, and the desire to better understand the fluidization process under wave action, the following objectives and scope were set for the ensuing work.

1.2 Objectives and Scope

At the outset it is necessary to mention again the work of Ross (1988), who conducted flume tests using a Kaolinite estuarine sediment to study wave-induced cohesive soil bed fluidization. Total and pore water pressures were measured to obtain the effective stress, which in turn was used for tracking bed elevation change during the fluidization process, and fluid mud thickness determined from the bed elevation change. However, in his work

the wave dissipation rate during fluidization was not calculated; therefore the possibility of a dependence of the bed fluidization rate on the rate of wave energy dissipation could not be explored. Given this limitation of Ross's work, the objectives of this study were to simultaneously evaluate the effective stress response (via soil pressure measurement), and wave dissipative characteristics (through a hydrodynamic wave-mud interaction model), and from these to explore the relationship between the process of mud fluidization and wave energy input for selected cohesive soil beds subjected to progressive wave action in a laboratory flume. By way of this approach, several fundamental issues related to the manner in which the cohesive bed fluidizes were chosen to be examined. Specifically the following aspects were considered:

1. To measure total and pore pressure profiles in the mud as a function of time under different wave conditions, as well as the corresponding damping characteristics of the surface waves.
2. To measure changes in the effective stress within the mud, and to investigate the definition of the cohesive bed boundary based on tracking the zero (or near-zero) effective stress level.
3. To determine if any tangible relationship exists between the rate of the bed fluidization, bed consolidation time and the rate of wave energy dissipation.
4. To compare the measured fluidized layer thickness and the calculated effective sheared mud thickness (a chosen measure of fluid mud thickness) from a two layered hydrodynamic wave-mud interaction model.

To meet the above objectives, the scope of this research was selected to be as follows:

1. The investigation was limited to using commercial clays whose rheological properties could be relatively easily characterized.
2. Waves were restricted to regular (monochromatic), 1 Hz progressive and non-breaking type, while wave heights ranged from 2 to 8 cm.

3. Mud bed thickness was limited to 10 -20 cm. The water level was maintained to be 35 cm above the flume bottom in all cases.
4. Different consolidation periods, from one to ten days, for the mud beds were selected, the tests been limited to self-weight consolidation.
5. Tap water was used, and a 50/50 (by weight) mixture of attapulgite and kaolinite was used to prepare the bed for the fluidization tests.

1.3 Outline of Presentation

Chapter 2 reviews the definition and theory of fluidization of mud, and also gives the approach to this study. All preliminary experiments, including auxiliary tests involving on the rheological properties of selected muds, instrument calibration tests and flume characterization tests are presented in Chapter 3. The selected two-layered hydrodynamic wave-mud interaction model for calculating the rate of wave energy dissipation and the effective thickness of fluidized mud are described in Chapter 4. Chapter 5 presents the fluidization experiments including test conditions, wave data, total and pore water pressure data, elevations of water/mud interface, and mud density measurements. Data analysis and results are presented and discussed in Chapter 6. Chapter 7 concludes the presentation of the entire investigation.

CHAPTER 2 STUDY BACKGROUND AND METHODOLOGY

2.1 Fluid Mud Definition

As mentioned in Chapter 1, many investigators have identified fluid mud in terms of a range of bulk density of the sediment-fluid mixture. Since fluid mud properties depend on the physico-chemical properties of this mixture and the hydrodynamic settling, a unique density range cannot be defined appropriately on theoretical grounds, hence a definition that accounts for the dynamical effects can significantly assist in estimating, for example, the rate of advective mud transport.

It has been suggested that the fluid mud density range be preferably examined in conjunction with the corresponding horizontal velocity field (Ross et al., 1987). Figure 2.1 shows the various layered regimes resulting from cohesive bed response to waves, defined by the profiles of instantaneous vertical density (or concentration) and velocity amplitude, u_m (Mehta, 1989). The density profile has been idealized by indicating only two significant concentration gradients that categorize the water-mud system into three zones. The top zone, which is above the upper gradient, is a mobile, relatively low concentration suspension, which may be less than 1 g/l^{-1} , but can exceed $2\text{-}3 \text{ g/l}^{-1}$ during extreme energy events (Ross & Mehta, 1989). This suspension is practically a Newtonian fluid. The lower gradient defines the cohesive bed within which there is sufficient interparticle contact to result in a finite, measurable effective stress. Between the two concentration gradients there occurs a relatively high concentration layer (e.g., up to 200 g/l^{-1}) as fluid mud. As noted in Chapter 1 it is essentially a fluid-supported slurry with non-Newtonian rheological properties, typically appearing to conform to a pseudoplastic (shear thinning) or dilatant (shear thickening) description with respect to the stress-rate of strain relationship, depending upon

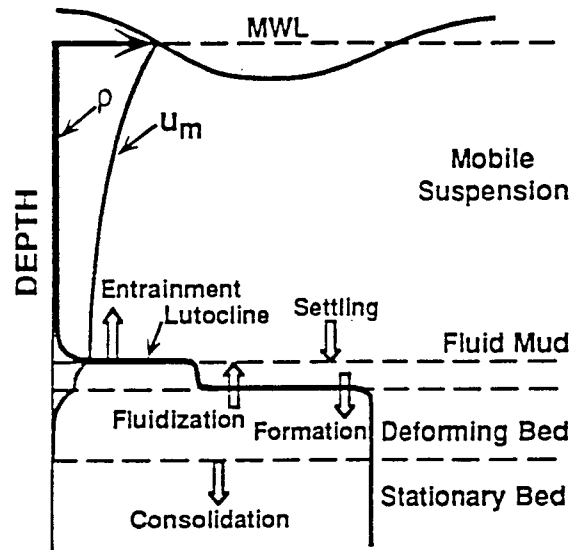


Figure 2.1: Schematic of water column with a muddy bottom in terms of vertical profiles of sediment density and velocity, and vertical sediment fluxes

mud composition, concentration, and the rate of shearing.

The fluid mud zone is of particular practical importance because this mud can be easily entrained and thereby substantially contribute to turbidity even under relatively low energy inputs, due to its high concentration and very weak internal structure (Ross, 1988). Fluid mud also plays a significant role in absorbing and dissipating turbulent kinetic energy, which can cause a transition from a typically visco-elastic response to a more viscous shear flow behavior. Depending on the time-history of the applied interfacial shear stress above the fluid mud layer, a finite depth limit of horizontal mobilization corresponding to a momentum diffusion layer within the fluid mud layer occurs. This limit defines the zero velocity interface which generally exists in the fluid mud layer but is not bounded by either the mobile suspension/fluid mud interface (or lutocline) or the fluid mud/bed interface. Under an oscillatory loading, e.g. water waves, the zero velocity elevation can extend well below the fluid mud/bed interface due to viscoelastic deformations in the cohesive soil bed.

There are three flux-related processes which define the sediment concentration profile: erosion, deposition, and bed consolidation. For cohesive sediments, however, such terms

as erosion and deposition are not always easily defined in an unequivocal sense. Thus, for example, fluidization of the cohesive soil bed and entrainment of fluid mud due to hydrodynamic forcing may both be thought of as erosion-type processes, while gravitational settling of sediment onto the lutocline (water-mud interface), as well as formation of the bed by dewatering of fluid mud, can be considered to be deposition-type phenomena (Mehta, 1989). These processes are shown in Figure 2.1.

2.2 Definition of Fluidization

Because of the different responses of the solid and the liquid phases to stress loading, it is necessary to consider each phase independently. The liquid phase is incompressible; under a differential compressive stress, however, it flows because a liquid, by definition, is not capable of resisting a shear load. Ultimately, the solid phase controls the resistance to compression and shear.

Consider a saturated soil mass cut along its surface, as shown in Figure 2.2, subjected to an applied average normal stress, σ . Imagine that the soil mass is cut along a surface so that a free-body diagram could be drawn. Suppose that this surface is approximately horizontal, but is wavy, so that it always passes between particles rather than through particles, as shown in the figure. Then the surface will pass through areas of solid-to-solid contact, and through void spaces filled with water. Let A_t be the total horizontal projection of the cutting surface for the soil mass considered, A_c the horizontal projection of the contact area between the solids lying in the cutting surface, and A_w be the horizontal projection of the portion of the cutting surface which passes through water. Then, by the requirement of the force balance in the vertical direction,

$$\sigma A_t = \sigma^* A_c + P_{pw} A_w \quad (2.1)$$

where σ^* is the actual intergranular stress at points of contact, and P_{pw} is the pressure in the water, i.e., pore water pressure. Or

$$\sigma = \frac{A_c}{A_t} \sigma^* + P_{pw} \frac{A_w}{A_t} \quad (2.2)$$

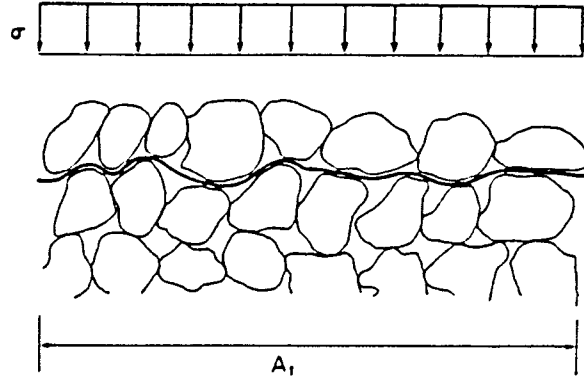


Figure 2.2: Soil mass subjected to stress loading

For soils A_c is very small, approaching zero (Sowers, 1979). Therefore, A_w approaches A_t , and σ^* must be very large. Thus

$$\sigma = \sigma^* \frac{A_c}{A_t} + P_{pw} \quad (2.3)$$

As noted by Perloff and Baron (1976), the product of $\sigma^* A_c$ must approach a finite limit corresponding to a constant intergranular force, even though σ^* is very large and A_c is very small. In fact, the first term on the right side of Equation 2.3 must be some measure of the average stress carried by the soil skeleton. It is called effective stress, σ' , defined by

$$\sigma' = \sigma^* \frac{A_c}{A_t} \quad (2.4)$$

Hence by measuring the total stress σ and pore water pressure P_{pw} , the effective stress at a point can be obtained from

$$\sigma' = \sigma - P_{pw} \quad (2.5)$$

which governs the mechanical behavior of soil. For example, a reduction in the effective stress can lead to a reduction in the soil strength and possibly the critical shear stress for erosion. Eventually if $\sigma' \rightarrow 0$, there is no contact between the soil particles and a zone of instability and potential failure is created.

Another important parameter is the excess pore pressure, Δu , which is the difference between actual pore water pressure, P_{pw} , and the hydrostatic pressure, P_h . Under dynamic

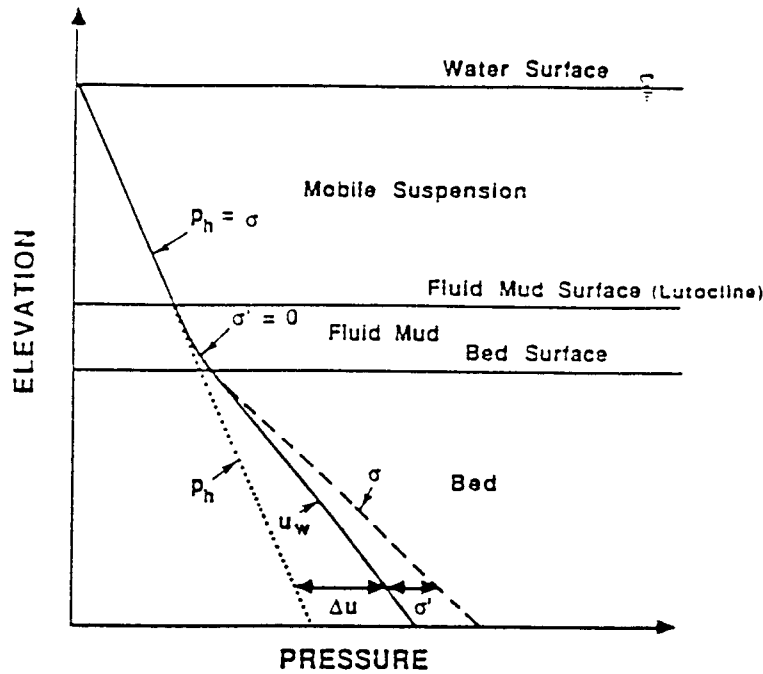


Figure 2.3: Definition sketch of soil stress terminology

conditions, if the sum of excess pore pressure, Δu , and the hydrostatic pressure, P_h , approaches the total stress, σ , i.e., $\Delta u + P_h \rightarrow \sigma$, fluidization occurs (Ross, 1988). Figure 2.3 is an idealized sketch of the stress profile corresponding to three-layered cohesive sediment concentration profile (see Figure 2.1). In the upper mobile suspension layer the total stress, σ , is equal to the hydrostatic pressure, P_h , within the suspension. In the fluid mud layer σ increases much more rapidly with depth due to higher sediment concentration, while the effective stress, σ' , is still zero. Finally, in the cohesive bed, structural integrity due to closely packed flocs results in a skeletal framework which partially self-supports the soil medium. The pore water pressure, P_{pw} , in the bed is equal to the hydrostatic pressure, P_h , plus the excess pore water pressure, Δu , which represents the component of the bed material not supported by the porous solid matrix.

Figure 2.4 shows the time changes of the pore water pressure, P_{pw} , at a given elevation, leading ultimately to bed fluidization, e.g. by wave action. At first, P_{pw} in the bed is equal to the hydrostatic pressure P_h , i.e. $\Delta u = 0$ (assuming this to be the initial condition). Then

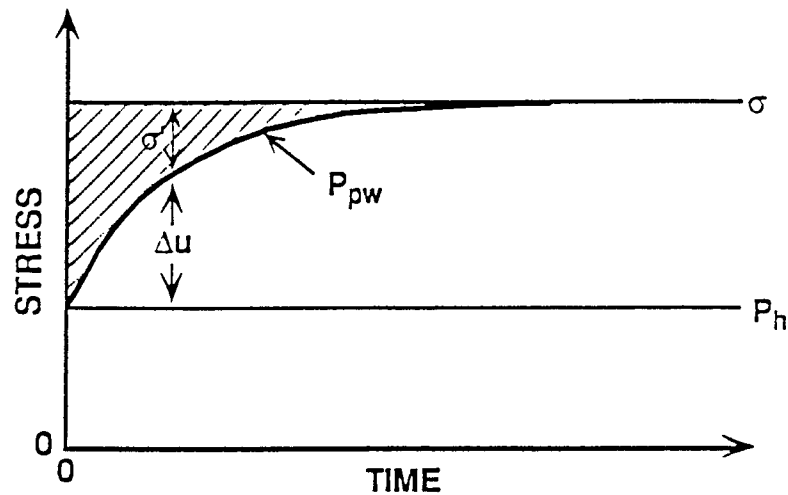


Figure 2.4: Fluidization process of a soil bed at a given elevation

under dynamic loading the excess pore water pressure, Δu , builds up and the effective stress σ' reduces gradually. When the pore water pressure P_{pw} equals the total pressure σ , the bed at this elevation is fluidized.

2.3 Wave-induced Fluidization

Surface waves and other highly oscillatory currents have a particularly pronounced influence on erosion in comparison with uni-directional currents. Because of the increased inertial forces associated with a local change in linear momentum, the net entrainment force is much greater than with turbulent uni-directional flows (Ross, 1988).¹ Also noteworthy is the effect that bed 'shaking' and 'pumping' can have under highly oscillatory flows. 'Shaking' or bed vibrations occur because of the oscillatory bed shear stress which is transmitted elastically (while at the same time damped) down through the bed. 'Pumping' occurs from oscillatory normal fluid pressure which, given the low permeability of cohesive soils, can lead to internal pore pressure build up and liquefaction (Ross, 1988). These effects can cause the dissipation of the effective stress in mud layers depending on the bed characteristics, thereby leading to mass erosion and fluid mud formation.

The example given in Figure 2.5 shows that resistance to bed erosion under waves was lower than that for a corresponding bed subjected to steady shear flow (Mehta, 1989). The

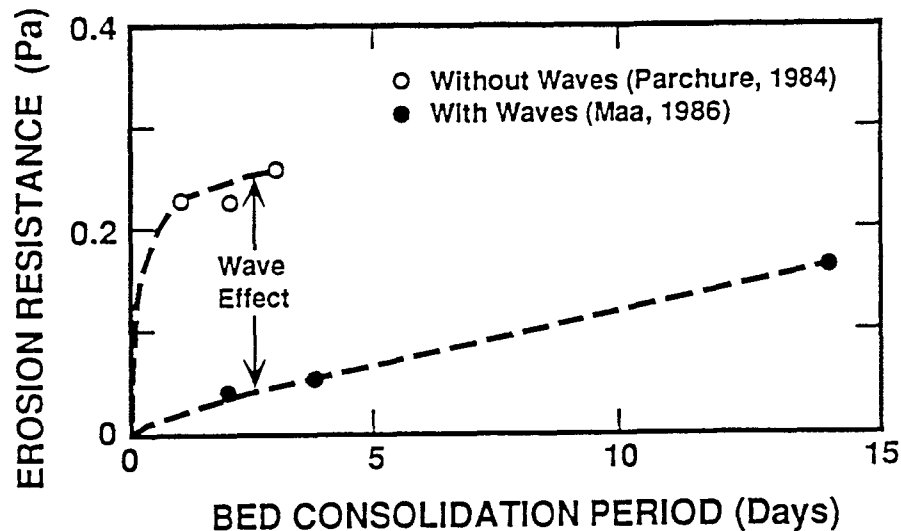


Figure 2.5: Influence of waves on shear resistance to erosion of kaolinite beds in flumes

effect of waves on the resistance to erosion is highlighted for beds of kaolinite of different consolidation periods in laboratory flumes. Erosion shear strengths representative of the top, thin bed layer in the upper curve were obtained by Parchure (1984) in the absence of waves. Representative values of bed shear resistance under waves corresponding to the lower curve were obtained by Maa (1986). The mean wave height during the wave experiments was 3.7 cm and the period was 1.6 sec. This example suggests that the fluid mud generating potential of waves can be a critical factor in eroding the cohesive soil bed, particularly in shallow water bodies. On the other hand, tidal current tends to serve as the main agent for advecting fluidized mud.

In the following section, the tasks carried out to meet the objectives of the present study mentioned in Section 1.2 are enumerated.

2.4 Tasks

The main experiments were carried out in a wave flume in the Coastal Engineering Laboratory of the University of Florida. The tasks were as follows:

1. Three types of clays, an attapulgite (palygorskite), a bentonite and a kaolinite, which together covered a wide range of cohesive properties, were initially selected for characterizing their rheological properties including viscosity and the upper Bingham yield

stress, and their time-dependent changes, before conducting the flume tests on fluidization.

2. A constitutive power-law model for the viscosity of the selected muds, fitted by the experimental data, was developed and used in a previously developed two-layered hydrodynamic wave-mud interaction model (Jiang & Mehta, 1991) to calculate the wave energy dissipation rate and the effective sheared mud thickness (defined in Chapter 4), a model-calculated representative of the fluidized mud thickness.
3. A composite mud, prepared from a 50/50 (by weight) mixture of attapulgite and kaolinite, was used to prepare the cohesive soil bed for the mud fluidization experiments. This bed had a "medium" degree of the resistance to shear stress, and was much more dissipative, and more realistic, compared with the mud which Ross (1988) used previously.
4. Wave flume characterization tests were conducted before the mud was introduced to determine the optimal operational domain for the flume specified by the wave height, period, and the water depth within which the waves were well behaved.
5. Pairs of total and pore pressure gauges were deployed at different elevations below the mud surface in a vertical array, and one additional total pressure gauge was mounted at the bottom of the flume for accurately determining the total load at the bottom. With these gauges the soil mechanical change during wave action was monitored.
6. Two capacitance gauges within the test section of the flume were used to monitor the wave amplitudes. Bulk density profiles of the deposit during wave action were measured vertically with a Paar (model 2000) density meter.
7. The hydrodynamic wave-mud interaction model was used to calculate the effective sheared mud thickness, and the wave energy dissipation rate.

8. The effective sheared mud thickness from the hydrodynamic model was compared with the fluidized mud thickness obtained from the flume pressure measurements. Also, the relationship between the rate of wave energy dissipation and the rate of fluidization was investigated.

CHAPTER 3 PRELIMINARY EXPERIMENTS

3.1 Sediment and Fluid Characterization

Three types of commercially available clays: a kaolinite, a bentonite, and an attapulgite, which together cover a wide range of cohesive properties, were initially selected. Kaolinite (pulverized kaolin), a light beige-colored powder, was purchased from the EPK Division of Feldspar Corporation in Edgar, Florida. The Cation Exchange Capacity (CEC) of the kaolinite given by the supplier is 5.2-6.5 milliequivalents per 100 grams. Bentonite was obtained from the American Colloid Company in Arlington Heights, Illinois. It is a sodium montmorillonite, its commercial name is Volclay and is light gray in color. Its CEC is about 105 milliequivalents per 100 grams. Attapulgite, of greenish-white color, was purchased from Floridin in Quincy, Florida. It is also called palygorskite, and its CEC is 28 milliequivalents per 100 grams as given by the supplier. Tables 3.1 through 3.3 give the chemical compositions of the three clays (given by the suppliers).

Table 3.4 gives the results of chemical analysis of the tap water used to prepare mud, whose pH value was 8 and conductivity 0.284 milimhos. This analysis was conducted in the Material Science Department of the University of Florida. The procedure was as follows: firstly, an element survey of both the tap water and double-distilled water was performed, which determined the ions in tap water. Secondly, standard solutions of these ions contained in the tap water were made, and the tap water was analyzed against the standard solutions to determine the concentrations of the ions by an emission spectrometer (Plasma II).

Table 3.1: Chemical composition of kaolinite

SiO ₂	46.5%	MgO	0.16%
Al ₂ O ₃	37.62%	Na ₂ O	0.02%
Fe ₂ O ₃	0.51%	K ₂ O	0.40%
TiO ₂	0.36%	SO ₃	0.21%
P ₂ O ₅	0.19%	V ₂ O ₅ <	0.001%
CaO	0.25%		

Table 3.2: Chemical composition of bentonite

SiO ₂	63.02%	Al ₂ O ₃	21.08%
Fe ₂ O ₃	3.25%	FeO	0.35%
MgO	2.67%	Na ₂ O & K ₂ O	2.57%
CaO	0.65%	H ₂ O	5.64%
Trace Elements	0.72%		

Table 3.3: Chemical composition of attapulgite (palygorskite)

SiO ₂	55.2%	Al ₂ O ₃	9.67%
Na ₂ O	0.10%	K ₂ O	0.10%
Fe ₂ O ₃	2.32%	FeO	0.19%
MgO	8.92%	CaO	1.65%
H ₂ O	10.03%	NH ₂ O ⁻	9.48%

Table 3.4: Chemical composition of tap water

Si	11.4 ppm
Al	1.2 ppm
Fe	0.2 ppm
Ca	24.4 ppm
Mg	16.2 ppm
Na	9.6 ppm
Total Salts	278 ppm

The particle size distributions of kaolinite, attapulgite, and bentonite are given shown in Tables 3.5, 3.6 and 3.7. The procedure for determination was: firstly, a particular suspension was prepared at about 0.5% by weight concentration, and run for at least 15 minutes in a sonic dismembrater (Fisher, model 300) to breakdown any agglomerates. Secondly, the suspension was analyzed in a particle size distribution analyser Horiba (model CAPA 700), and allowed to gradually settle down to the bottom. Particle concentration and fall velocities were determined with an X-ray, which could be converted to Stokes equivalent diameters. The median particle sizes of kaolinite, attapulgite, and bentonite were $1.10\mu m$, $0.86\mu m$, and $1.01\mu m$, respectively. Scanning Electron Microscope (SEM) photographs of the three types of clays, as dry agglomerates, are shown in Figures 3.1, 3.2 and 3.3.

Table 3.5: Size distribution of kaolinite

D(μm)	Percent size distribution(%)	Cumulative size distribution(%)
5.00<	0.0	0.0
5.00-3.20	0.0	0.0
3.20-3.00	2.9	2.9
3.00-2.80	4.0	6.9
2.80-2.60	2.6	9.5
2.60-2.40	4.1	13.6
2.40-2.20	4.0	17.6
2.20-2.00	6.0	23.6
2.00-1.80	5.7	29.3
1.80-1.60	6.2	35.5
1.60-1.40	5.5	41.0
1.40-1.20	6.2	47.2
1.20-1.00	5.8	53.0
1.00-0.80	5.0	58.0
0.80-1.60	10.4	68.4
0.60-0.40	11.2	79.6
0.40-0.20	13.6	93.2
0.20-0.00	6.8	100.0

Table 3.6: Size distribution of bentonite

D(μm)	Percent size distribution(%)	Cumulative size distribution(%)
3.00<	5.9	5.9
3.00-2.80	1.9	7.8
2.80-2.60	2.3	10.1
2.60-2.40	2.5	12.6
2.40-2.20	3.0	15.6
2.20-2.00	3.0	18.6
2.00-1.80	4.9	23.5
1.80-1.60	5.3	28.8
1.60-1.40	8.1	36.9
1.40-1.20	4.5	41.4
1.20-1.00	9.3	50.7
1.00-0.80	9.1	59.8
0.80-1.60	11.4	71.2
0.60-0.40	11.2	82.4
0.40-0.20	11.5	93.3
0.20-0.00	6.1	100.0

Table 3.7: Size distribution of attapulgite

D(μm)	Percent size distribution(%)	Cumulative size distribution(%)
2.00<	11.8	11.8
2.00-1.80	4.1	15.9
1.80-1.60	4.9	20.8
1.60-1.40	5.3	26.1
1.40-1.20	5.6	31.7
1.20-1.00	5.8	37.5
1.00-0.80	17.4	54.9
0.80-1.60	25.5	80.4
0.60-0.40	12.3	92.7
0.40-0.20	6.1	98.8
0.20-0.00	1.2	100.0



Figure 3.1: SEM of dry agglomerates of attapulgite. Scale $1\text{cm} = 10\mu\text{m}$



Figure 3.2: SEM of dry agglomerates of bentonite. Scale $1\text{cm} = 10\mu\text{m}$

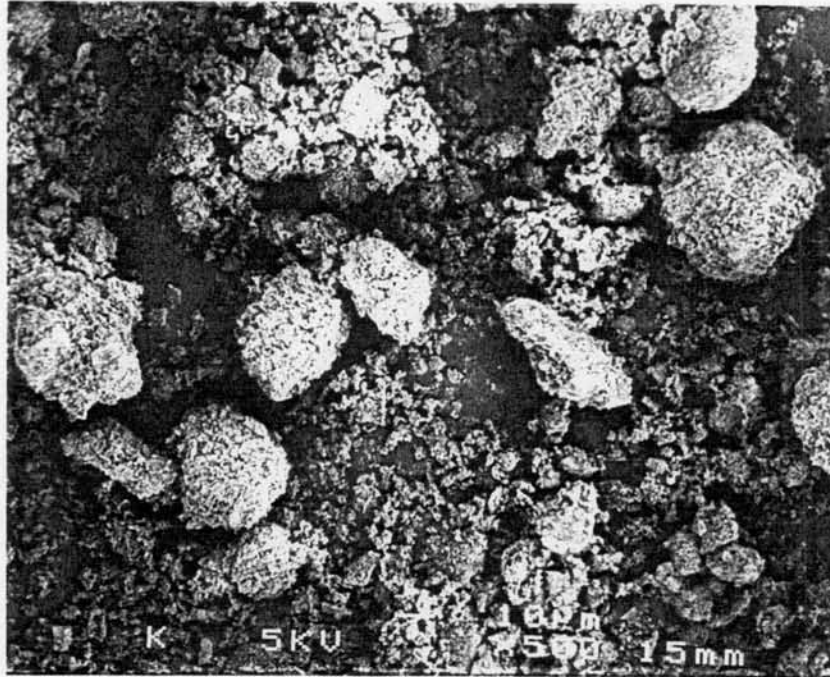


Figure 3.3: SEM of dry agglomerates of kaolinite. Scale $0.5\text{cm} = 10\mu\text{m}$

3.2 Rheological Experiments

The rheological properties of mud, including viscosity and the upper Bingham yield stress, and their time-dependent changes, are very important in ultimately controlling soft muddy bottom erosion, wave energy dissipation, and mud transportation along coasts and in estuaries. In the present study, the viscosity and the upper Bingham yield stress of several types of muds (clay-water mixtures) were measured to determine which ones could be selected for the wave-induced fluidization experiments. Also through these measurements a mud viscosity model was developed, which was then used in the two-layered hydrodynamic wave-mud interaction model as described in Chapter 4.

Each mud sample was prepared by adding tap water to the clay, or a mixture of two clays, and mixing the material for 5 to 20 minutes and adjusting the amount of water to the desired density which was selected to approximate those of typical soft natural muds. Composite muds were made by adding any two of equally weighted clays together. One-half

percent salt, which is about the critical salinity value for coagulating clays in sea water, was added in each of six samples, while no salt was added in six other samples of the same compositions. Thus as shown in Table 3.8 a total of twelve mud samples were prepared in this way.

Table 3.8: Selected muds (clays and clay mixtures) for rheological tests

Symbol	Components	Density (g/l)
K	kaolinite	1.30
KS	kaolinite + 0.5 % salt	1.30
B	bentonite	1.05
BS	bentonite + 0.5 % salt	1.03
A	attapulgate	1.10
AS	attapulgate + 0.5 % salt	1.08
BK	kaolinite + bentonite	1.16
BKS	kaolinite + bentonite + 0.5 % salt	1.16
AB	attapulgate + bentonite	1.05
ABS	attapulgate + bentonite + 0.5 % salt	1.05
AK	attapulgate + kaolinite	1.19
AKS	attapulgate + kaolinite + 0.5 % salt	1.19

The samples were set aside for about two weeks to attain equilibration between the solid and the liquid phases in terms of ion exchange. The equipment used was the Brookfield viscometer (model LVT), in which a rotating bob is immersed in a beaker of mud. The bob can rotate at selected fixed speeds, giving a shear rate range of 0.125 to 12.5 Hz. The torque generated can be read from a meter, to which the shear stress is directly proportional. In each test the shear rate was increased in steps, with a fixed time interval, e.g., 10 mins (or 10 cycles of the bob rotation) between the change of shear rate, and then decreased gradually back to the starting point. For the pure muds, i.e., A, B, K, cycles of bob rotation were used, and for the composite ones and muds with salt, i.e., KS, BS, AS, BK, BKS, AB, ABS, AK, AKS, the time of application of a shear rate in mins was used. For each type of mud the test was repeated several times with different time intervals including 5 mins, 10 mins, and 20 mins (or 5 cycles, 10 cycles, and 20 cycles) to examine the time-dependent behavior of the materials.

The viscosity of muds can be significantly affected by such variables as the shear rate, temperature, pressure and the time of shearing. Here the shear rate and the shearing duration (time or cycles) are considered to be the most relevant influences on viscosity. Figures 3.4 and 3.5 show the experimental flow curves, plotted as shear stress versus shear rate. For comparison between different materials, the curves corresponding to muds subjected to the same shearing time of 10 mins (or 10 cycles) are shown in Figures 3.6 and 3.7, showing the relationship between shear stress and shear rate, where the arrows indicate the direction of the rising and falling flow curves. The corresponding curves of viscosity (obtained by dividing shear stress by shear rate using the rising curves) versus shear rate are plotted in Figures 3.8 and 3.9.

3.2.1 Influence of Shear Rate

The experimental data points, which are represented by point markers in Figures 3.8 and 3.9, indicate that all the materials, except attapulгите, generally exhibit a shear-thinning behavior, i.e., the viscosity decreases as the shear rate increases. While attapulгите at low shear rates shows a shear-thinning behavior, at higher shear rates it exhibits shear-thickening behavior and then reverts to shear-thinning as the shear rate is increased to even higher values. In the case of Figure 3.8(e),(f), for example, it can be seen that the viscosity of attapulгите decreases up to a shear rate of 2 Hz, then increases as the shear rate increases from 2 Hz to 6 Hz, and finally decreases again as the shear rate continues to increase beyond 6 Hz, when the sample is subjected to a shearing duration of 20 mins (or 20 cycles) at each step.

General power-law equations that predict the shape of the curves representing the variation of viscosity with shear rate typically need at least four parameters. One such relation is the Cross (1965) equation given by

$$\frac{\mu_0 - \mu}{\mu - \mu_\infty} = (c_1 \dot{\gamma})^p \quad (3.1)$$

where μ_0 and μ_∞ refer to the asymptotic values of the viscosity at very low and very high shear rates, respectively, c_1 is a constant parameter having dimensions of time, p is a

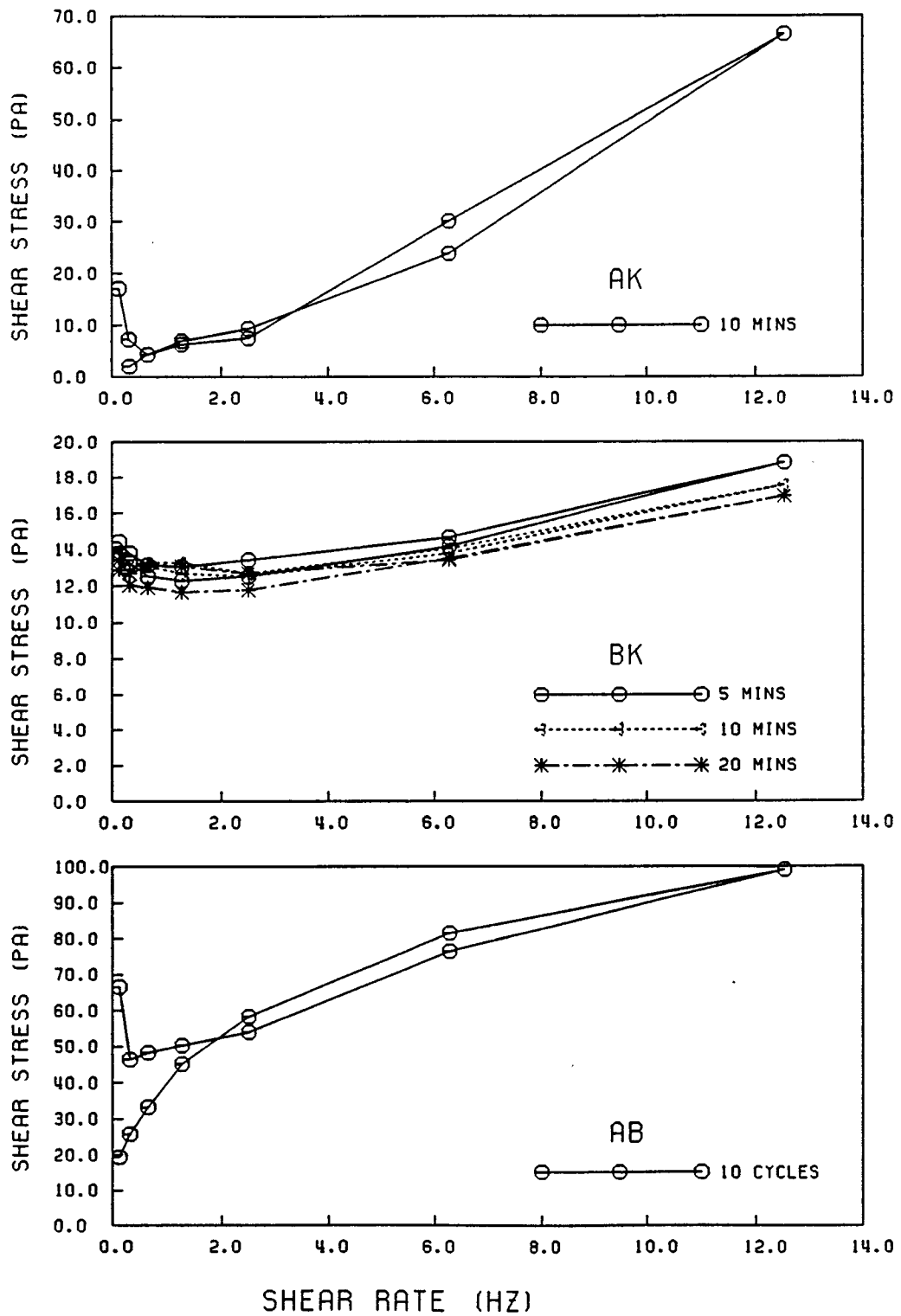


Figure 3.4: Shear stress, σ , versus shear rate, $\dot{\gamma}$, (K,A,B)

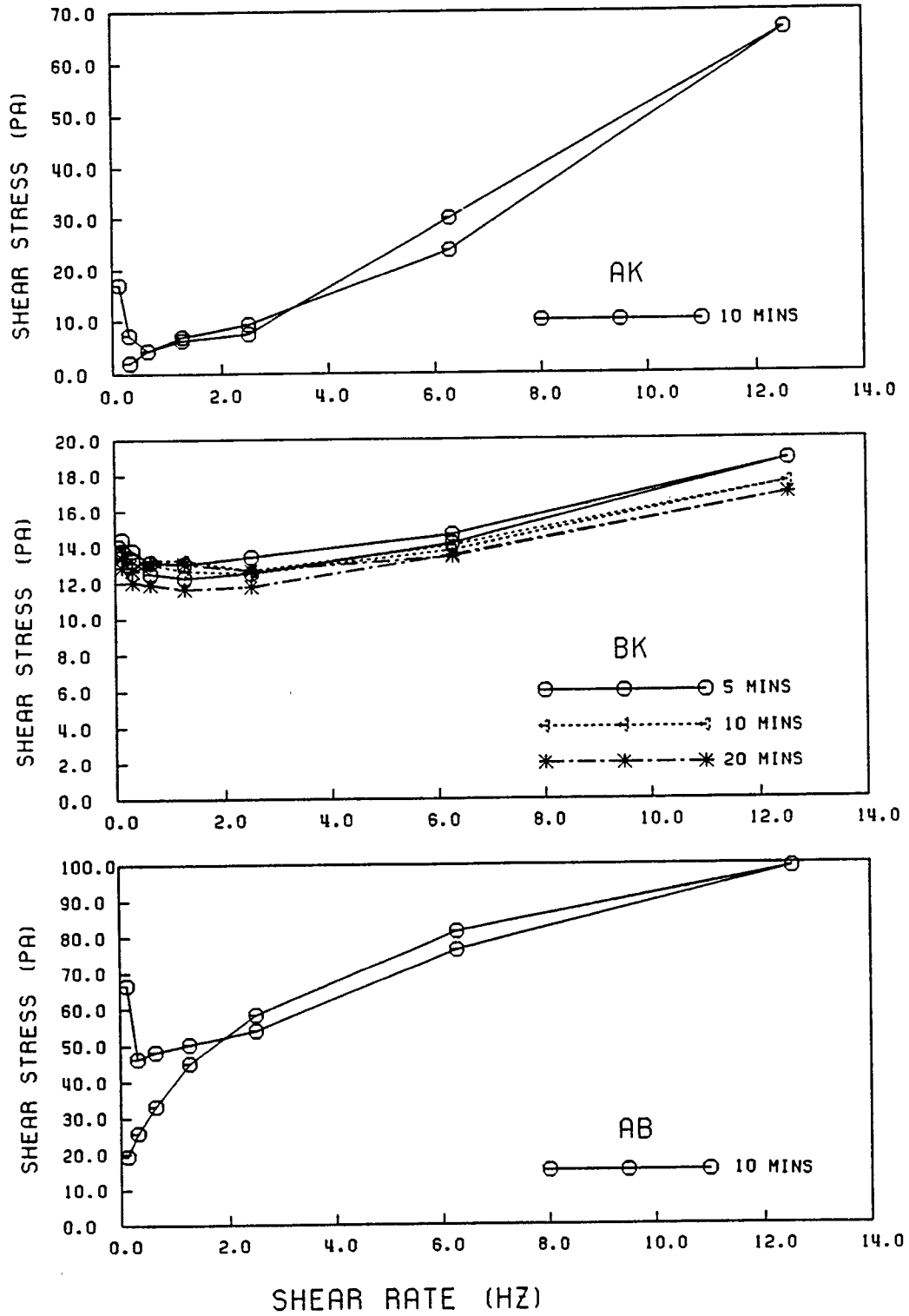


Figure 3.5: Shear stress, σ , versus shear rate, $\dot{\gamma}$, (AK,BK,AB)

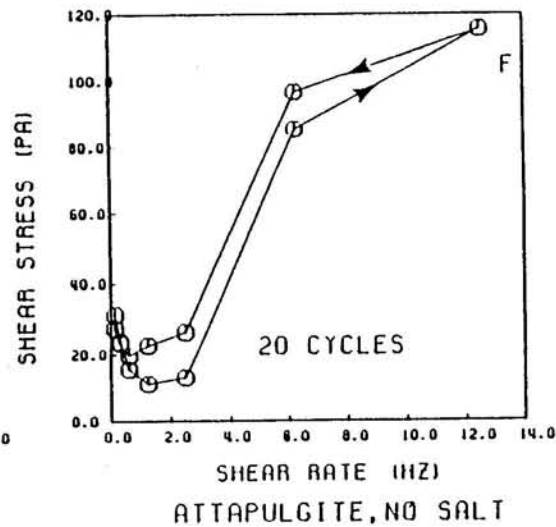
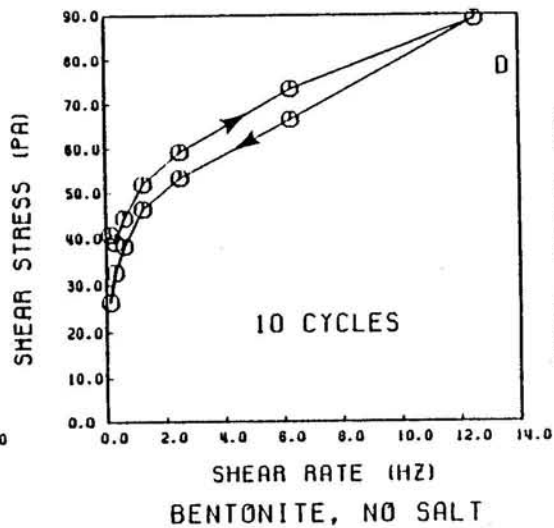
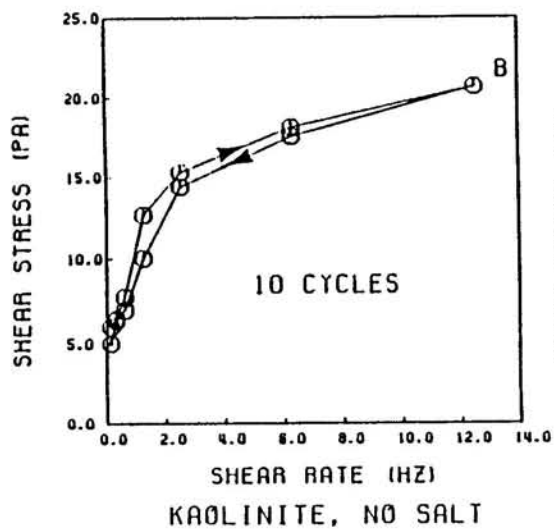
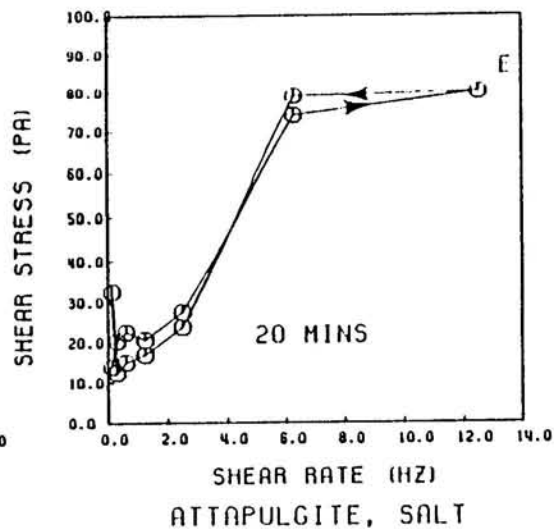
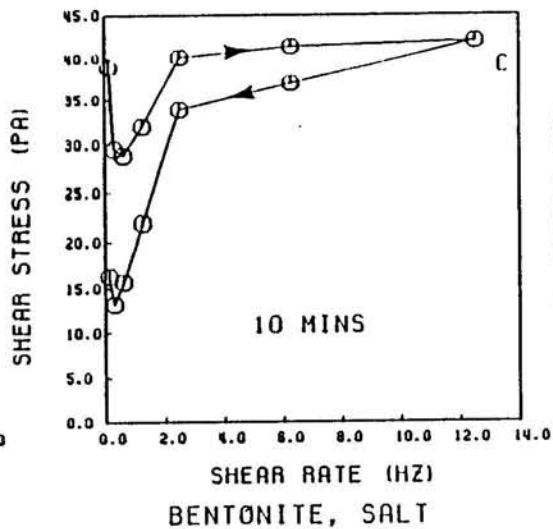
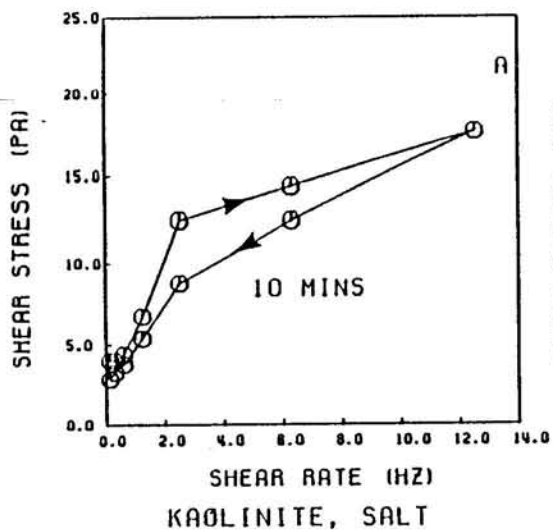


Figure 3.6: Shear stress, σ , versus shear rate, $\dot{\gamma}$, (K,KS,A,AS,B,BS)

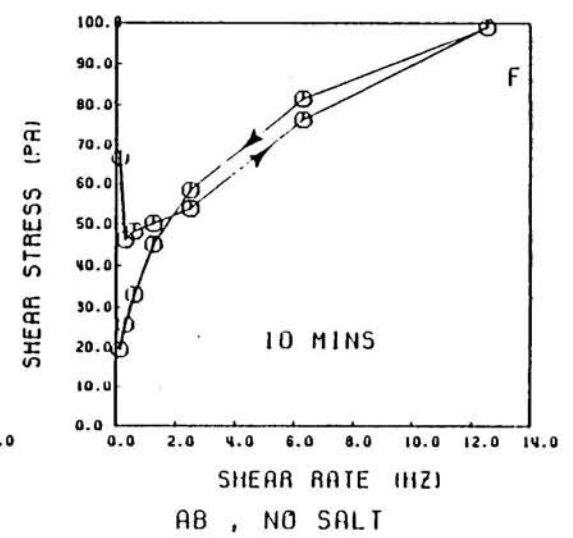
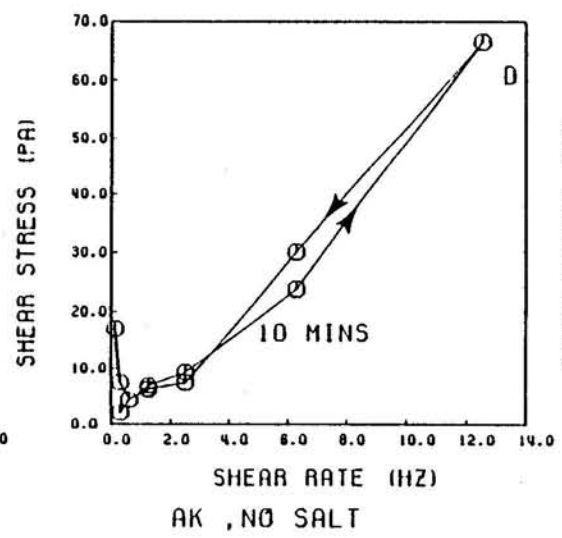
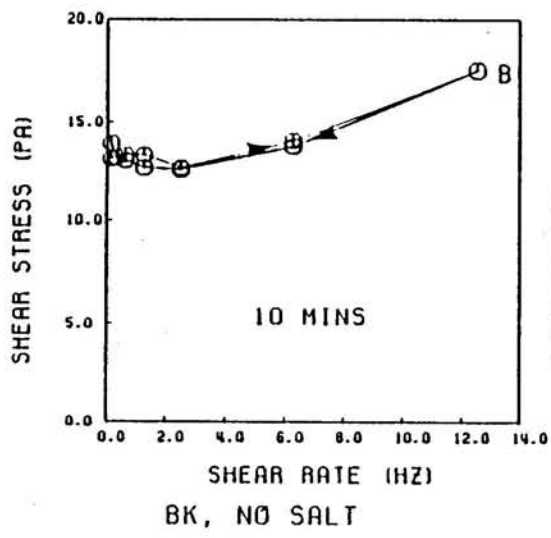
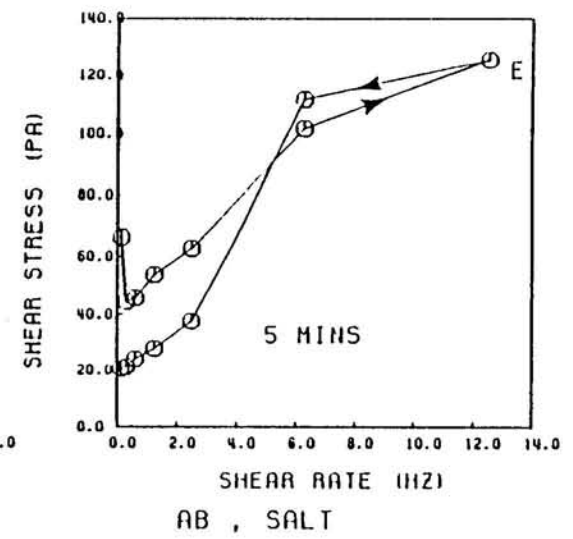
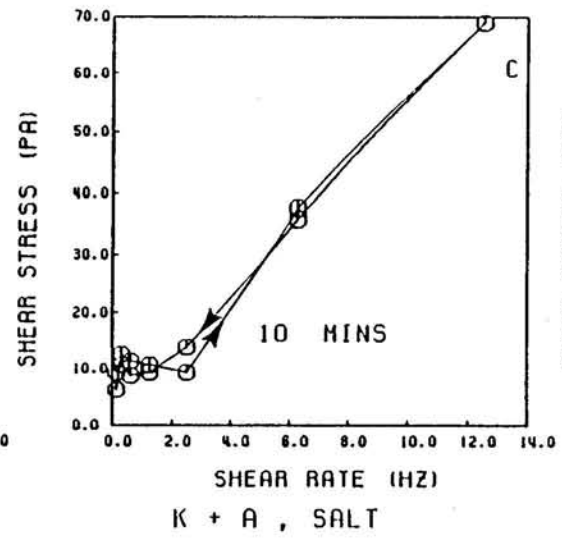
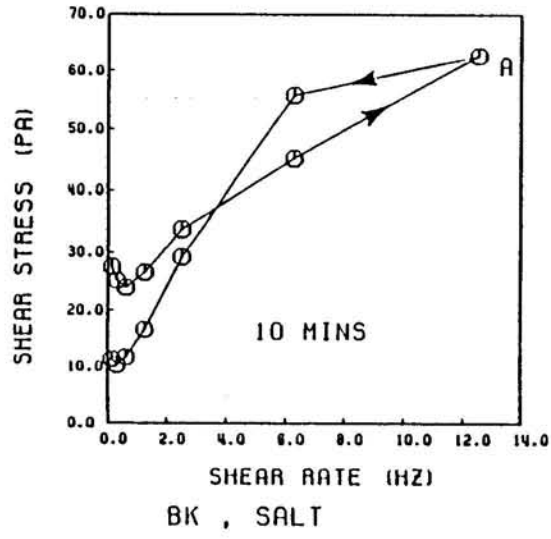


Figure 3.7: Shear stress, σ , versus shear rate, $\dot{\gamma}$, (BK,BKS,AK,AKS,AB,ABS)

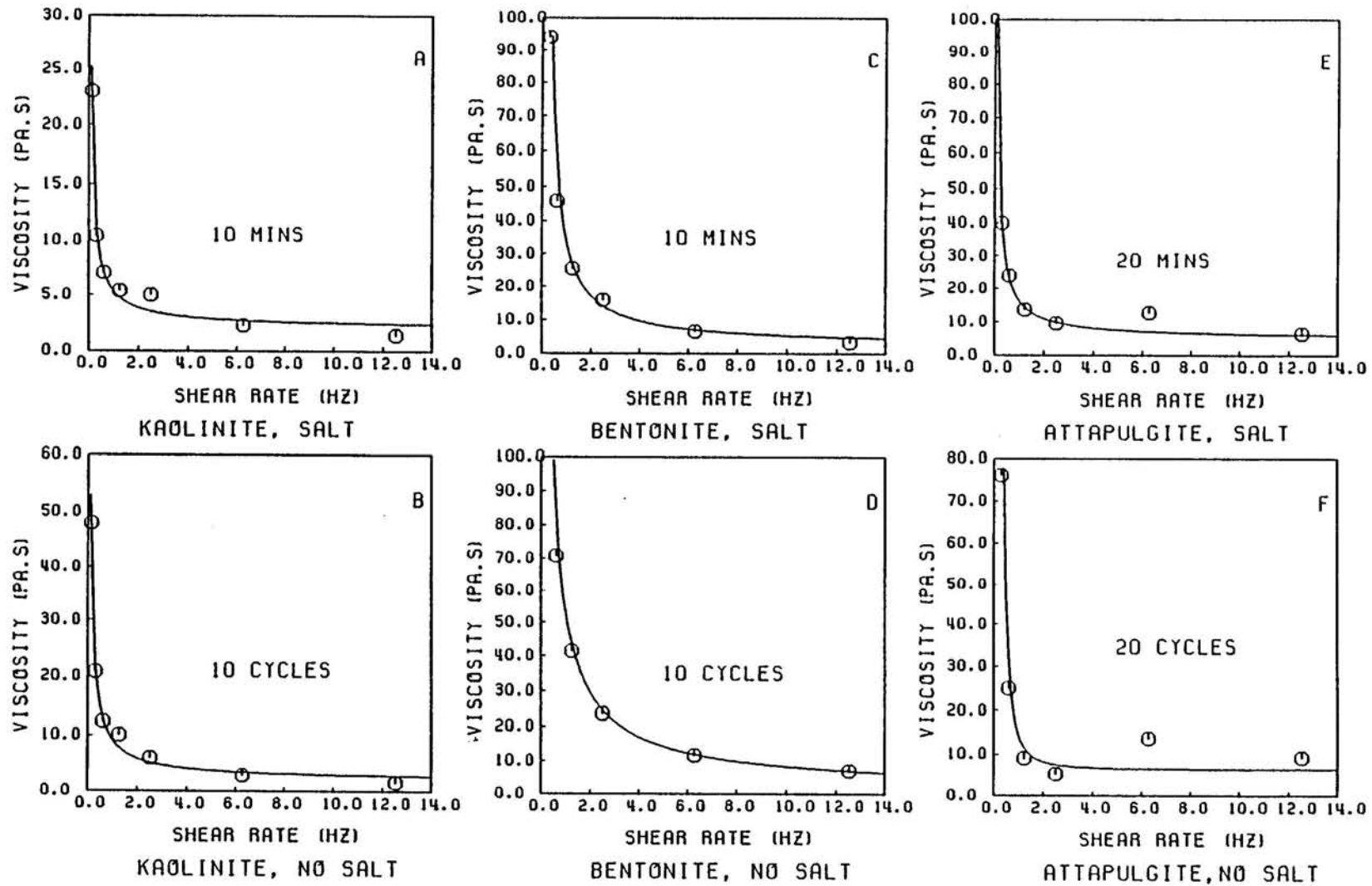


Figure 3.8: Viscosity, μ , versus shear rate, $\dot{\gamma}$, (K,KS,A,AS,B,BS)

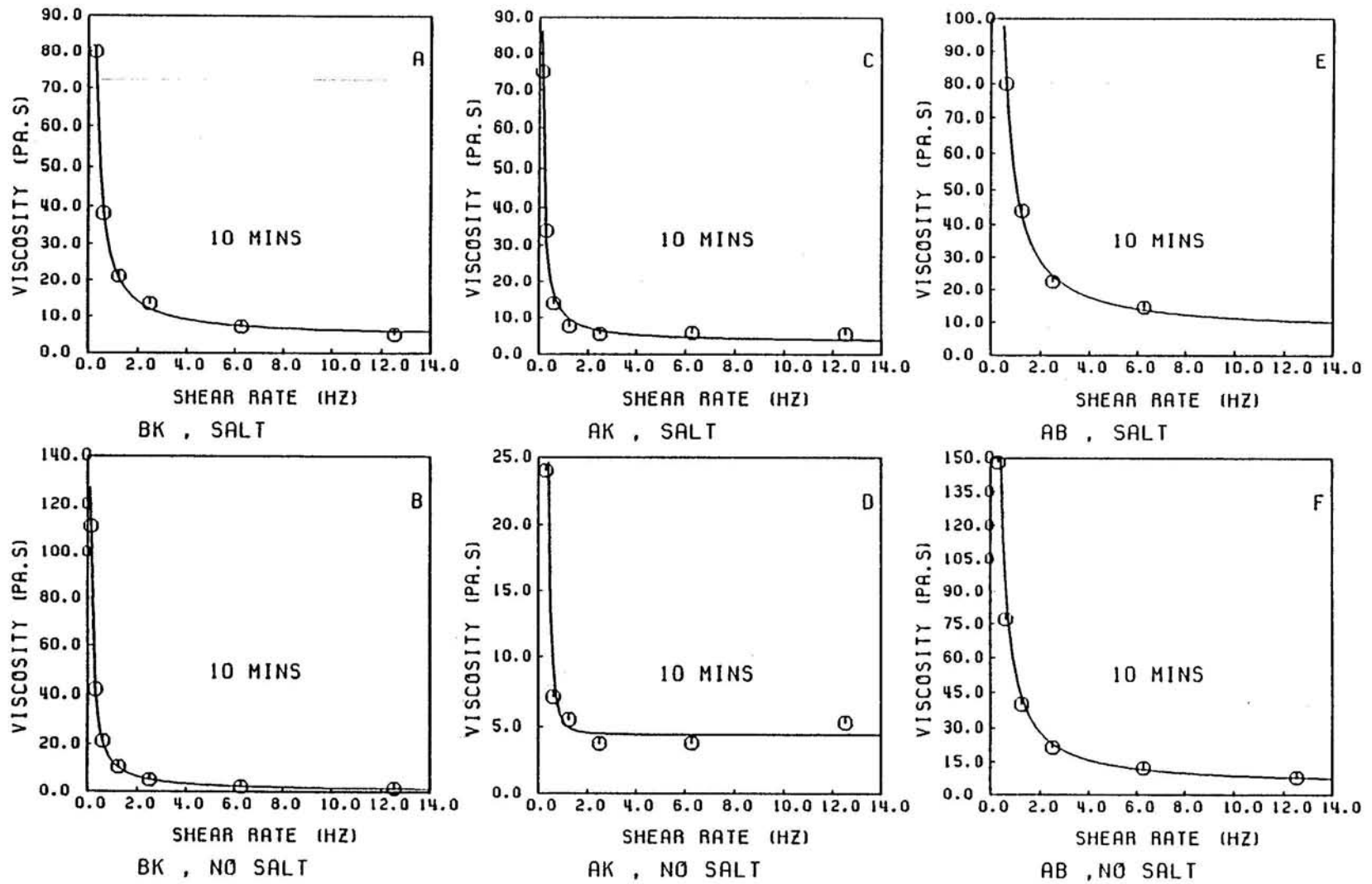


Figure 3.9: Viscosity, μ , versus shear rate, $\dot{\gamma}$, (BK,BKS,AK,AKS,AB,ABS)

dimensionless constant, μ is the apparent viscosity and $\dot{\gamma}$ is the shear rate.

In all the studied cases, $\mu \ll \mu_0$, hence the above equation can be simplified as

$$\frac{\mu_0}{\mu - \mu_\infty} = (c_1 \dot{\gamma})^p \quad (3.2)$$

which can be further written as

$$\mu = \mu_\infty + \frac{\mu_0}{(c_1 \dot{\gamma})^p} \quad (3.3)$$

or

$$\mu = \mu_\infty + c \dot{\gamma}^{n-1} \quad (3.4)$$

Equation 3.4 is referred to as the Sisko (1958) model, where μ_∞ is the constant viscosity at the limit of high (theoretically infinite) shear rate, c is a measure of the consistency of material, and n is a parameter that indicates whether the material is shear-thinning or shear-thickening, that is, when $n > 1$ the material exhibits shear-thickening, otherwise it possesses a shear-thinning behavior.

To solve for the three parameters, μ_∞ , c and n , the least squares method was used for fitting the curves obtained from Equation 3.4 to the experimental data. For this method it is required that the viscosity difference between the model (Equation 3.4) and data, D , be minimized, that is,

$$D = \sum_{i=1}^N (\hat{\mu}_i - \mu)^2 = \text{minimum} \quad (3.5)$$

or

$$D = \sum_{i=1}^N (\hat{\mu}_i - \mu_\infty - c \dot{\gamma}^{n-1})^2 = \text{minimum} \quad (3.6)$$

where $\hat{\mu}_i$ is viscosity of the mud obtained from the experiment, and N is the number of data points.

Setting

$$\frac{\partial D}{\partial \mu_\infty} = 0 \quad (3.7)$$

$$\frac{\partial D}{\partial c} = 0 \quad (3.8)$$

$$\frac{\partial D}{\partial n} = 0 \quad (3.9)$$

Equations 3.5 and 3.6 can be expressed as

$$\sum_{i=1}^N (\hat{\mu}_i - \mu_{\infty} - c\dot{\gamma}^{n-1}) = 0 \quad (3.10)$$

therefore

$$\sum_{i=1}^N \{\dot{\gamma}^{n-1}(\hat{\mu}_i - \mu_{\infty} - c\dot{\gamma}^{n-1})\} = 0 \quad (3.11)$$

hence

$$\sum_{i=1}^N \{c\dot{\gamma}^{n-1} \log \dot{\gamma}(\hat{\mu}_i - \mu_{\infty} - c\dot{\gamma}^{n-1})\} = 0 \quad (3.12)$$

In this way, μ_{∞} , c and n can be determined from the three equations above. The results are given in Table 3.9. In all cases, $n < 1$, and that the data point of attapulgite near the shear rate of 6 Hz was conveniently removed when fitting the model. Therefore, all the materials (except of course attapulgite over a certain shear rate range) are observed to exhibit shear-thinning behavior. The greater the departure of n from unity, the more pronounced the shear-thinning behavior of the material. The higher the value of c , the more viscous the mud (Wilkinson, 1960). The upper limit of viscosity, μ_{∞} , represents resistance to flow in the limit of a very high shear rate. It can be seen that attapulgite has the highest value of μ_{∞} among the three types of clays, up to 5 to 6 Pa.s. Kaolinite and bentonite have lower μ_{∞} values, about 2 Pa.s. For the composite materials, AB has a high μ_{∞} of 4.3 Pa.s, ABS has as high as 7 Pa.s because of the coagulating effect of adding salt. While BK has a low value of μ_{∞} , about 0.6 Pa.s, salt also increases μ_{∞} (of BKS) to a comparatively high value of 4.7 Pa.s.

Generally, salinity does increase the coagulating tendency of clays (Parchure, 1984), which in turn increases the viscosity. However, salt does not greatly affect the viscosity of kaolinite due to its somewhat anomalous properties. For example, kaolinite flocculates more readily in distilled water than in salt water, although the nature of flocculation is different in the two cases (Parchure, 1984).

Table 3.9: Parameters for the Sisko power-law model for viscosity

Mud	μ_{∞} (Pa.s)	c	n
K	2.10	7.08	0.106
KS	2.06	3.31	0.117
B	0.41	48.68	0.207
BS	2.46	28.26	-0.009
A	6.34	6.86	-1.0
AS	5.00	11.54	0.038
BK	0.61	12.29	-0.057
BKS	4.69	20.60	-0.114
AB	4.28	45.2	0.002
ABS	7.06	45.07	-0.039
AK	4.44	0.76	-1.083
AKS	3.35	8.02	0.059

3.2.2 Influence of Shearing Time

For a given shear rate, the corresponding shear stress, and hence the viscosity, can either increase or decrease with time of shearing. This type of behavior is either called, respectively, "thixotropy," which usually occurs in circumstances where the material is shear-thinning, or "anti-thixotropy," which is usually associated with shear-thickening behavior. As an illustration of the generally thixotropic influence of shearing time on shear stress, Figures 3.4, 3.5, and Table 3.10 give the shear stresses at different times at the selected shear rate of 6 Hz. It can be seen that shearing time had the greatest effect on the viscosity of attapulgite and the smallest on kaolinite. Bentonite was in-between. For the muds containing kaolinite, i.e., KS, BK, BKS, the effect of shearing time was also very small, while for AS and BS this effect was relatively greater.

Time-dependent mud behavior leads to a hysteresis loop in the flow curves of shear stress versus shear rate when the curves are plotted first for increasing and then decreasing shear rate sequences. This behavior is observed in Figures 3.4, 3.5, 3.6, and 3.7, in which it can be seen that all the materials more or less exhibit a hysteresis loop. When the material is sheared, typically the structure progressively breaks down and the apparent viscosity

Table 3.10: Shearing time effect on shear stress

Symbol	5 cycles	10 cycles	15 cycles	20 cycles	25 cycles	30 cycles
K	19.4	17.9	17.7	18.8		
B	74.3	69.9	61.8		66.8	
A		25.0		90.9		25.7
	5 mins	10 mins	15 mins	20 mins		
KS	14.7	13.5	13.0			
BS	46.7	39.2				
AS	62.7			76.5		
BK	14.4	13.9		13.5		
BKS	53.3	50.5		56.7		
AB		76.5				
ABS		101.6				
AK		23.8				
AKS		35.9				

decreases with time. The rate of breakdown of the structure during shearing at a given rate depends on the number of linkages available for breaking and must therefore decrease with time (Wilkinson, 1960). Also, during shearing asymmetric particles or molecules are better aligned, i.e., instead of a random, intermingled state which exists when the material is at rest, the major particle axes are brought in line with the direction of flow. The apparent viscosity thus continues to decrease with increasing rate of shear until no further alignment along the streamline is possible.

3.2.3 Upper Bingham Yield Stress

The upper Bingham yield stress, σ_B , the stress that must be exceeded before flow starts, can be determined from the plots of shear stress versus shear rate in Figures 3.6 and 3.7 by drawing a line tangent to the upper range of shear rates (Wilkinson, 1960). The intersection of this tangent with the stress axis gives σ_B . The results are presented in the Table 3.11. This table shows that among the three types of clays, attapulgite has the highest upper Bingham yield stress with 72 Pa, kaolinite has the lowest one with 10 Pa, and bentonite is in-between with 50 Pa. The composite materials that contain kaolinite, i.e., AK, AKS, BK, have very low upper Bingham yield stresses that are less than 10 Pa, except BKS, which

Table 3.11: Upper Bingham yield stress

sample	K	KS	B	BS	A	AS	BK	BKS	AB	ABS	AK	AKS
σ_B (Pa)	15.0	9.5	50.0	36.0	66.0	72.0	10.0	39.0	58.0	88.0	0.0	4.0

has a relatively higher σ_B of 39 Pa. The higher value of the upper Bingham yield stress for BKS is likely to be due to the presence of salt, which in general promotes flocculation of clays. Of the composite materials AB and ABS have the highest upper Bingham yield stresses with values of 58 Pa and 88 Pa, respectively. ABS also has a higher value of σ_B than AB presumably because of the effect of salt. Salt might increase the upper Bingham yield stress of bentonite as well, although the upper yield stress of BS, 36 Pa, is less than that of B, which is 50 Pa. Note that when BS was tested the density had to be reduced from 1.05 g l^{-1} to 1.03 g l^{-1} in order to keep the torque reading within the viscometer gauge range.

3.2.4 Gelling

Gelling is a special case of flocculation. It can result instead of flocculation when electrolytes are added to certain moderately concentrated soils. A gel is a homogeneous-looking system displaying some rigidity and elasticity. When gelling occurs, its effect is manifested in the flow curve of shear stress versus shear rate. Thus at the beginning, starting with a very low shear rate, the stress decreases when the shear rate increases due to the breakdown of the gel. Thereafter, the stress goes up as the shear rate continues to increase. Attapulgitte and bentonite exhibit measurable gelling behavior, especially when salt is added. Gelling also occurred in AB, ABS, BKS. See examples in Figure 3.6 (c), (e) and (f), as well as in Figure 3.7 (d), (e) and (f).

3.2.5 Summary

Table 3.12 gives a summary of the properties of the materials that have been studied, where τ_B of ABS refers to the value corresponding to 5 mins shearing duration. The

following observations are noteworthy:

1. All the selected materials exhibited shear-thinning, although attapulgite behaved as a shear-thickening material somewhere in the shear rate range from 2.5 to 6.0 Hz.
2. For both the viscosity and the upper Bingham yield stress, kaolinite had the lowest values among the three types of clays, attapulgite the highest, and bentonite was in-between. The composite materials that contained kaolinite had relatively low viscosities and low upper Bingham yield stresses, while the attapulgite and bentonite composite had higher values.
3. Salt had a measurable effect in increasing the viscosity of bentonite as well as the composites that contained bentonite. Salt increased the upper limit viscosity, μ_{∞} , of B by 500%, BK by 660%, and AB by 65%. It increased the upper Bingham yield stress of BK by 290% and AB by 50%. Salt did not significantly change the viscosity of kaolinite and attapulgite. It decreased both μ_{∞} and σ_B of kaolinite by less than 10%. Finally, salt decreased μ_{∞} and increased σ_B of attapulgite by less than 10%.
4. Of the three types of clays, time or duration of shearing had the greatest effect on attapulgite, the smallest on kaolinite, and bentonite was in-between. Thus attapulgite had the highest thixotropy.
5. Attapulgite and bentonite were influenced by gelling, especially when salt was added. The gelling effect also appeared in AB, ABS, BKS. Kaolinite did not exhibit this effect.

3.3 Instrumentation

3.3.1 Wave Gauges

Two capacitance-type gauges were installed in the flume to monitor the required surface wave information. Calibration of the two gauges was conducted in situ by increasing the

Table 3.12: Rheological parameters for power-law given by Equation 3.4

Mud	time	Density (g/l)	σ_B (Pa)	μ_∞ (Pa.s)	c	n
K	10 cycles	1.30	15.0	2.1	7.08	0.106
K+0.5% S	10 mins	1.30	9.5	2.06	3.31	0.117
B	10 cycles	1.05	50.0	0.41	48.68	0.207
B+0.5% S	10 mins	1.03	36.0	2.46	28.26	-0.009
A	20 cycles	1.10	66.0	6.34	6.86	-1.0
A+0.5% S	20 mins	1.10	72.0	5.00	11.54	0.038
B+K	10 mins	1.16	10.0	0.61	12.29	-0.057
B+K+0.5% S	10 mins	1.16	39.0	4.69	20.6	-0.114
A+B	10 mins	1.05	58.0	4.28	45.2	0.002
A+B+0.5% S	10 mins	1.05	88.0	7.06	45.07	-0.039
A+K	10 mins	1.19	0.0	4.44	0.76	-1.083
A+K+0.5% S	10 mins	1.19	4.0	3.35	8.02	0.059

water level in steps of 1 to 2 cm, while the gauges were held in fixed positions. The linear least squares method was used to obtain a regression equation. Results of calibration are shown in Figure 3.10. Water level variation was recorded by a data acquisition system briefly described later in this chapter. The sampling frequency was 40 Hz for 0.5-sec wave and 20 Hz for 1 to 2-sec waves.

3.3.2 Current Meter

An electromagnetic Marsh-McBirney current meter (model 523) was used to measure the horizontal velocities in the water column. Calibration of the current meter is shown in Figure 3.11, which was conducted in a V-notched weir flume in the Civil Engineering Department. The current meter had two restrictions. Firstly, the probe could not be placed close to the water-air or water-bed interface due to the drastic change in material (medium) density and conductivity associated with the electromagnetic field, which resulted in an unrealistic output. Secondly, the meter generated strong interference with other instruments which meant that only the current meter could be used at a given time. Thus other data had to be collected during separate time windows. The sampling frequency for the current meter data was the same as the wave gauges.

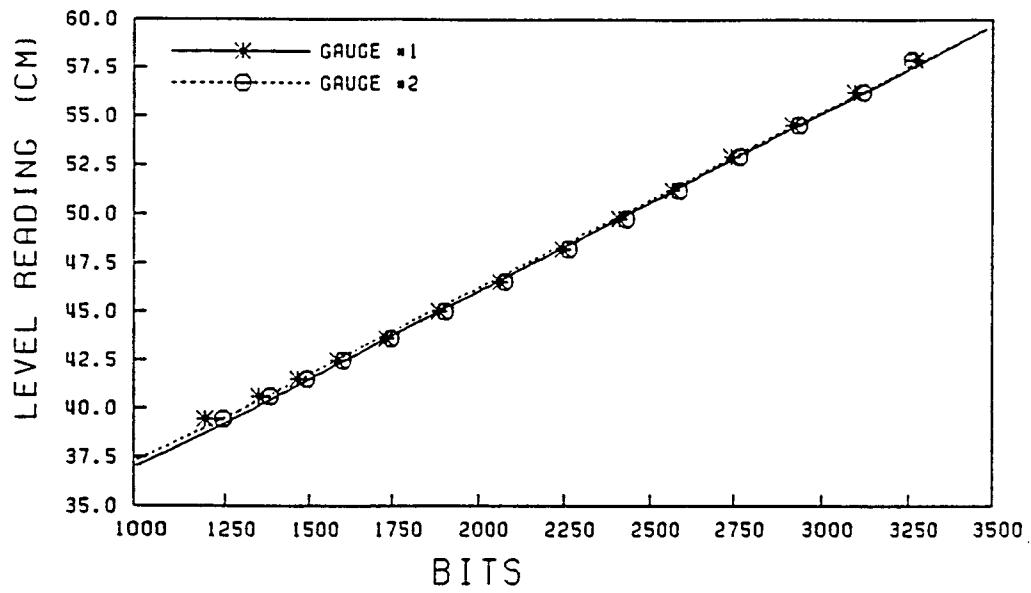


Figure 3.10: Calibration curves for the wave gauges

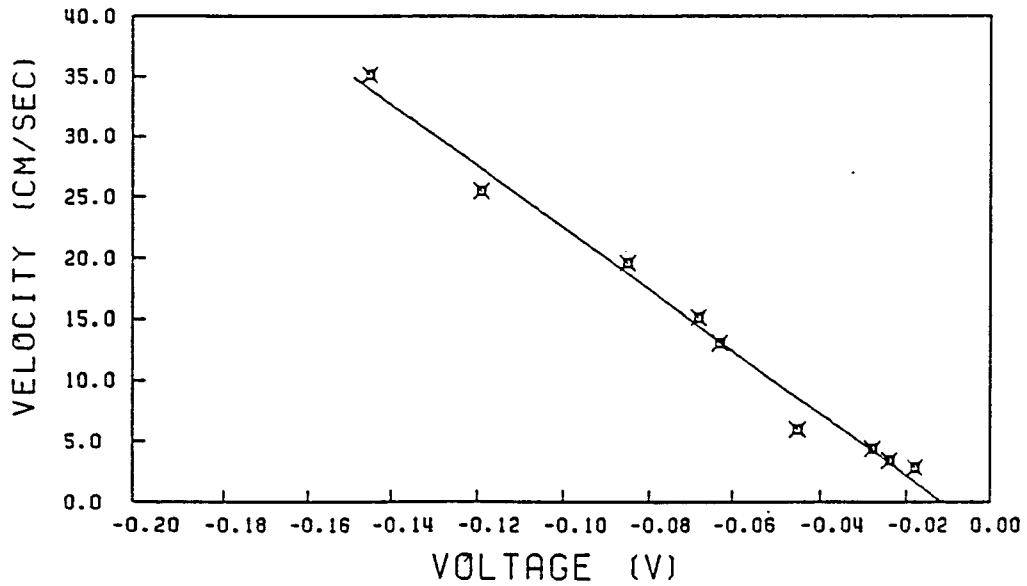


Figure 3.11: Calibration curve for the current meter

3.3.3 Pressure Transducers

Six pairs of total and pore pressure transducers were flush-mounted on the side wall of the flume at different elevations for quantifying the effective stress at different elevations. One additional total pressure transducer was installed at the flume bottom to check the weight of the column. The elevations of the 6 paired-transducers from the flume bottom were: 14cm(#1), 12cm(#2), 9.5cm(#3), 7.5cm(#4), 5.1 cm (#5), and 3.1cm(#6) for the pore pressure gauges, and 14cm(#5), 11.9cm(#7), 9.5cm(#1), 4.9cm(#3), 2.6 cm(#2), and 0cm(#6) for the total pressure gauges. The pore pressure transducers were Druck model PDCR 810, each covered with a water-saturated porous stone. Each gauge was fitted with a specially designed 300× signal amplifier. Four of the total pressure transducers were Druck model PDCR135/A/F, and the remaining three were Druck model PDCR 81, each fitted with 200× signal amplifiers. The gauges were checked in a calibration cylinder filled with water to the desired depth. The cylinder was graded with a 1 mm scale. Calibration curves for the 13 pressure transducers are shown in Figures 3.12 and 3.13. The sampling frequency during the fluidization experiments was 20 Hz, sampling duration was 30 sec for each record.

The pressure gauges were then tested under dynamic loading by subjecting them to a 1 sec period, about 5cm high wave in the flume. Measured pressures were compared with results from the linear wave theory with respect to amplitudes, as shown in Figures 3.14 and 3.15. The comparison shows that the experimental data agreed reasonably well with theory, thus indicating that the temporal response of the pressure transducers to dynamic wave loading were of acceptable quality. Phase lags appeared between the pressures from the theory and the measurements as observed in the figures, caused by the distance between the wave gauge and pressure gauges. The wave gauge was located approximately 0.6m upstream from the pressure gauges, so that the peak value of the pressure from theory was ahead of those from measurement. Between the pore and total pressure gauges there also was a small distance, plus there was the lag effect of the porous stone in the pore pressure sensor that also possibly delayed its response to the wave loading in a measurable way. These factors

also caused the peak values of pore pressure to lag behind total pressure.

All the gauges worked properly over short time scales, but when tested in still water over longer times, e.g., a day, a drift in the measurement appeared, an example of which is shown in Figure 3.17. It can be observed that during the first approximately seven hours the drift was typically more significant than at later times, so that in the fluidization experiment measurements were made after the gauges were turned on for about 7 hours. After that the measuring system became relatively stable, and most of the measurements were made within the next 9 hr period to minimize the drift.

In order to find out where the drift problem came from, a different, more reliable amplifier (Omega, model DMD 465) was used in a drift test to compare gauge response with the responses of the gauges used throughout the experiments. This drift test was also conducted in still water, and the new amplifier was used together with pore pressure gauge #2. A set of results is shown in Figure 3.16. It appears that the drift problem may not have been from the amplifier, since both the curves in the figure show similar trends in drift. The data acquisition system, or the gauges themselves might have caused this problem. Note that the accuracy of the pressure gauges stated by the suppliers was 68 Pa.

3.3.4 Data Acquisition System

In the test setup, two channels were required for wave information and thirteen for the pressure gauges. All the time-series data were collected by a Multitech personal computer via a digitizing interface card. The interface card had 16 channels for analog to digital (A/D) conversion. The A/D conversion could be triggered by Global Lab software command. The computer sampled digitized data at selected sampling intervals and stored the data into disk files. The computer scanned at 20 Hz frequency for 1 to 2 sec waves, and 40 Hz for 0.5 sec waves. Record lengths were 30 sec for pressure gauges and 1 min for wave gauges.

3.4 Flume Characterization Tests

The dimensions of the plexiglass laboratory flume were: length 20 m, width 46 cm, and height 45 cm. A programmable wave maker, which covered a large portion of the water

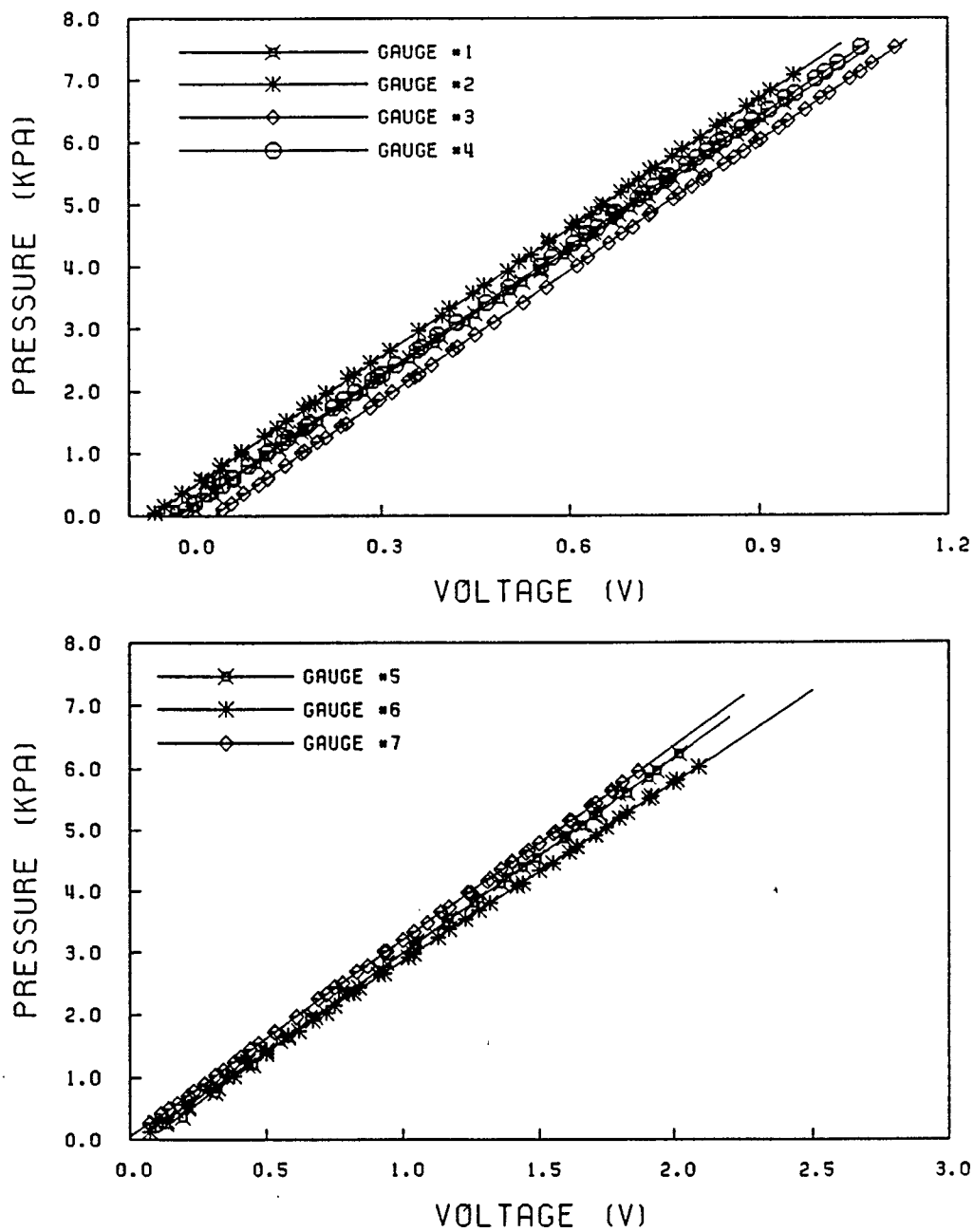


Figure 3.12: Calibration curves for the total pressure gauges

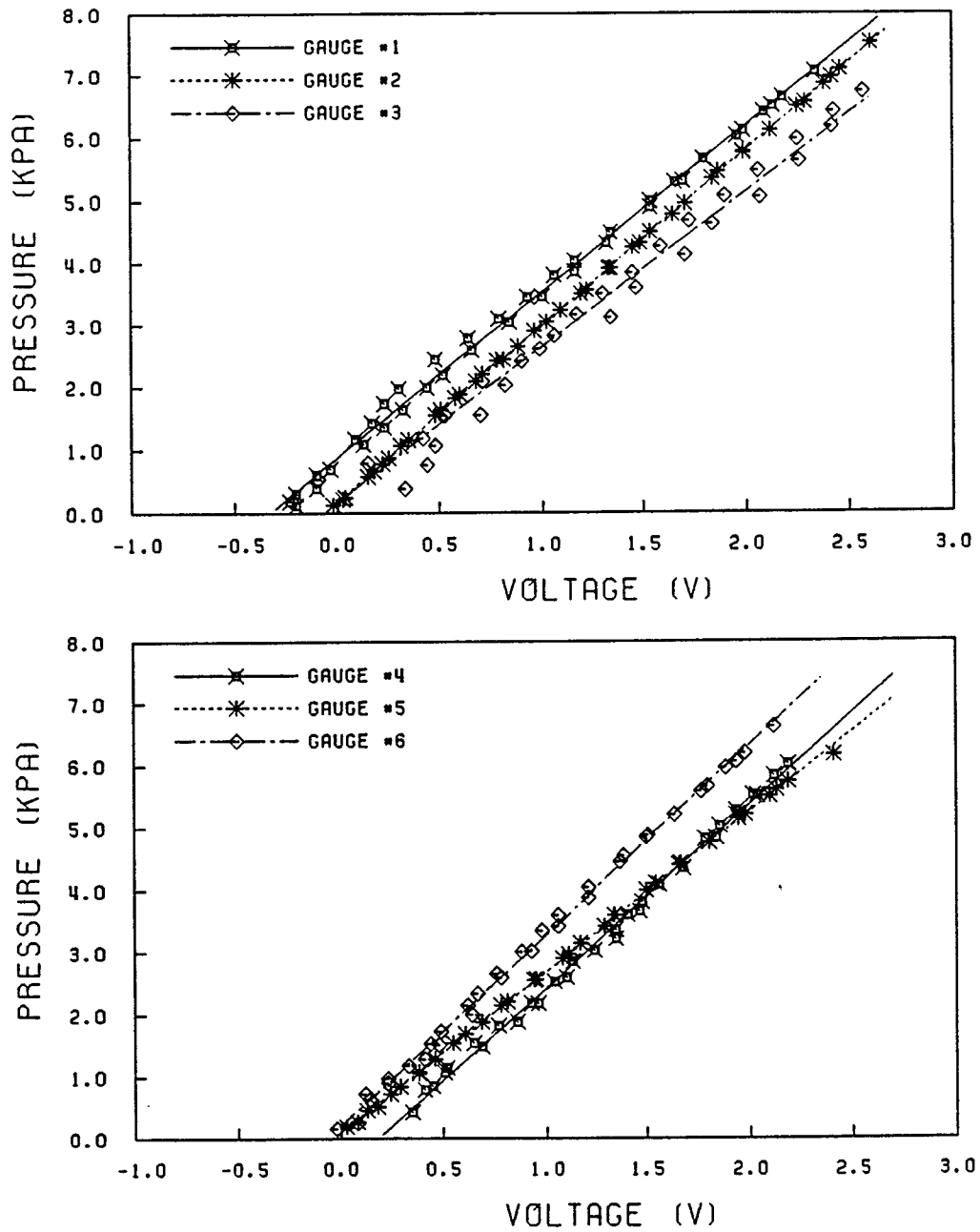


Figure 3.13: Calibration curves for the pore pressure gauges

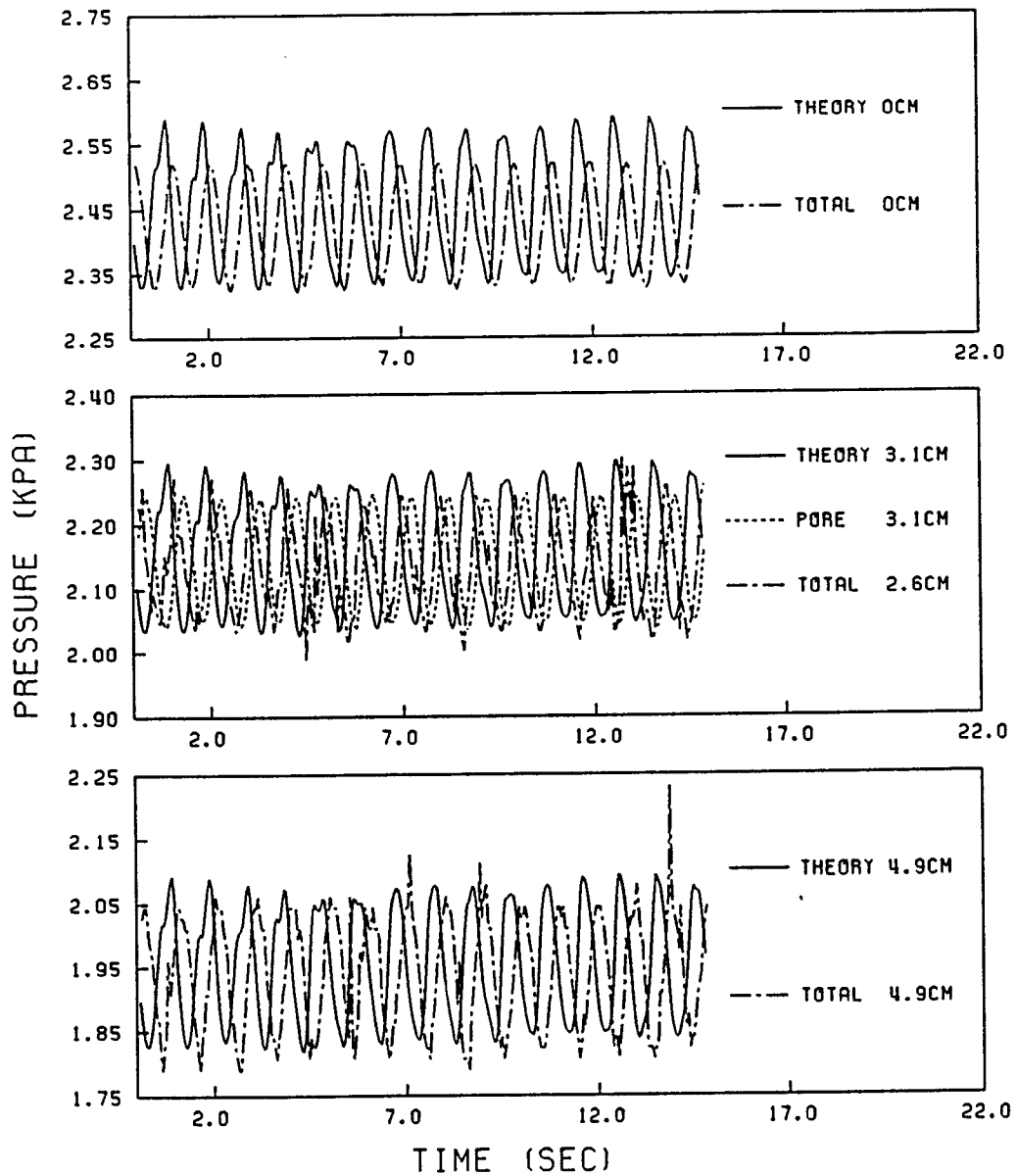


Figure 3.14: Dynamic response of pressure gauges, and comparison with results from the linear wave theory: gauge elevations ranging from 0 to 4.9 cm

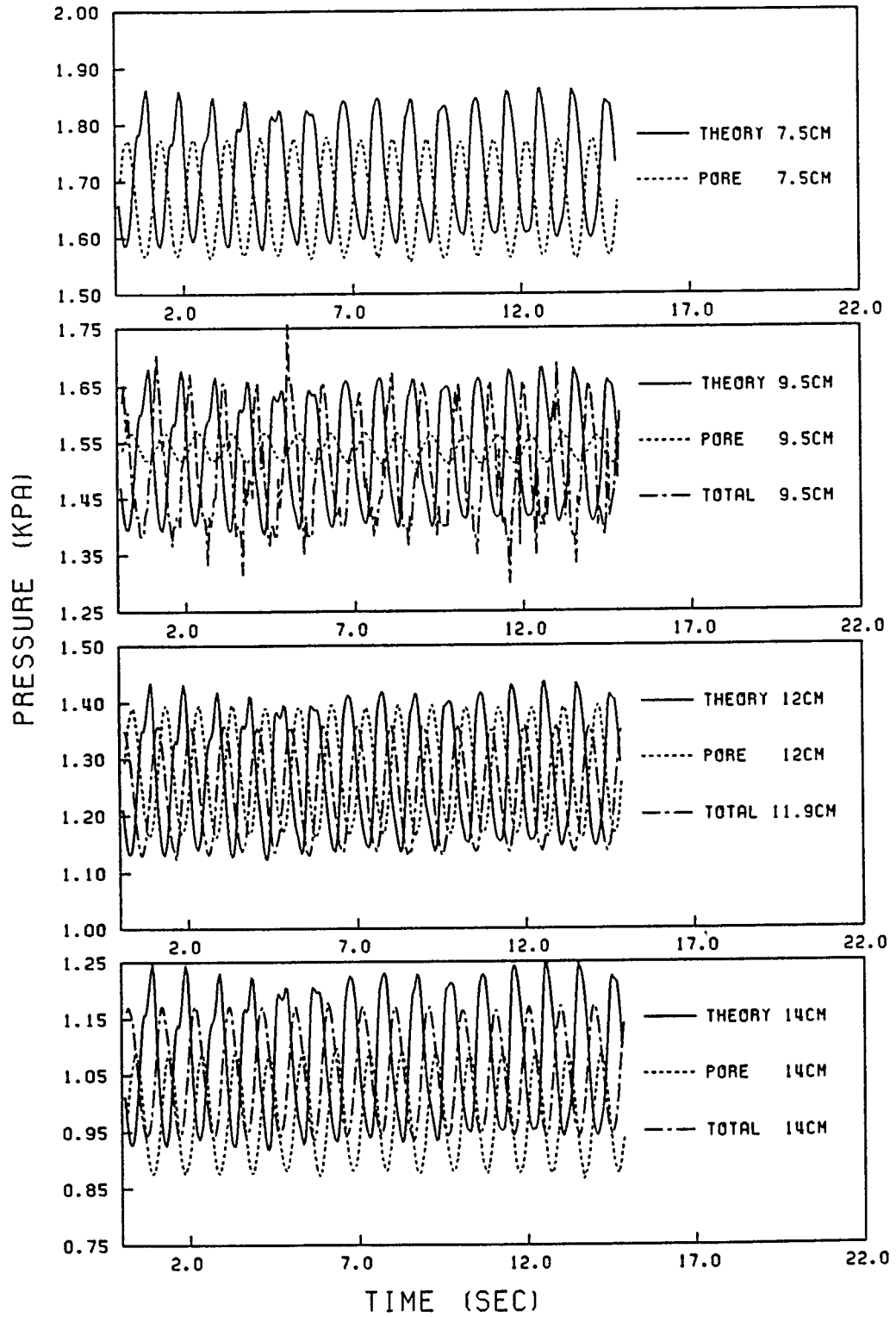


Figure 3.15: Dynamic response of pressure gauges, and comparison with results from the linear wave theory: gauge elevations ranging from 7.5 to 14 cm

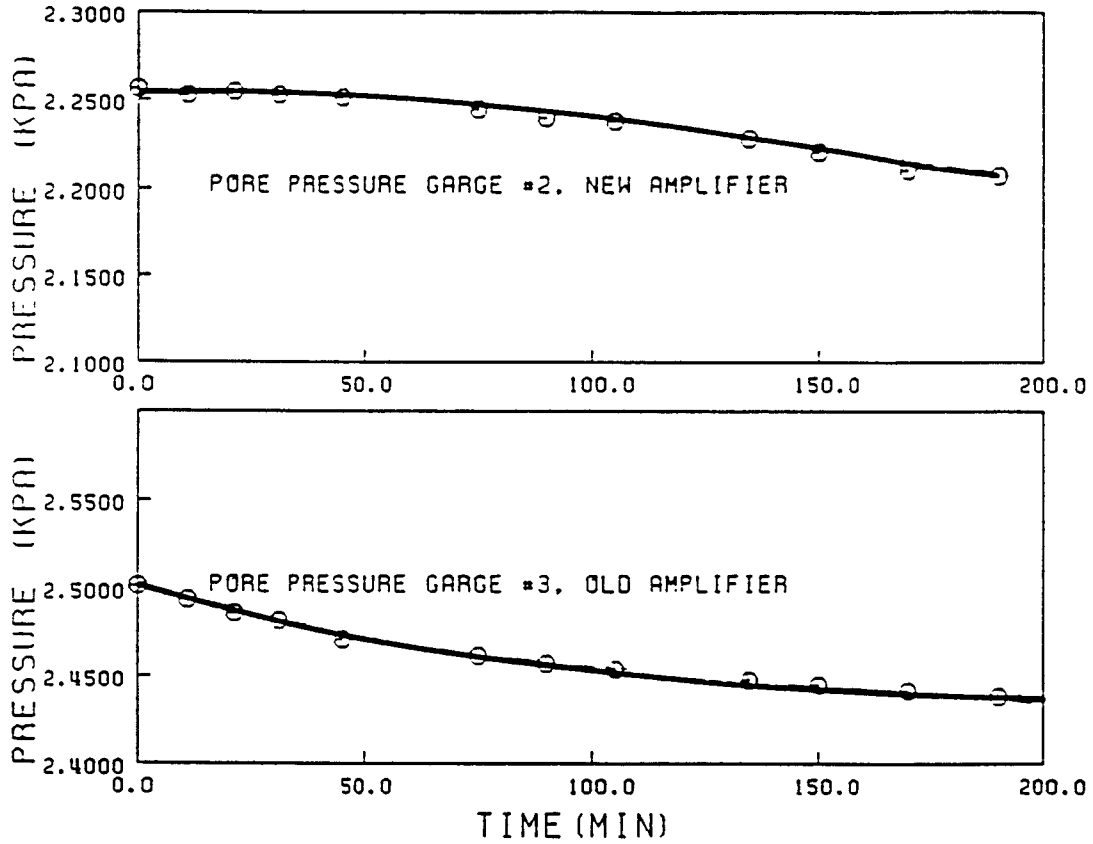


Figure 3.16: Example of instrument drift, in pore pressure measurement, with old and new amplifiers. Gauge #2 was connected to the "new" amplifier. Comparison is made with gauge #3 response connected to the "old" amplifier

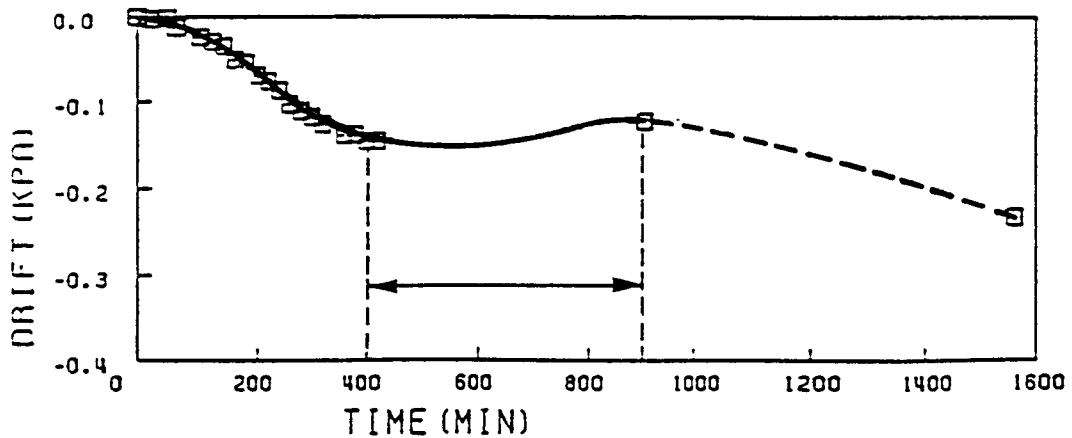


Figure 3.17: Example of instrument drift, pore pressure gauge #1, Time range over which most of the pressure data were obtained is indicated.

column and moved in the piston-type manner, was installed at one end of the flume to generate regular (monochromatic) waves. The wave height and period could be adjusted by a DC motor controller. An impermeable, 1 in 4 sloped beach covered with astroturf, a type of plastic wire mesh about 1 cm thick, was installed at the end behind the wave maker to damp out water level fluctuations caused there by the wave maker. At the downstream end of the flume, a plexiglass board was installed to provide a 1 in 20 sloped beach. Astroturf was also placed on top of this beach for reduction of wave reflection. In the test section, a trench, from $x=6.1$ m to 13.3 m (Figure 3.18), with a height of 14 cm and side slopes of 1 in 12, was formed to hold the sediment. Here x is the distance measured from the wave maker as shown in Figure 3.18.

Before the mud fluidization experiments were carried out in the flume, wave performance in the flume, without mud, was examined in order to characterize flume hydrodynamics and to define the domain of flume operation for the next phase of the work. For this purpose a false bottom made of plywood was introduced to cover up the trench, as shown in Figure 3.18. The data obtained were used to determine the optimal ranges of the wave height, wave period and water depth within which the waves seemed reasonably well behaved, and the ranges over which significant higher harmonics occurred. In the characterization test, two wave gauges and a current meter were used to record wave heights and horizontal current velocities, respectively. As shown in Figure 3.18, one gauge was set up at the upstream end of the test section, and the other was approximately in the middle. The distance between the two gauges was 5 m.

3.4.1 Test Conditions

Two water depths, 15 and 20 cm, were selected for this experiment. For each depth two wave heights were chosen, and the periods were 0.5s, 1.0s, 1.5s and 2.0s. A total of 15 tests were conducted, as noted in Table 3.13. Examples of 1 sec wave time-series at 20 cm water depth are shown in Figures 3.19, where H refers to wave height.

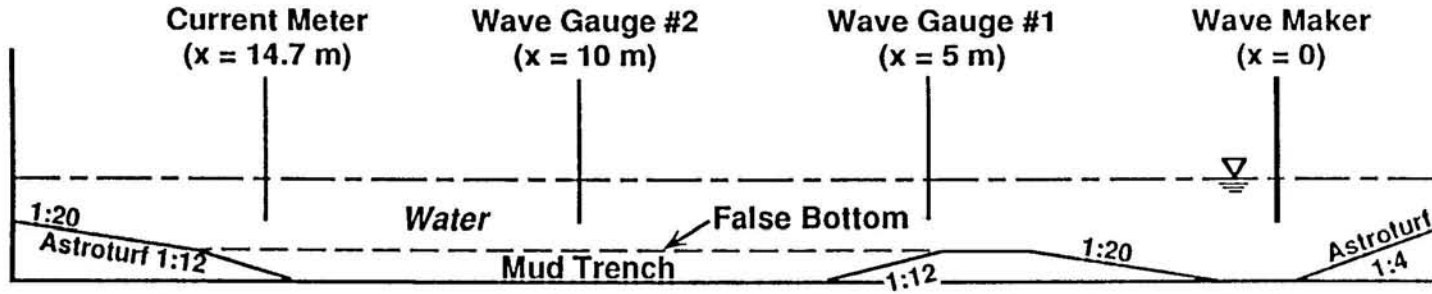


Figure 3.18: Wave flume elevation profile and instrument locations

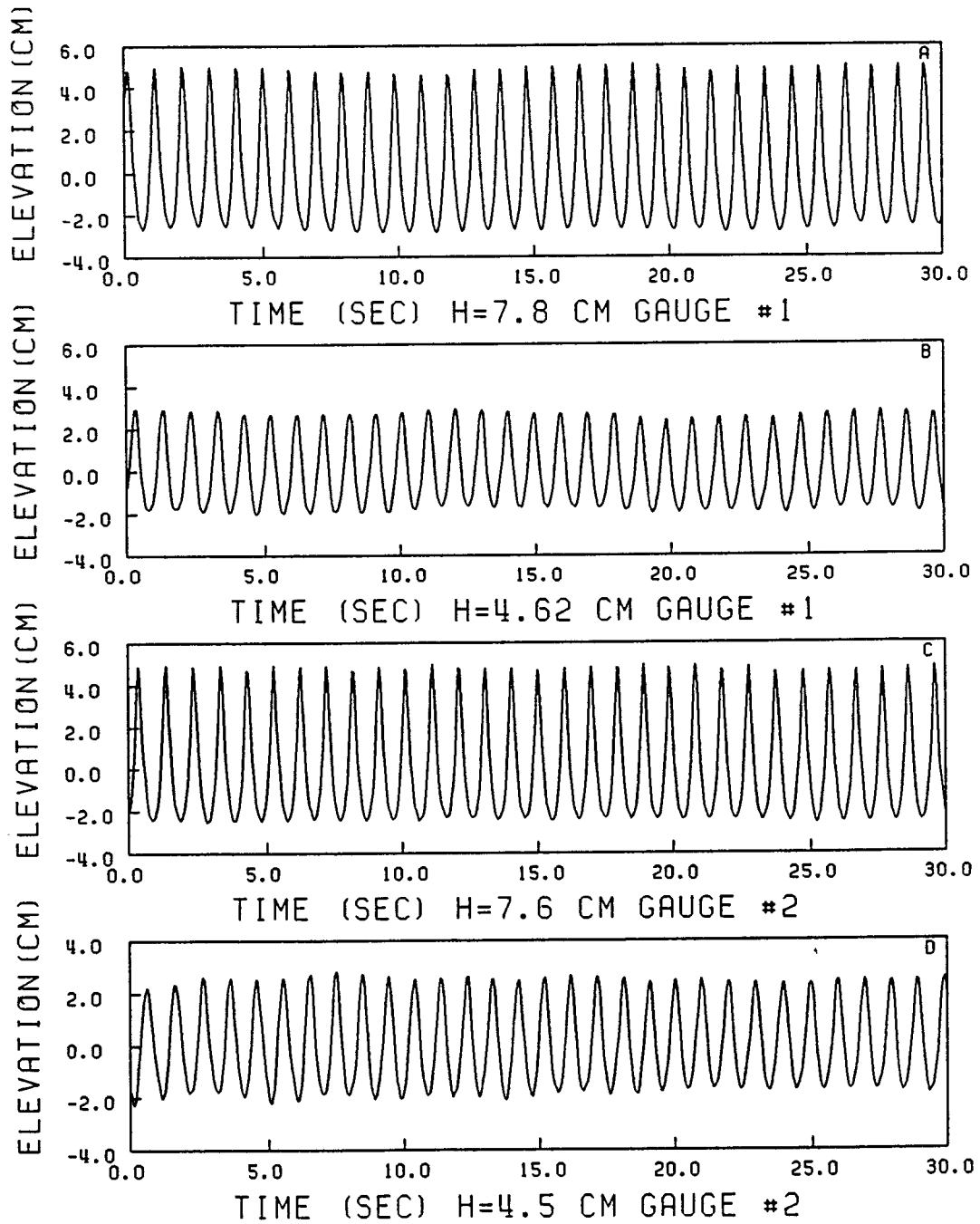


Figure 3.19: Examples of wave time-series (depth=20cm, period=1.0s) for flume characterization tests with a false bottom

Table 3.13: Wave conditions for the characterization tests

Depth (cm)	Period T(sec)	Wave height H(cm)	
		gauge #1	gauge #2
15	0.5	2.7	2.3
15	0.5	4.2	3.7
15	1.0	2.3	2.3
15	1.0	5.0	4.8
15	1.5	2.7	2.5
15	1.5	5.0	4.9
15	2.0	2.7	2.4
15	2.0	4.9	4.2
20	0.5	3.1	2.7
20	1.0	4.6	4.3
20	1.0	7.8	7.6
20	1.5	4.4	4.5
20	1.5	9.1	9.2
20	2.0	4.3	3.9
20	2.0	8.4	6.4

3.4.2 Wave Spectra

The wave spectrum for each wave condition was obtained from the time-series. Some examples of spectra given in Figures 3.20 and 3.21 indicate that among all the selected frequencies, 1 Hz waves had the highest fundamental harmonic, and comparatively very small higher harmonics. For the same water depth and wave height, a second harmonic wave appeared as the wave period increased. When the wave period was increased to 2 seconds, the wave became visually non-linear, and there were two or even three dominant wave components. For the same depth and wave period, when the wave height increased, the second harmonic became more pronounced. Also for the same wave height and period, the deeper the water, the lesser was the magnitude of the second harmonic.

3.4.3 Wave Reflection Estimation

Goda and Suzuki (1976) developed an experimental technique for the resolution of incident and reflected waves in continuous runs in the absence of multi-reflections of irregular waves between the wave maker and a reflective (beach) structure. This method was used in the present study to calculate the wave reflection coefficients, in order to assess the

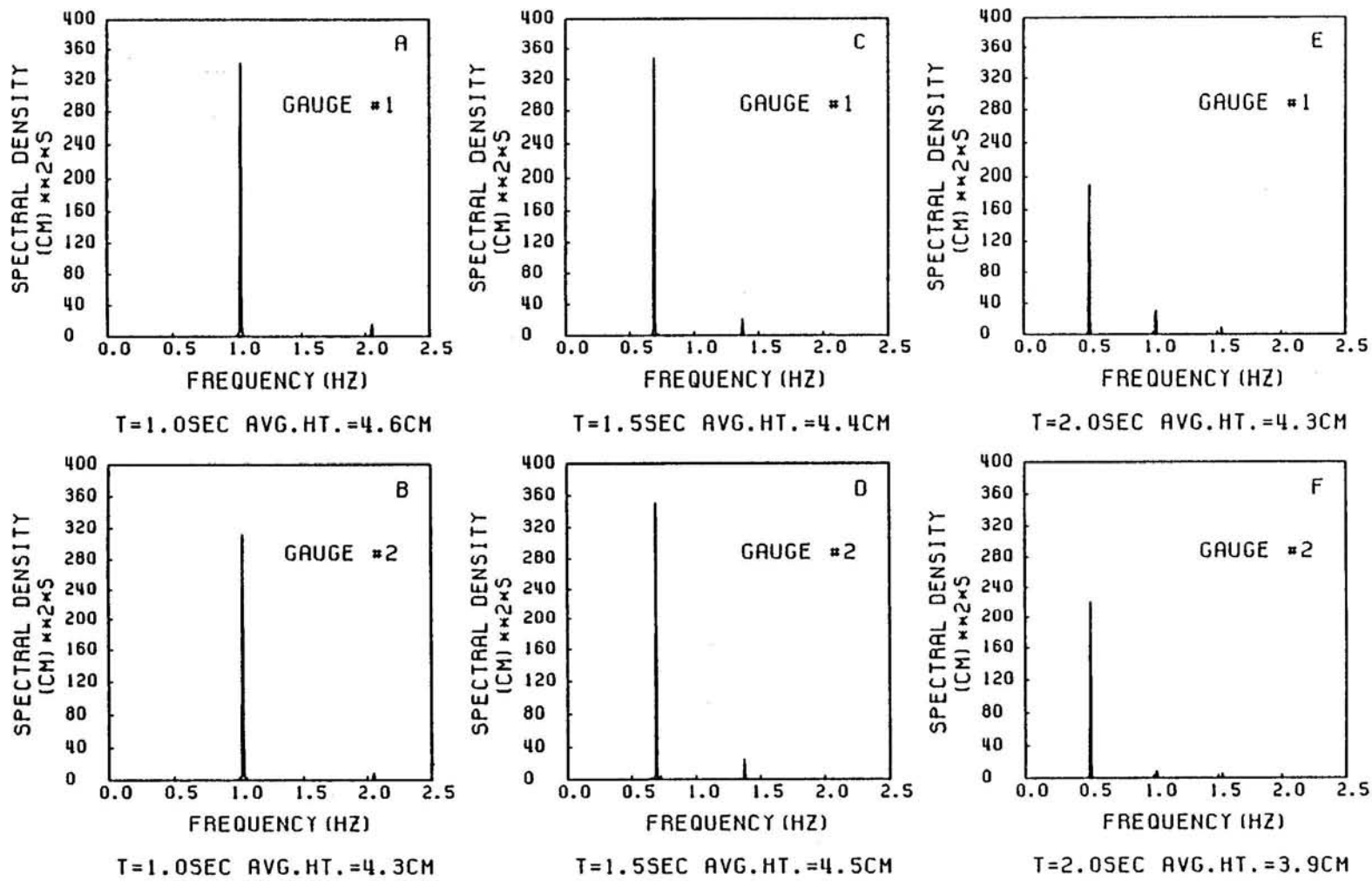


Figure 3.20: Wave spectra, water depth=20cm; average wave height ranging from 3.9 to 4.6 cm, period ranging from 1 to 2 sec.

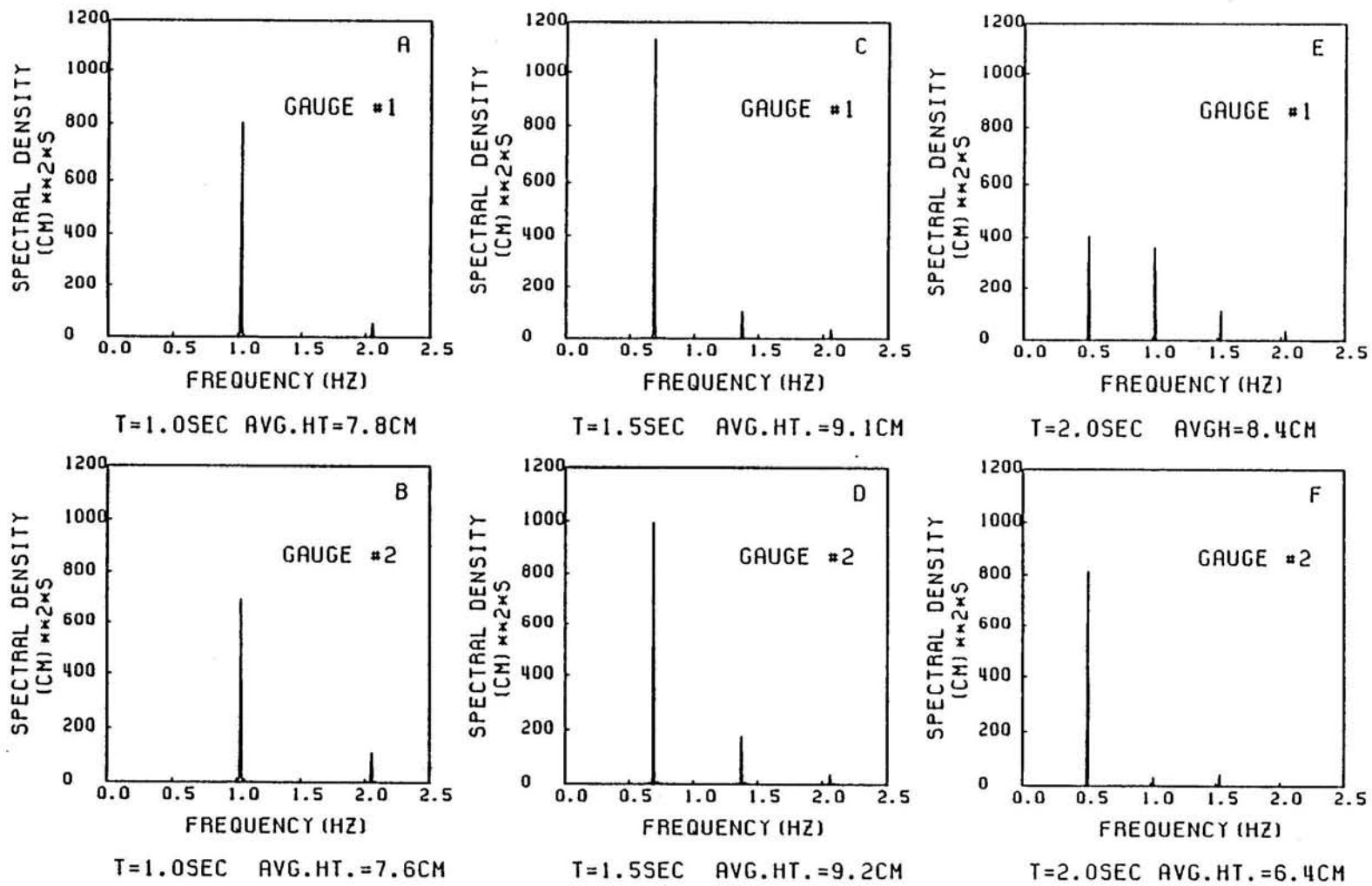


Figure 3.21: Wave spectra, water depth=20cm; average wave height ranging from 6.4 to 9.1 cm, period ranging from 1 to 2 sec.

progressive character of the waves. The principle is briefly described next.

The incident wave and the reflected wave are described in the general forms of

$$\begin{aligned}\eta_I &= a_I \cos(kx - \sigma t + \varepsilon_I) \\ \eta_R &= a_R \cos(kx + \sigma t + \varepsilon_R)\end{aligned}\quad (3.13)$$

where η_I and η_R are the surface elevations of the incident and the reflected waves, respectively, a_I is the amplitude of the incident wave and a_R is that of reflected wave, k is the wave number, $2\pi/L$, with L the wavelength, σ is the angular frequency, $2\pi/T$, with T the wave period, and ε_I and ε_R are the phase angles of the incident and the reflected waves, respectively. The surface elevations must be recorded at two adjacent stations, x_1 and $x_2 = x_1 + \Delta l$. The measured profiles of the composite waves, selecting the fundamental frequency for analysis, are

$$\begin{aligned}\eta_1 &= (\eta_I + \eta_R)_{x=x_1} = A_1 \cos \sigma t + B_1 \sin \sigma t \\ \eta_2 &= (\eta_I + \eta_R)_{x=x_2} = A_2 \cos \sigma t + B_2 \sin \sigma t\end{aligned}\quad (3.14)$$

where

$$\begin{aligned}A_1 &= a_I \cos \phi_I + a_R \cos \phi_R \\ B_1 &= a_I \sin \phi_I - a_R \sin \phi_R \\ A_2 &= a_I \cos(k\Delta l + \phi_I) + a_R \cos(k\Delta l + \phi_R) \\ B_2 &= a_I \sin(k\Delta l + \phi_I) + a_R \sin(k\Delta l + \phi_R)\end{aligned}\quad (3.15)$$

$$\phi_I = kx_1 + \varepsilon_I$$

$$\phi_R = kx_1 + \varepsilon_R\quad (3.16)$$

Equation 3.15 can be solved to yield a_I and a_R according to

$$\begin{aligned}a_I &= \frac{\sqrt{(A_2 - A_1 \cos k\Delta l - B_1 \sin k\Delta l)^2 + (B_2 + A_1 \sin k\Delta l - B_1 \cos k\Delta l)^2}}{2 |\sin k\Delta l|} \\ a_R &= \frac{\sqrt{(A_2 - A_1 \cos k\Delta l + B_1 \sin k\Delta l)^2 + (B_2 - A_1 \sin k\Delta l - B_1 \cos k\Delta l)^2}}{2 |\sin k\Delta l|}\end{aligned}\quad (3.17)$$

Using Fourier analysis enables the estimation of the amplitudes A_1 , B_1 , A_2 and B_2 for the fundamental frequency. The amplitudes of the incident and the reflected waves, a_I and a_R , are then estimated from Equation 3.17. Table 3.14 gives the reflection coefficients, $k_r = a_R/a_I$, for the two series experiments, with water depths of 15 and 20 cm. This table shows that at a water depth of 20 cm and a frequency of 1 Hz, the wave reflection coefficient was less than 0.3, which could be considered to mean that the waves under these conditions were generally of the progressive type. For this reason as well as another cited previously, in the fluidization experiments described in Chapter 5, the chosen wave frequency was 1 Hz. The range of water depth was selected from 16 to 20 cm. The waves under these conditions were found to be acceptably well behaved, even when the false bottom was removed and the trench filled with mud.

Table 3.14: Wave reflection coefficient, k_r

Depth (cm)	Period (sec)	Wave height(cm)	k_r
15	1.0	2.3	0.48
15	1.0	4.8	0.37
15	1.5	2.5	0.81
15	1.5	4.9	0.18
15	2.0	2.4	0.59
15	2.0	4.2	0.52
20	1.0	4.3	0.30
20	1.0	7.6	0.17
20	1.5	4.5	0.24
20	1.5	9.2	0.51
20	2.0	3.9	0.11
20	2.0	6.4	0.35

3.4.4 Current Velocity

For each selected wave condition the horizontal current velocity was measured at elevations of 2.6 cm, 4.6 cm, 6.6 cm, 8.6 cm and 9.6 cm from the bottom of the flume. These velocities were then compared with those calculated from the linear wave theory. Considering the 4.7 m distance between the current meter and wave gauge #2, it should be noted that there was measurable wave dissipation over this distance, even in the absence of mud.

The mean wave decay coefficient, k_{im} , was found to be 0.02/m, as calculated from the wave height recordings by gauges #1 and #2. The wave height where the current meter was located, H_{cur} , would be

$$H_{cur} = H_{\#2} e^{-k_{im} \Delta x} \quad (3.18)$$

where $H_{\#2}$ is the wave height at gauge #2, and Δx is the distance between gauge #2 and the current meter. Here $\Delta x = 4.7$ m.

The root-mean square (rms) velocity from the current velocity time-series is obtained from

$$u_{rms} = \sqrt{\frac{1}{N} \sum_{i=1}^N (u_i - \bar{u})^2} \quad (3.19)$$

where u_i is the instantaneous velocity and \bar{u} is the time-mean velocity. According to the linear wave theory (Dean & Dalrymple, 1984), the horizontal orbital current velocity under a wave is

$$u = \frac{H_{cur} \sigma \cosh kz}{2 \sinh kh} \cos(kx - \sigma t) \quad (3.20)$$

where H the wave height, σ the angular frequency, k the wave number, h the water depth, and z the elevation above the flume bottom. Thus u_{rms} amplitude can be calculated as (van Rijn, 1985)

$$u_{rms} = \frac{\sqrt{2} H_{cur} \sigma \cosh kz}{2 \sinh kh} \quad (3.21)$$

As shown by examples in Figure 3.22, at $T=1$ sec the measured velocities agreed well with theory. At $T=2$ sec, the measured velocities (not shown) were about 50% larger than those from theory, because the 2 sec wave was not quite linear. At $T=1.5$ sec the two results did not agree well either for the same reason. The two curves in Figure 3.22 represent the results from the theory. The solid curve includes wave dissipation, while the dashed one does not, i.e., k_{im} in Equation 3.18 is 0.02/m for calculating H_{cur} for the solid curve and is zero for the dashed curve.

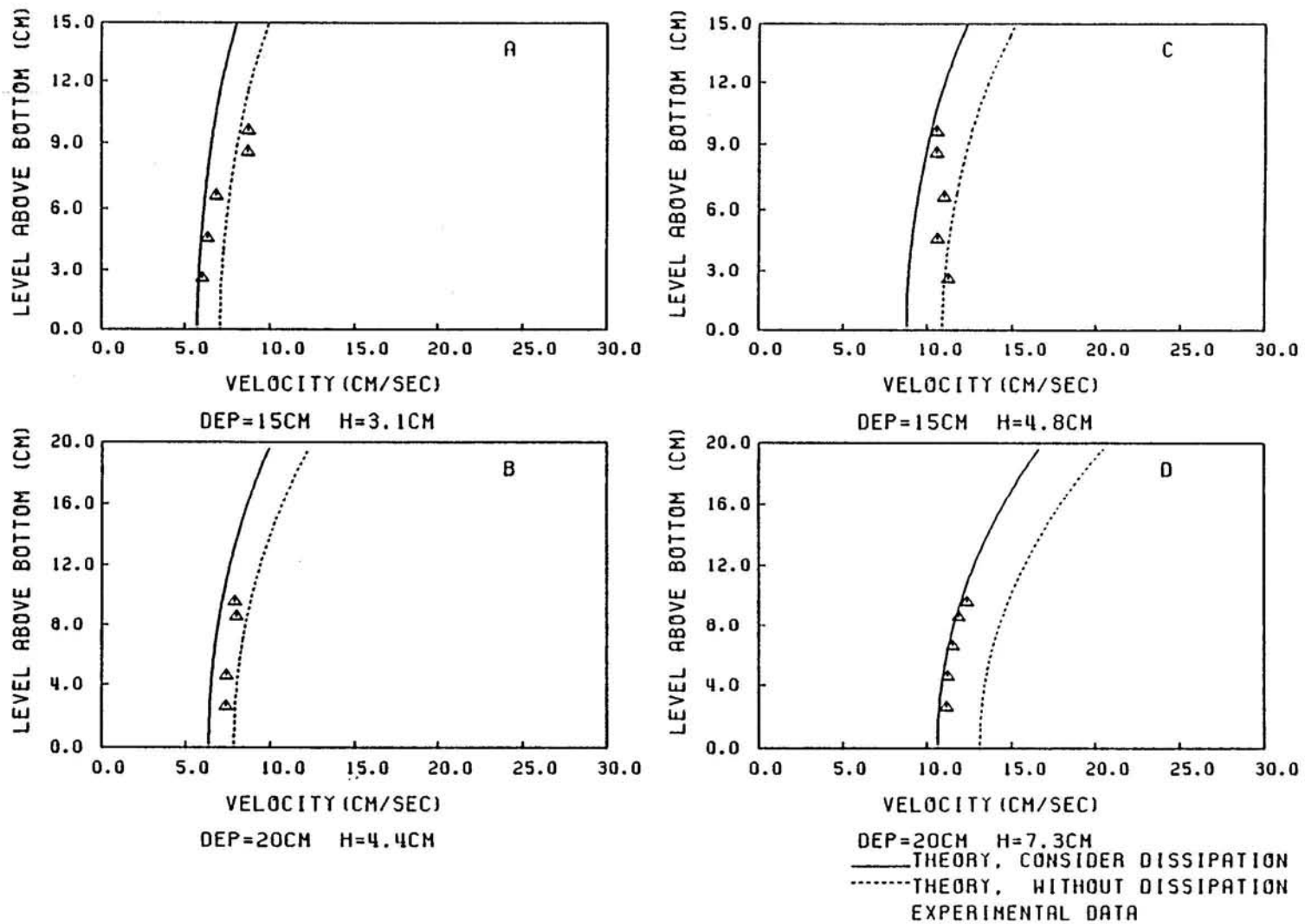


Figure 3.22: Horizontal velocity profiles: comparison between experimental data (rms amplitudes) and linear wave theory (period $T=1.0s$)

CHAPTER 4 ESTIMATIONS OF FLUID MUD THICKNESS AND WAVE ENERGY DISSIPATION

4.1 Introduction

A previously developed shallow water wave-mud interaction model (Jiang & Mehta, 1991) was used to calculate the rate of wave energy dissipation and an effective fluid mud thickness during the fluidization process. This model considers a two-layered mud/water system forced by a progressive, non-breaking surface wave of periodicity specified by frequency σ , as depicted in Figure 4.1. In the upper water column of thickness H_1 , in which the pressure and inertia forces are typically dominant in governing water motion and the flow field is practically irrotational, sediment concentration usually tends to be quite low, so that the suspension density, ρ_1 , is close to that of water which is considered to be inviscid. The lower column is a homogeneous layer of fluid mud having a thickness of H_2 , density ρ_2 and dynamic viscosity μ . This last assumption of mud having fluid properties to begin with is a noteworthy limitation of the simple model description chosen, some consequences of which are discussed later. Likewise, the shallow water assumption proved to be yet another limitation, since the data were obtained in the intermediate water range for practical reasons. Finally, a third limitation arose from the fact that while the model assumed constant properties (density, viscosity) in the mud layer. These properties varied with depth in the experiments. Some horizontal variations, also ignored in the model, were significant as well, e.g., the model surface elevation.

4.2 Effective Sheared Mud Thickness

The surface and interface variations about their respective mean values are $\eta_1(x, t)$ and $\eta_2(x, t)$. The amplitude of a simple harmonic surface wave is assumed to be small enough

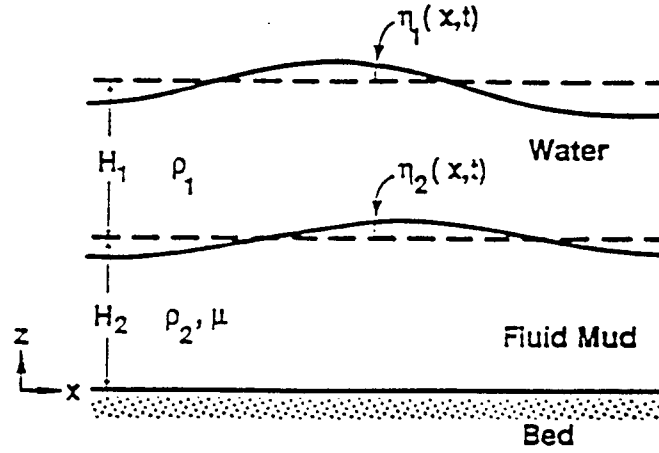


Figure 4.1: Two-layered water-fluid mud system subjected to progressive wave action to conform to the linear theory, as also the response of the mud layer. Accordingly, the relevant linear governing equations of motion and continuity can be written as:

upper layer:

$$\frac{\partial u_1}{\partial t} + g \frac{\partial \eta_1}{\partial x} = 0 \quad (4.1)$$

$$\frac{\partial(\eta_1 - \eta_2)}{\partial t} + H_1 \frac{\partial u_1}{\partial x} = 0 \quad (4.2)$$

lower layer:

$$\frac{\partial u_2}{\partial t} + rg \frac{\partial \eta_2}{\partial x} + (1 - r)g \frac{\partial \eta_1}{\partial x} = \nu \frac{\partial^2 u_2}{\partial z^2} \quad (4.3)$$

$$\int_0^1 \frac{\partial u_2}{\partial x} dz + \frac{\partial \eta_2}{\partial t} = 0 \quad (4.4)$$

where $u_1(x, t)$, $u_2(x, t)$ are the wave-induced velocities, $h = H_2 + \eta_2$, $r = (\rho_2 - \rho_1)/\rho_2$ is the normalized density jump, and $\nu = \mu/\rho_2$ is the kinematic viscosity of mud.

The following boundary conditions are imposed:

$$\eta_1(0, t) = a_0 \cos \sigma t \quad (4.5)$$

$$u_1(\infty, t), u_2(\infty, z, t), \eta_1(\infty, t), \eta_2(\infty, t) \rightarrow 0 \quad (4.6)$$

$$u_2(x, 0, t) = 0 \quad (4.7)$$

$$\frac{\partial u_2(x, H_2, t)}{\partial z} = 0 \quad (4.8)$$

where $a_0(= H/2)$ is the surface wave amplitude at $x = 0$. Equation 4.5 specifies the surface wave form, Equation 4.6 represents the fact that, due to viscous dissipation, all motion must cease at an infinite distance, Equation 4.7 is the non-slip bottom boundary condition, and Equation 4.8 states that because the upper layer fluid is inviscid, there can be no stress at the interface.

Solutions (Jiang & Mehta, 1991) give the normalized wave number, $\tilde{k} = kH_1$, which is a complex valued function

$$\frac{\tilde{k}}{F_r} = \left\{ \frac{1 + \tilde{H}_2\Gamma - [(1 + \tilde{H}_2\Gamma)^2 - 4r\tilde{H}_2\Gamma]^{1/2}}{2r\tilde{H}_2\Gamma} \right\}^{1/2} \quad (4.9)$$

where

$$\Gamma = 1 - \frac{\tanh(m\tilde{H}_2)}{m\tilde{H}_2} \quad (4.10)$$

$\tilde{H}_2 = H_2/H_1$, $m = (-iRe)^{1/2}$, $Re = \sigma H_1^2/\nu$ is the wave Reynolds number and $F_r = \sigma(H_1/g)^{1/2}$ is the wave Froude number, σ is the wave angular frequency.

The imaginary part of k , i.e., k_i , is the wave attenuation (decay or damping) coefficient with respect to the travel distance x , defined by

$$a_x = a_0 \exp(-k_i x) \quad (4.11)$$

where a_x is the wave amplitude at any x . Also the normalized, horizontal wave-induced velocity in a mud layer is given as

$$\tilde{u}_2 = A \frac{\tilde{k}}{F_r^2} \left\{ 1 - r \left(\frac{\tilde{k}}{F_r} \right)^2 \right\} \left\{ 1 - \cosh(m\tilde{z}) + \tanh(m\tilde{H}_2) \cdot \sinh(m\tilde{z}) \right\} \exp\{i(\tilde{k}\tilde{x} - \tilde{t})\} \quad (4.12)$$

where $\tilde{u}_2 = u_2/(\sigma H_1)$, $A = a_0/H_1$, $\tilde{z} = z/H_1$, and $\tilde{x} = x/H_1$.

As noted in Section 3.2.1 in Chapter 3, the dynamic viscosity of mud can be expressed as

$$\mu = \mu_\infty + c\dot{\gamma}^{n-1} \quad (4.13)$$

where μ_∞ , c and n are constants for a given material, and $\dot{\gamma}$ is the shear rate.

With the two recorded wave amplitudes a_0 ($=H_{\#1}/2$ at gauge #1) and a_x ($=H_{\#2}/2$ at gauge #2) from the experiment, the wave dissipation coefficient, k_i , could be calculated from Equation 4.11. By equating this k_i with the model result from Equation 4.9, the viscosity, μ , was determined. Then from Equation 4.13 a representative shear rate in the mud layer corresponding to this viscosity, $\dot{\gamma}_s$, was calculated. Also, by substituting the viscosity, μ (or $\nu = \mu/\rho_2$), into Equation 4.12, an effective sheared mud thickness, d , was obtained from the equation:

$$d = \frac{u_{2s}}{\dot{\gamma}_s} = \frac{\tilde{u}_{2s}\sigma H_1}{\dot{\gamma}_s} \quad (4.14)$$

where u_{2s} is the amplitude of u_2 at the mud surface and $\tilde{u}_{2s} = u_{2s}/(\sigma H_1)$ is the normalized value of U_{2S} . Note that this is a very approximate procedure, particularly because the experiments were not conducted with a fully fluidized mud, as assumed in the model, and, furthermore, the mud properties were assumed to be depth-invariant in the model, which was not the case in the experiment. Nevertheless, the objective was to examine if d was related in any way to the mud fluidization depth obtained from the pressure measurements, as described in Chapter 5. The process for the calculation of d is illustrated in Figure 4.2, in which $\dot{\gamma}_0$ is an initially selected value of *gamma* required for iterative calculation of $\dot{\gamma}_s$.

A physical implication of Equation 4.14 is that, assuming $d < H_2$, u_2 will be zero at elevation $z = H_2 - d$. This requirement is not compatible with the fact that u_2 in the model is consistently equal to zero only at the flume bottom, i.e., $z = 0$. Thus the attempt to calculate a fluidized mud thickness, d , within a layer of thickness H_2 that is already a fluid, by definition in the model, is an artifact meant only to experiment with the possibility of evaluating the fluidization depth that is commensurate with the experimental data. This attempt at developing correspondence between the model and the data is necessitated by the fact that the mud in the flume was not in general a fluid, except in the upper elevations when fluidization occurred by virtue of wave action.

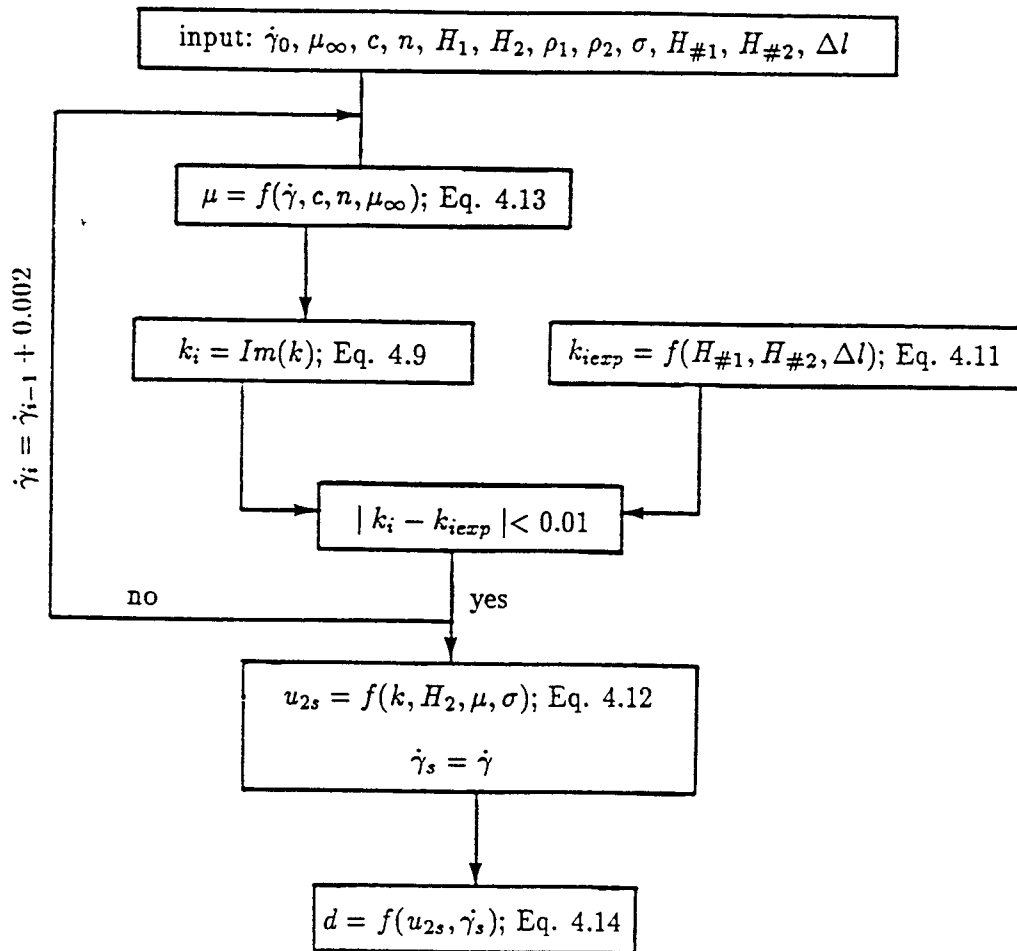


Figure 4.2: Diagram of calculation process for effective sheared mud thickness, d

4.3 Wave Energy Dissipation Rate

The wave-mean rate of energy dissipation with respect to time, ε_D , is given by (Dean & Dalrymple, 1984):

$$\varepsilon_D = \rho\nu \int_0^{H_1+H_2} \overline{[2(\frac{\partial u}{\partial x})^2 + (\frac{\partial w}{\partial x} + \frac{\partial u}{\partial z})^2]} dz \quad (4.15)$$

where the overbar indicates wave-mean value. Note that since the water layer is assumed to be inviscid, wave dissipation in this layer is theoretically zero. The integration was therefore carried out only over the mud layer of thickness H_2 . For the two-dimensional shallow water model, the vertical velocity, w , is ignored. Thus Equation 4.15 can be simplified as:

$$\varepsilon_D = \rho_2\nu \int_0^{H_2} \overline{[2(\frac{\partial u_2}{\partial x})^2 + (\frac{\partial u_2}{\partial z})^2]} dz \quad (4.16)$$

or, dividing ε_D into two terms:

$$\varepsilon_D = \varepsilon_{D1} + \varepsilon_{D2} \quad (4.17)$$

$$\varepsilon_{D1} = \rho_2\nu \int_0^{H_2} \overline{2(\frac{\partial u_2}{\partial x})^2} dz \quad (4.18)$$

$$\varepsilon_{D2} = \rho_2\nu \int_0^{H_2} \overline{(\frac{\partial u_2}{\partial z})^2} dz \quad (4.19)$$

Physically, ε_{D1} and ε_{D2} are the wave-mean rates of energy dissipation due to the horizontal and vertical velocity gradients, respectively. Equation 4.12 gives:

$$\frac{\partial u_2}{\partial x} = \sigma \frac{\partial \bar{u}_2}{\partial \bar{x}} = \sigma(i\bar{k})\bar{u}_2 \quad (4.20)$$

and

$$\frac{\partial u_2}{\partial z} = \sigma \frac{\partial \bar{u}_2}{\partial \bar{z}} = \sigma A \frac{\bar{k}}{F_r^2} \{1 - r(\frac{\bar{k}}{F_r})^2\} \{-m \sinh(m\bar{z}) + m \tanh(m\bar{z}) \cosh(m\bar{z})\} \exp i(\bar{k}\bar{x} - \bar{t}) \quad (4.21)$$

Therefore, the time-averaged values of $(\frac{\partial u_2}{\partial x})^2$, $(\frac{\partial u_2}{\partial z})^2$ are:

$$\overline{(\frac{\partial u_2}{\partial x})^2} = \frac{1}{2} \sigma^2 \bar{k}^2 (\frac{A\bar{k}}{F_r^2})^2 \{1 - r(\frac{\bar{k}}{F_r})^2\}^2 \cdot \{1 - \cosh(m\bar{z}) + \tanh(m\bar{H}_2) \sinh(m\bar{z})\}^2 \quad (4.22)$$

and

$$\begin{aligned} \overline{(\frac{\partial u_2}{\partial z})^2} &= \frac{1}{2} m^2 \sigma^2 (\frac{A\bar{k}}{F_r^2})^2 \{1 - r(\frac{\bar{k}}{F_r})^2\}^2 \left\{ \frac{\tanh^2(m\bar{H}_2) - 1}{2} \right. \\ &\quad \left. + \frac{\tanh^2(m\bar{H}_2) + 1}{2} \cosh(2m\bar{z}) - \tanh(m\bar{H}_2) \sinh(2m\bar{z}) \right\} \end{aligned} \quad (4.23)$$

Therefore

$$\begin{aligned}
\varepsilon_{D1} &= 2\rho_2\nu \int_0^{H_2} \overline{\left(\frac{\partial u_2}{\partial x}\right)^2} dz = 2\rho_2\nu \int_0^{\tilde{H}_2} H_1 \overline{\left(\frac{\partial u_2}{\partial x}\right)^2} d\tilde{z} \\
&= 2\rho_2\nu H_1 \sigma^2 \bar{k}^2 \left(\frac{A\bar{k}}{F_r^2}\right)^2 \left\{1 - r\left(\frac{\bar{k}}{F_r}\right)^2\right\} \\
&\left\{\frac{3}{2}\tilde{H}_2 - \frac{1}{2}\tilde{H}_2 \tanh^2(m\tilde{H}_2) + \frac{2 \tanh(m\tilde{H}_2)}{m} [\cosh(m\tilde{H}_2) - 1] \right. \\
&\quad \left. - \frac{\tanh(m\tilde{H}_2)}{2m} [\cosh(2m\tilde{H}_2) - 1] - \frac{2}{m} \sinh(m\tilde{H}_2) \right. \\
&\quad \left. + \frac{1 + \tanh^2(m\tilde{H}_2)}{4m} \sinh(2m\tilde{H}_2)\right\} \tag{4.24}
\end{aligned}$$

and

$$\begin{aligned}
\varepsilon_{D2} &= \rho_2\nu \int_0^{\tilde{H}_2} H_2 \overline{\left(\frac{\partial u_2}{\partial z}\right)^2} dz \tag{4.25} \\
&= \frac{1}{2}\rho_2\nu H_1 m^2 \sigma^2 \left(\frac{A\bar{k}}{F_r^2}\right)^2 \left\{1 - r\left(\frac{\bar{k}}{F_r}\right)^2\right\}^2 \\
&\left\{\frac{\tanh^2(m\tilde{H}_2) - 1}{2} \tilde{H}_2 + \frac{1 + \tanh^2(m\tilde{H}_2)}{4m} \sinh(2m\tilde{H}_2) \right. \\
&\quad \left. - \frac{1}{2m} \tanh(m\tilde{H}_2) [\cosh(2m\tilde{H}_2) - 1]\right\}
\end{aligned}$$

Introducing

$$\chi = H_2 \left(\frac{\sigma}{2\nu}\right)^{1/2} \tag{4.26}$$

the normalized mud layer thickness, where $(2\nu/\sigma)^{1/2}$ is the thickness of the laminar wave-induced (mud) boundary layer (Jiang & Mehta, 1991), Equations 4.24 and 4.26 can therefore be further written as:

$$\begin{aligned}
\varepsilon_{D1} &= \frac{E_0}{1-r} \sigma F_r^2 \tilde{H}_2^2 \chi^{-2} \left(\frac{\bar{k}}{F_r}\right)^4 \left\{1 - R\left(\frac{\bar{k}}{F_r}\right)^2\right\}^2 \\
&\left\{\frac{3}{2}\tilde{H}_2 - \frac{1}{2}\tilde{H}_2 \tanh^2(\sqrt{-2i}\chi) + \frac{2\tilde{H}_2 \tanh(\sqrt{-2i}\chi)}{\sqrt{-2i}\chi} [\cosh(\sqrt{-2i}\chi) - 1] \right. \\
&\quad \left. - \frac{\tilde{H}_2 \tanh(\sqrt{-2i}\chi)}{2\sqrt{-2i}\chi} [\cosh(2\sqrt{-2i}\chi) - 1] - \frac{2\tilde{H}_2}{\sqrt{-2i}\chi} \sinh(\sqrt{-2i}\chi) \right. \\
&\quad \left. + \tilde{H}_2 \frac{1 + \tanh^2(\sqrt{-2i}\chi)}{4\sqrt{-2i}\chi} \sinh(2\sqrt{-2i}\chi)\right\} \tag{4.27}
\end{aligned}$$

and

$$\varepsilon_{D2} = \frac{E_0\sigma}{2} \frac{(1-i)^2}{1-r} \left(\frac{\bar{k}}{F_r}\right)^2 \left\{1 - r\left(\frac{\bar{k}}{F_r}\right)^2\right\}^2$$

$$\left\{ \frac{\tilde{H}_2}{2} [\tanh^2(\sqrt{-2i\chi}) - 1] + \tilde{H}_2 \frac{1 + \tanh^2(\sqrt{-2i\chi})}{4\sqrt{-2i\chi}} \sinh(2\sqrt{-2i\chi}) - \tilde{H}_2 \frac{\tanh(\sqrt{-2i\chi})}{2\sqrt{-2i\chi}} [\cosh(2\sqrt{-2i\chi}) - 1] \right\} \quad (4.28)$$

where $E_0 = 0.5\rho_1ga_0^2$ is the initial energy (at wave gauge #1). For any set of conditions in the flume, Equations 4.17, 4.27 and 4.28 can be used to calculate ε_D .

As an alternative to the above approach, the same dissipation rate can also be obtained via the following procedure:

$$\varepsilon_D = -\frac{dE}{dt} \quad (4.29)$$

The wave energy, E , is obtained from

$$E = \frac{1}{2}\rho_1ga_x^2 \quad (4.30)$$

where

$$a_x = a_0 \exp(-k_{iexp}x) \quad (4.31)$$

is the surface wave amplitude at any x , and

$$x = Ct \quad (4.32)$$

and (Jiang & Mehta, 1991)

$$C = C_0 \frac{F_r}{\tilde{k}_r} \quad (4.33)$$

with $C_0 = \sqrt{gH_1}$ being the wave celerity in shallow water over the rigid bottom and \tilde{k}_r being the normalized wave number from Equation 4.9. Therefore, Equation 4.29 can be further written as:

$$\varepsilon_D = \frac{\sqrt{gH_1}F_r}{\tilde{k}_r} \rho_1ga_x^2 k_{iexp} \quad (4.34)$$

Where g is the acceleration due to gravity; H_1 is the water column thickness, ρ_1 is water density and k_i is the surface wave attenuation (decay) coefficient over mud bed obtained from the fluidization experiment. This approach, which was especially suitable for analyzing the data obtained in this study, was used for calculation of the energy dissipation rate in Chapter 6.

CHAPTER 5 MUD BED FLUIDIZATION EXPERIMENTS

5.1 Test Conditions

Originally, three composite sediments (AK, BK, and AB) were selected as muds for the fluidization experiment, based on the rheological data presented in Chapter 3. However, time limitations permitted testing of only one composite, i.e., AK. This mud was mixed with the help of a compressed air jet in a 1.2m diameter and 1.4m high aluminum tank with a protective cover lid for two days before placement into the flume. The selected initial mud density was approximately 1.2 g l^{-1} .

In all the tests, water level in the flume was maintained at 35 cm, and wave period close to 1 sec. The only change in the experimental conditions was with the respect to the wave height. In different tests, the bed was subjected to wave heights ranging from 2 cm to 8 cm for selected durations. In addition to the wave height, total and pore water pressures, bed density profile (vertical), visual bed elevation, and water temperature were also recorded during the tests.

The flume setup is shown in elevation view in Figure 5.1. Eleven sets of tests were conducted. Except for test #1 in which the wave height was increased in steps without interruption, in all the other tests the wave height was kept constant at the wave maker throughout the fluidization process. Depending on the wave conditions, tests were run continuously for 6 hours to over one day. In tests #1 through #7 pressures were recorded but had to be discarded for want of accuracy due to a significant mean drift (see Section 3.3.3, Chapter 3) that was recorded by most pressure gauges. From test #8 onwards, the pressure measuring system was turned on at least at least 6 hrs before data collections, in order to minimize the drift problem. Table 5.1 summarizes the test conditions, including the

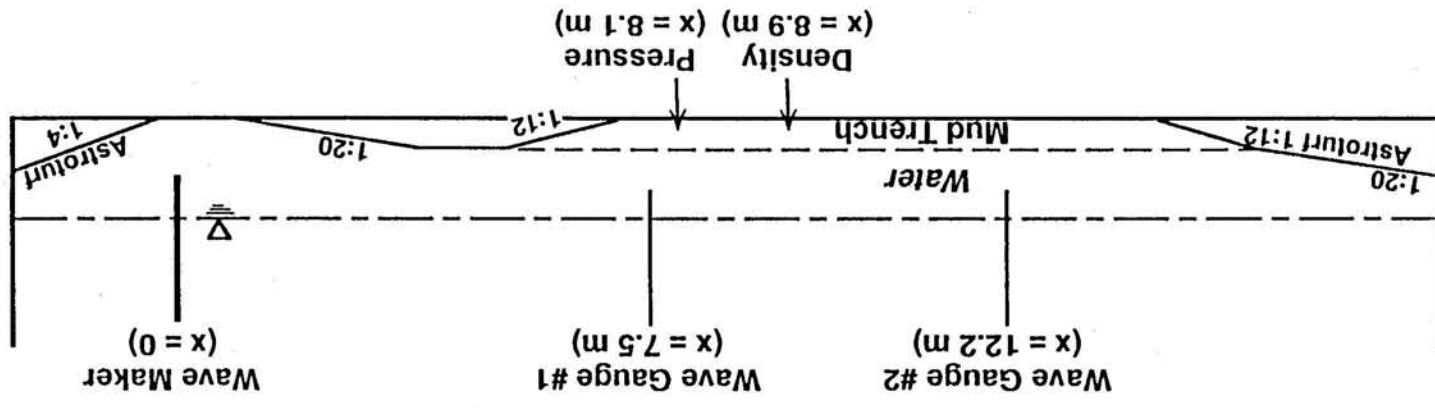


Figure 5.1: Sketch of flume profile in the fluidization experiment

Table 5.1: Summary of test conditions

Test No.	Consolidation time (hrs)	Average initial bed thickness(cm)	Design wave height (cm)	Frequency (Hz)	Duration (min)	Temp. °C
1	20	15.6	2	1.06	130	19
		15.3	4	1.06	30	19
		15.2	5	1.06	50	19
		14.5	7.7	1.06	45	19
2	15	13.9	2	1.06	135	20
3	15	13.7	3	1.06	290	20
4	160	18.3	4	1.06	2970	17
5	140	17.0	6	1.04	770	16
6	160	17.0	7.5	1.04	350	15
7	150	17.6	5	1.06	380	17
8	240	17.5	4	1.06	460	19
9	65	16.6	5	1.06	450	20
10	85	16.4	8	1.06	385	21
11	90	16.4	3	1.06	1700	20

bed consolidation time, average initial bed thickness, design wave height (at the beginning of the mud trench), wave frequency, experimental duration, and mean water temperature. As observed, the water temperature remained fairly constant through the entire test series.

Note that sediment densities were measured within mud only, not in the water column. This is because during the experiments, entrainment of mud into the water column was comparatively small. For example, Maa (1986) using the same flume found that the maximum sediment concentration in the water column was on the order of 0.05 to 0.5g/l only.

5.2 Flume Data

The complete set of experimental data from test #9 is given as an example here.

5.2.1 Wave Time-series

Wave heights at different times from test #9 are given in Table 5.2, and examples of the wave time-series are shown in Figure 5.2, where time refers to the beginning of the test. It can be observed that the wave height decreased with respect to both time and traveling distance, which in general suggests that the rate of wave energy dissipation changed during the course of the bed fluidization process. This issue is discussed later in Section 6.2.3.

Table 5.2: Wave heights, Test #9

Time(mins)	$H_{\#1}$ (cm)	$H_{\#2}$ (cm)
4	5.0	3.4
8	5.2	3.0
11	5.1	2.8
14	5.1	2.5
18	5.2	2.4
24	5.2	2.1
28	5.1	2.0
36	5.1	1.9
43	5.1	1.9
50	5.1	1.9
59	5.1	1.8
71	5.0	1.8
80	5.0	1.7
90	4.9	1.8
102	4.9	1.6
115	4.9	1.6
135	4.8	1.7
150	4.8	1.6
165	4.7	1.5
180	4.7	1.6
195	4.7	1.7
210	4.7	1.7
230	4.6	1.6
250	4.6	1.6
265	4.6	1.6
285	4.6	1.7
300	4.5	1.7
320	4.5	1.5
340	4.5	1.6
360	4.4	1.6
380	4.4	1.6
400	4.4	1.6
420	4.3	1.5
450	4.3	1.5

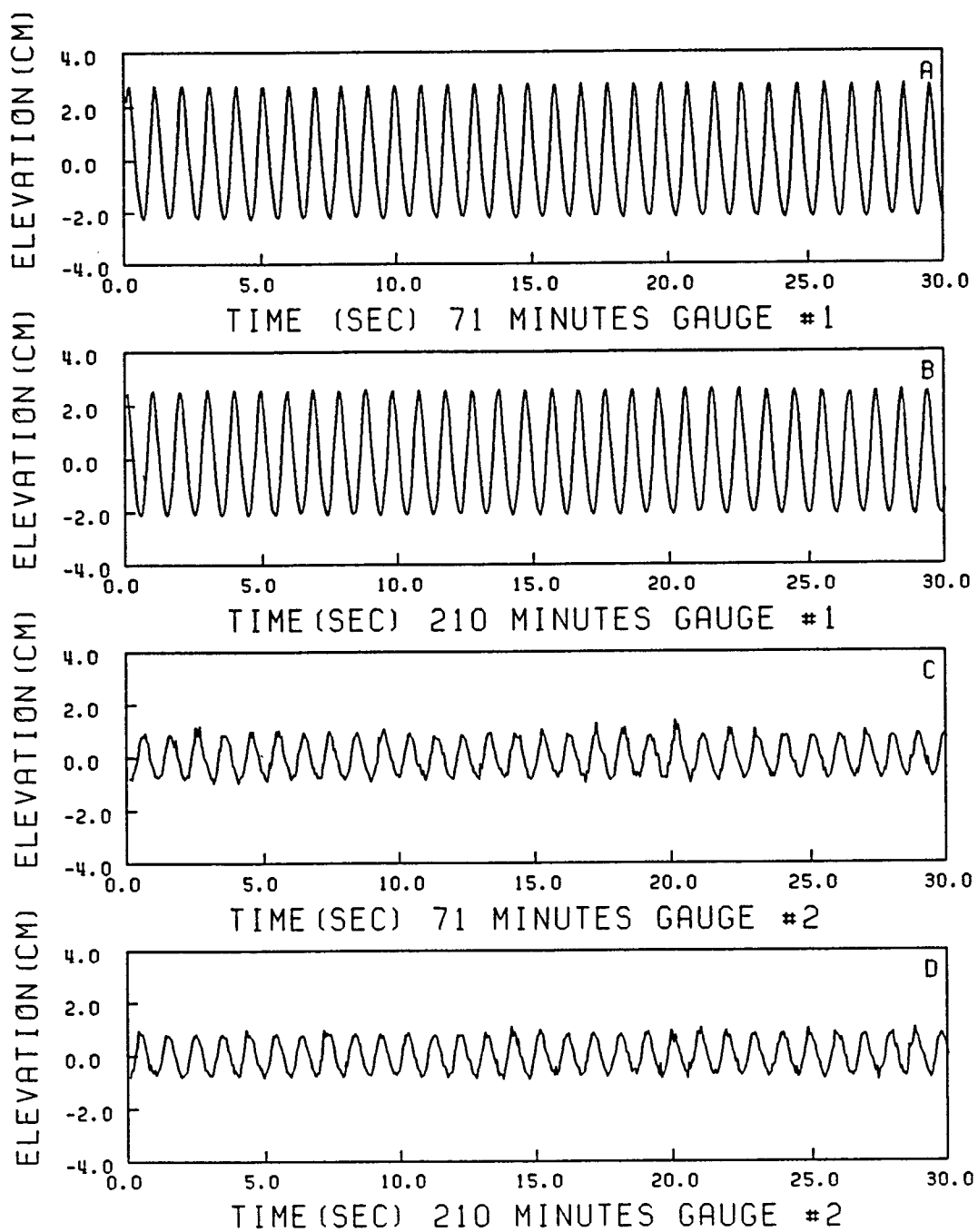


Figure 5.2: Wave time-series, Test #9

5.2.2 Wave Spectra

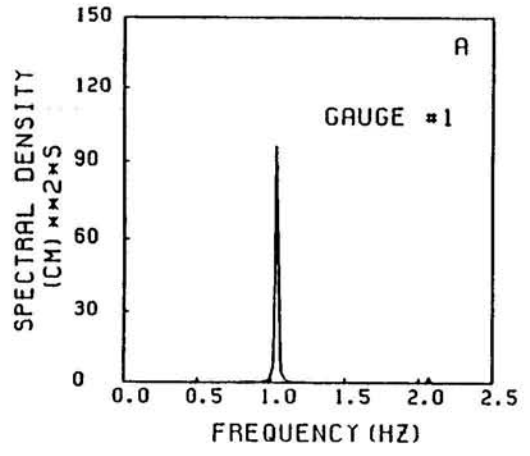
Wave spectra from test #9 are shown in Figure 5.3, where time represents test duration from the beginning. These spectra highlight the dissipation of wave energy during the test. At 71 mins the wave energy density decrease between the two gauges was $76 \text{ cm}^2\text{s}$, while at 210 mins and 360 mins the decrease was about $70 \text{ cm}^2\text{s}$, which is consistent with the trend in the wave energy dissipation rate, ϵ_D discussed in Section 6.2.3, Figure 6.6 (b).

5.2.3 Water/mud Interface

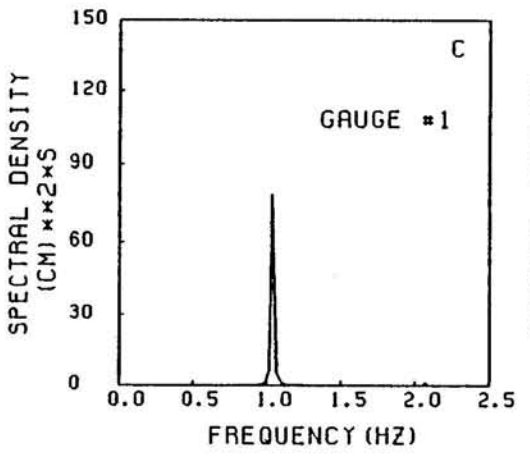
During wave action mud was initially observed to be transported downstream, due to the non-linear effect of the waves, especially due to net mass transport, which resulted in a slope (set-up) with interfacial elevation increasing in the downstream direction. Subsequently, under the opposing effects of mass transport and hydrostatic force due to the slope, the interfacial profile appeared to approach an equilibrium shape. Later on, however, when the upper part of the bed became fluidized, the top mud layer moved back again slightly. This phenomenon is seen from Figure 5.4 and the water/mud interface change in the density profiles presented in Section 5.2.4. After each test was conducted, recovery of the effective stress (described later in Section 6.3.1, Chapter 6), dewatering and gelling, all combined to cause the residual slope to become rapidly static. Even after some days no measurable change in the slope could be observed visually.

5.2.4 Density Measurement

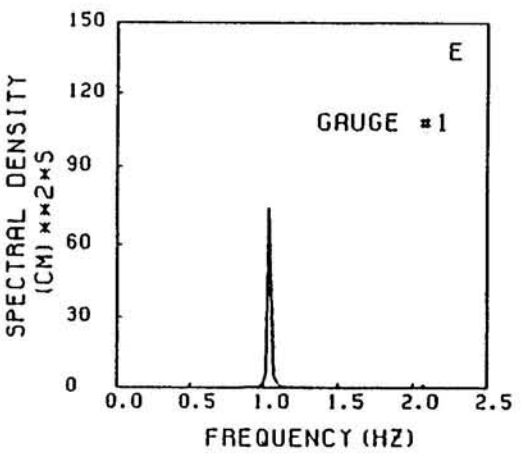
Examples of mud density profiles during test #9 are shown in Figure 5.5. These profiles indicate the generally stratified nature of the bed throughout the test. However, a change in bed density due to the fluidization could not be identified clearly from this test or others, an observation that is in agreement with that of Ross (1988). A part of the difficulty lies in the low accuracy of the measurements which were made at discrete elevations. However, since there was very little entrainment of mud into the water column, and since the bed did not dilute to any significant elevation during fluidization, a significant density change could not have been expected in these tests.



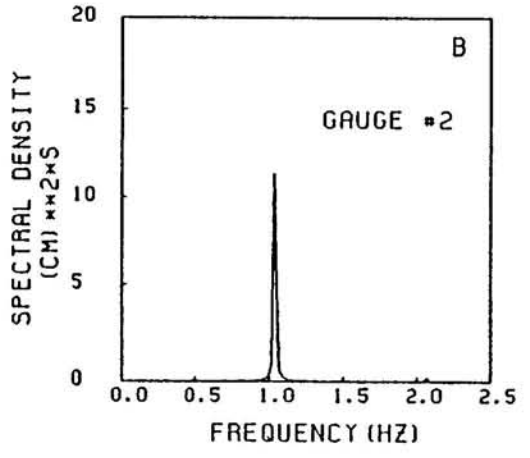
AVG. HT. = 5.0CM 71 MINUTES



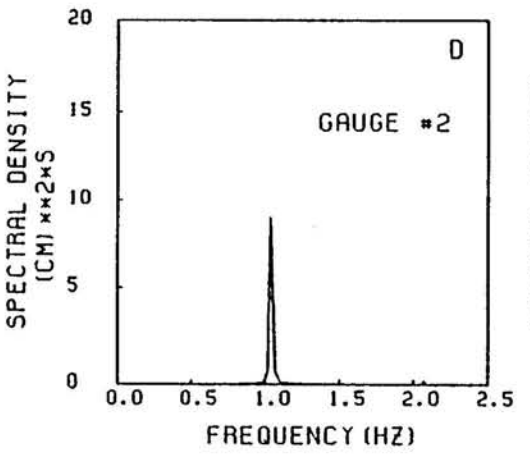
AVG. HT. = 4.7CM 210 MINUTES



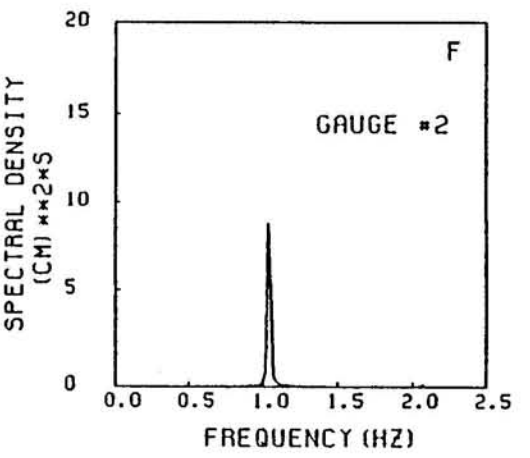
AVG. HT. = 4.4CM 360 MINUTES



AVG. HT. = 1.8CM 71 MINUTES



AVG. HT. = 1.7CM 210 MINUTES



AVG. HT. = 1.6CM 360 MINUTES

Figure 5.3: Wave spectra, Test #9

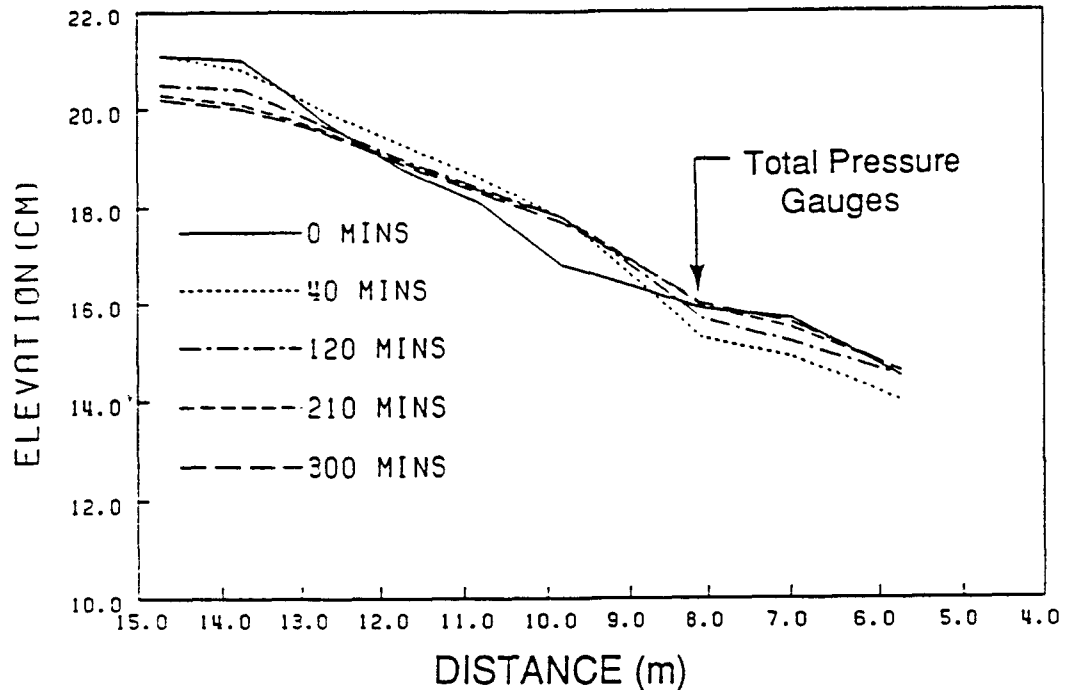


Figure 5.4: Time-variation of water-mud interface along the flume, Test #9

5.2.5 Total and Pore Water Pressures

Wave-averaged total and pore water pressures are shown in Figure 5.6. As indicated in Section 3.3.3, the total pressure gauge elevations did not match precisely with those of the pore pressure gauges, hence interpolation had to be used to calculate the value of the total pressure at exactly the same level at which the corresponding paired pore pressure gauge was located.

At the beginning, when wave action was started, the pore water pressure at a given elevation was equal to the corresponding hydrostatic pressure. Then under wave action an excess pore water pressure generally developed. In those cases in which the pore pressure curve intersected the total pressure curve, fluidization was considered to have occurred in

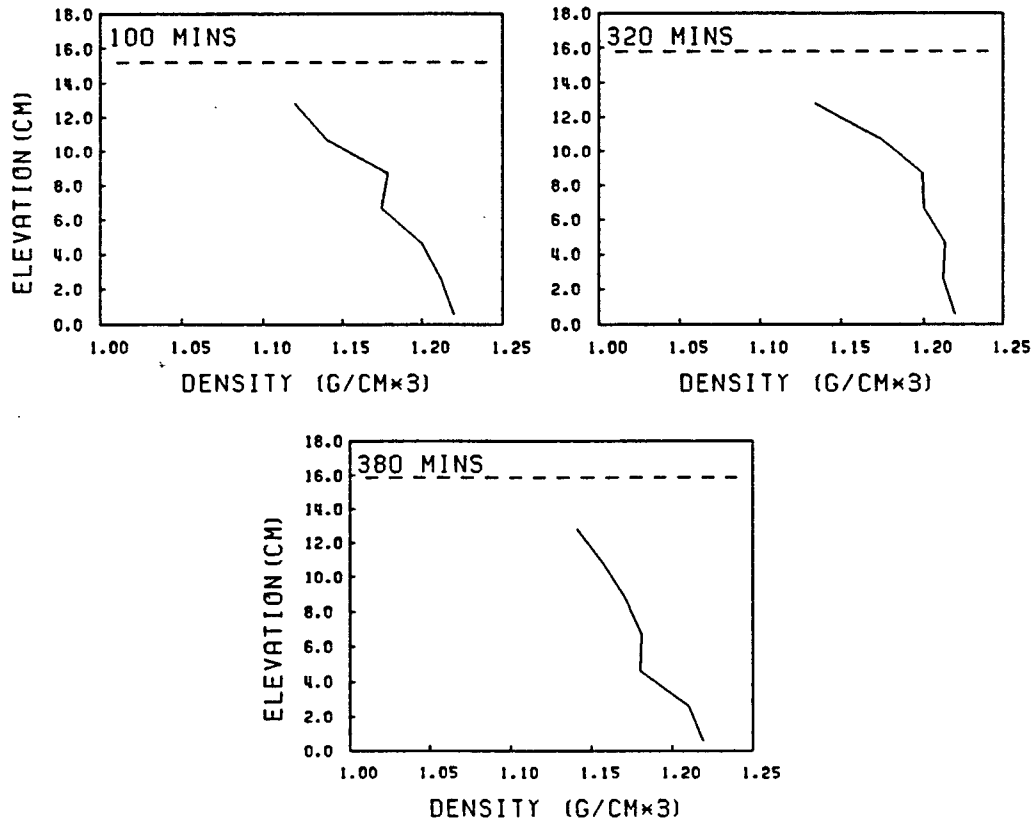


Figure 5.5: Examples of density profiles, Test #9. Dashed line indicates interfacial elevation

accordance with Figure 2.4. Note that the total pressure was also obtained independently from the density profiles, and these had to be used to "calibrate" for the total pressures in cases where the gauge data exhibited significant drift problems. Problems of instrument related drift noted in Section 3.3.3 (Chapter 3) are apparent in most cases in Figure 5.6. Drift generally caused both types of pressures to change over a time-scale that was much larger than the wave period, thus compromising the accuracy of determining the time at which fluidization occurred. The pore pressure data points at 14cm elevation dropped below the hydrostatic value which is unrealistic, and suggests a serious instrument problem. Note that with the exception of the gauge pair at 14cm elevation, all the gauges showed a response that suggested a drift that seem to cause the pressure to rise for the first 100-150 mins followed by a drop. This uniform behavior suggests that the drift problem may have been, at least in part, associated with the data acquisition system excluding the gauges themselves.

At this point it is worth considering the range of variation in total pressure that would have resulted from a change in the interfacial elevation during the course of the test. Referring to the time-variation of water-mud interface in Figure 5.4, at the pressure gauge site the maximum change of the mud surface elevation during test # 9 was about 5mm, which corresponded to 10 Pa pressure change, which was less than the accuracy of the pressure gauge (68Pa). On the other hand, the pressure measurement, for example at the 5.1cm elevation, indicated a difference of 90 pa. This difference was therefore attributed primarily to the drift problem.

5.2.6 Bottom Pressure Gauge Data, Test #9

Figure 5.7 shows the total pressure at the bottom of the flume during test #9. This plot shows that at first the total pressure decreased (from 3.73 kPa to 3.7 kPa, i.e., 30 Pa) for about 40 minutes, then increased slightly. This change suggests mud advection movement due to wave action. When waves just began, mud moved in the downstream direction because of the non-linear effects of waves, thus causing a set-up in the flume as noted in

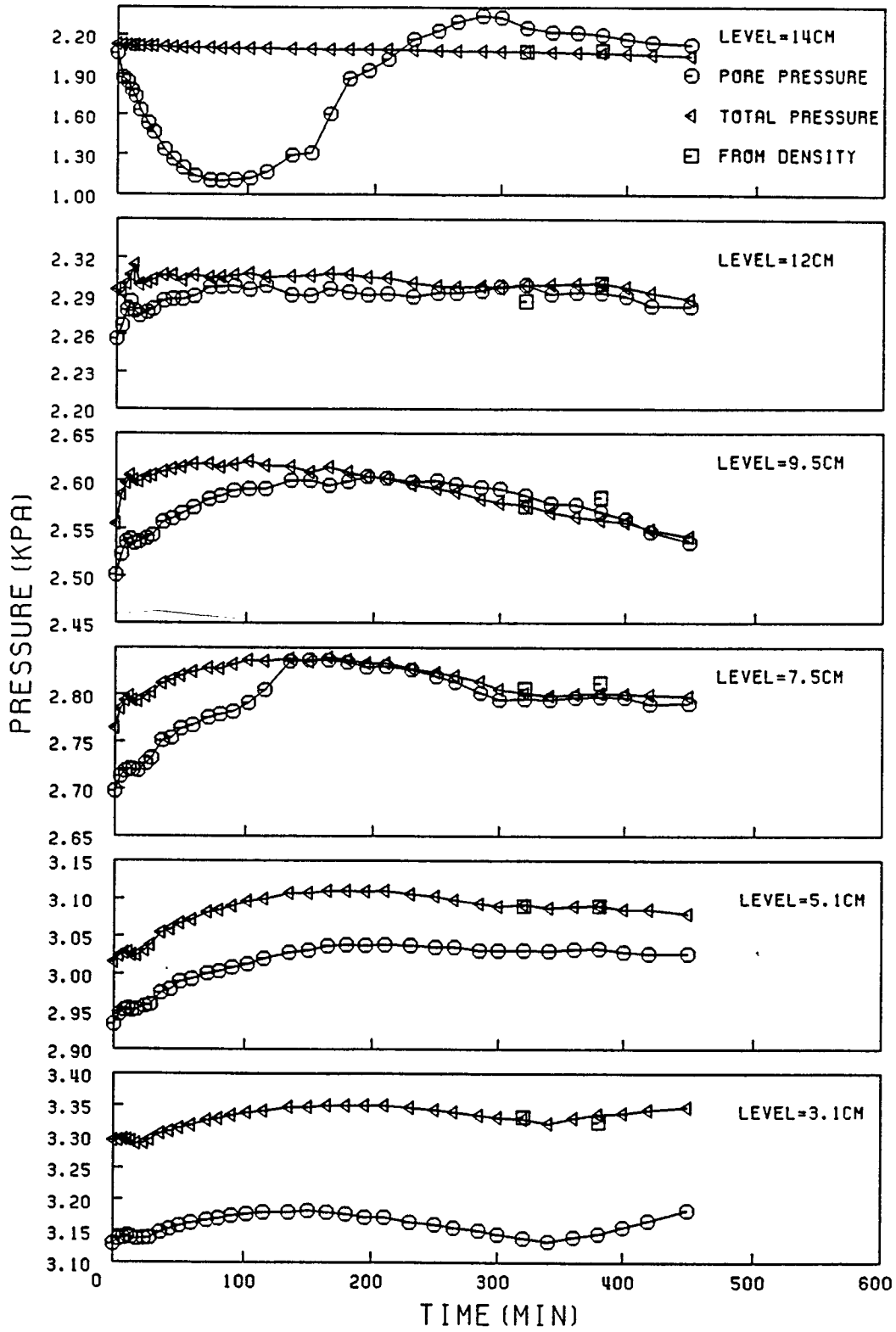


Figure 5.6: Wave-averaged total and pore water pressures, Test #9

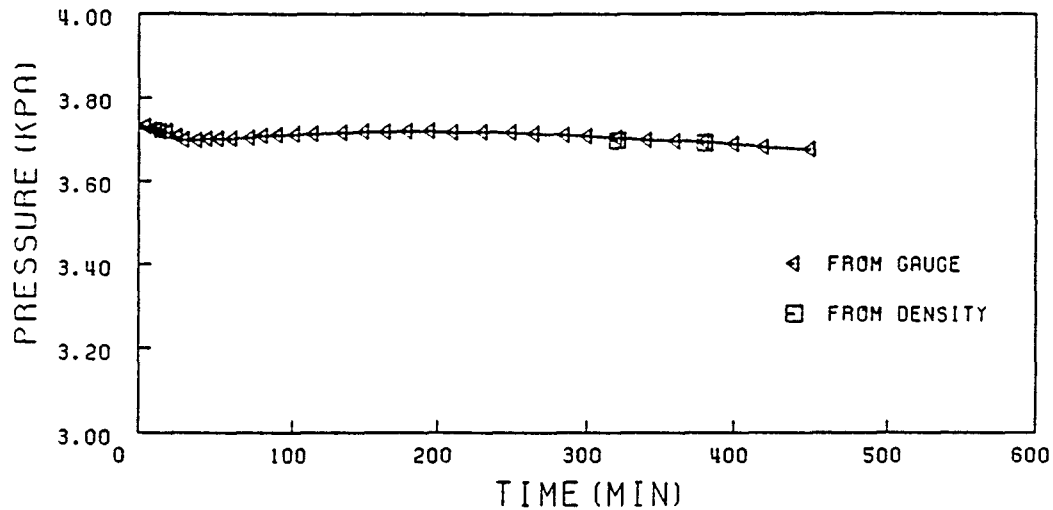


Figure 5.7: Total pressure at the bottom of the flume, Test #9

Section 5.2.3. When the top of the bed was fluidized, which thus became a suspension, the mud moved back again to level out the bed surface.

This result from the total pressure measurement was very consistent in the first 200 mins, with the phenomenon shown in Figure 5.4 in Section 5.2.3. which shows that the pressure data dropped in the first 40 mins, then started to increase slightly. However, after 200 mins, it dropped again.

5.2.7 Rms Pressure Amplitudes, Test #9

Root-mean square (rms) amplitude pressure is obtained from

$$P_{rms} = \sqrt{\frac{1}{N} \sum_{i=1}^N (P_i - \bar{P})^2} \quad (5.1)$$

where P_i is the instantaneous pressure, \bar{P} is the time-mean pressure, and N is the number of data points. Rms amplitudes of pore and total pressure data are shown in Figures 5.8 and 5.9. For both the total and pore pressures there was a trend of increasing amplitudes initially in the first approximately 30 mins, especially at the top three levels. This increase was an indication of the wave-induced movement been transmitted relatively rapidly into the bed. Later on as the bed began to fluidize, which dissipated more wave energy, the pressure

amplitudes decreased accordingly. The largest decrease in pressure amplitude occurred at about the same time when the wave energy dissipation rate was highest (see Figure 6.16). The decreasing of the rms amplitudes can reflect increasing the wave energy dissipation during the bed fluidization process. Such a decrease was more rapid initially, as further noted in Section 6.2.3.

Combining the data in Figure 5.8 and 5.9 with those in Table 5.2 it can be concluded that as the wave height decreased with time, the rms amplitudes of pore and total pressure also decreased with time, especially for the top three (elevations of 14cm, 12cm, and 9.5cm) pressure data. Apparently, the pressure amplitudes decreased only slightly after fluidization occurred (the elevations and times when fluidization occurred are given in Table 6.6, Section 3.2 of Chapter 6). Finally, it can be concluded that the amplitudes in the lower levels of mud layer had smaller values than at higher elevations, presumably because the wave amplitude decreased as the dynamic pressure was transmitted and dissipated downwards into the bed.

5.2.8 Pressure Recovery after End of Test

In test #9, pressure data were obtained after wave action ceased. The corresponding effective stresses are calculated and discussed in Section 6.3.1.

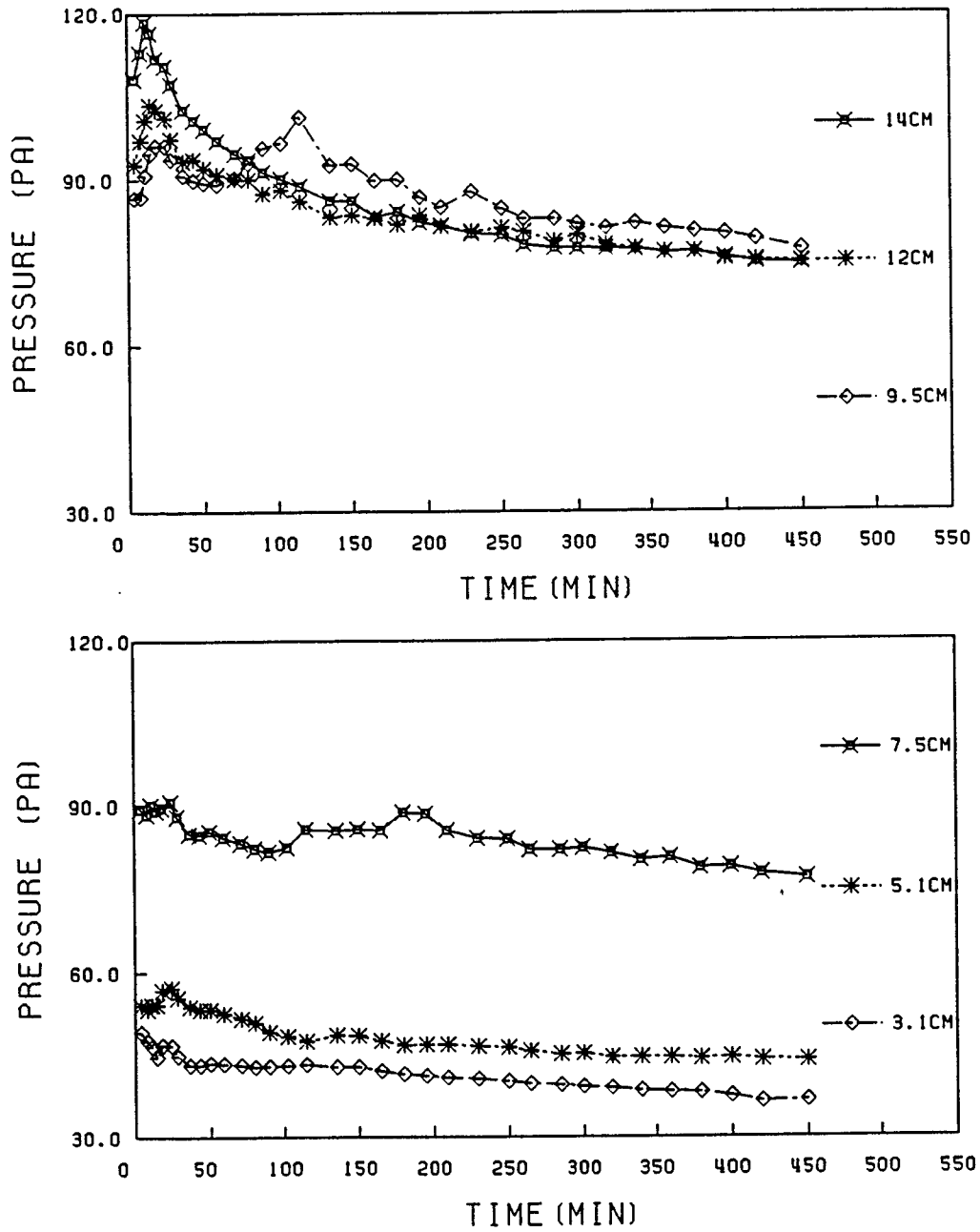


Figure 5.8: Root-mean square pore water pressure amplitudes, Test #9

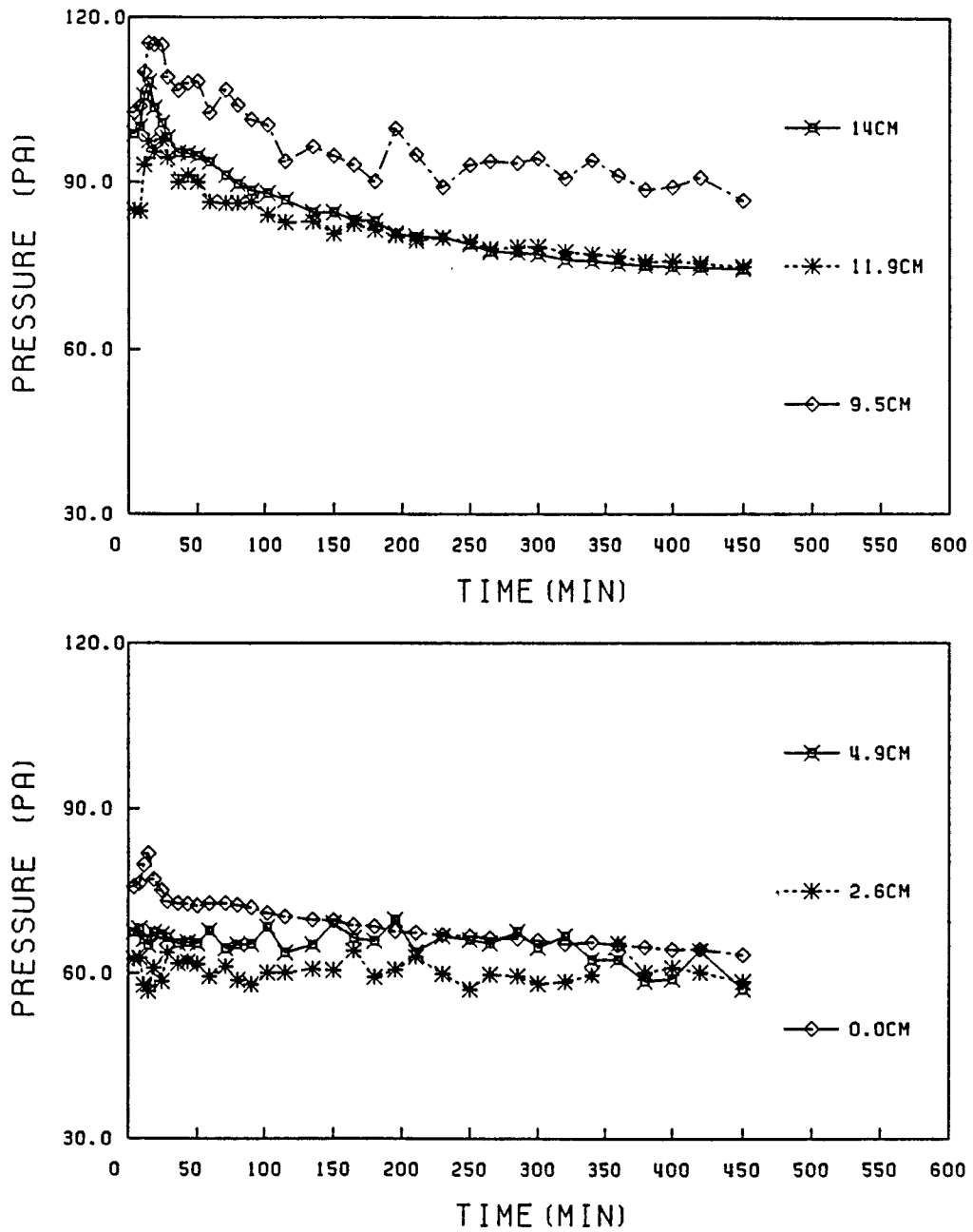


Figure 5.9: Root-mean square total pressure amplitudes, Test #9

CHAPTER 6 EXPERIMENTAL DATA ANALYSIS

6.1 Introduction

In this chapter, results are presented, based on the wave-mud interaction (introduced in Chapter 4), which were applied to calculate the effective sheared thickness, d , as a possible representative of the fluidized mud layer thickness, as well as the rate of energy dissipation, ε_D (also from Chapter 4). The pressure data are then analysed to determine the fluidized mud thickness, d_f , and the rate of fluidization. The two types of thicknesses, d and d_f , are then compared, and the relationship between the rate of fluidization and the rate of wave energy dissipation, ε_D , is examined.

6.2 Wave-Mud Interaction Model Results

6.2.1 Wave Regime: Test Versus Model Conditions

As noted in Chapter 4, the wave-mud interaction model is based on the shallow water assumption, i.e., $H_1/L < 0.05$, where L is the wave length, which was obtained from the linear wave dispersion equation (assuming rigid bed condition):

$$L = \frac{g}{2\pi} T^2 \tanh \frac{2\pi H_1}{L} \quad (6.1)$$

The range $0.05 < H_1/L < 0.5$ is the transition condition from the shallow water to deep water. Table 6.1 presents the values of H_1/L for the present experiments. As observed the test condition was not really shallow water according to this classification. There are two different types of effects on the model-based results due to shallow water assumption. Firstly, in the shallow water model the particle horizontal velocity is assumed to be uniform in the z direction in the water column. When waves are not in the shallow water regime this velocity decreases downwards from the water surface, so that near the bottom of the water column

Table 6.1: Parameters for determining the water wave condition

Test #	H_1	L	H_1/L
	(cm)	(m)	
1	19.4	1.11	0.17
2	21.1	1.13	0.19
3	21.3	1.14	0.19
4	16.7	1.05	0.16
5	18.0	1.11	0.16
6	18.0	1.11	0.16
7	17.4	1.07	0.16
8	17.5	1.07	0.16
9	18.4	1.09	0.17
10	18.6	1.09	0.17
11	18.6	1.09	0.17

the particle movement is smaller than that at the surface. Thus the velocity at the bottom of the water column (at the mud surface) was overpredicted by the model. Consequently the model also overpredicts the degree of the bed fluidization in this sense. On the other hand, however, the shallow water model assumes the particle vertical acceleration to be equal to zero, which was not quite the case. The vertical movement of the water particle at the bottom of the water column would contribute to the wave energy transmission down to the mud layer, thus enhancing bed fluidization. Therefore from this point of view the model underestimates the degree of bed fluidization. These two factors therefore have opposing effects on fluidization, hence the overall influence of the shallow water assumption in reality depends on which of the two factors is dominant. The limited scope and data in this study prevented a quantitative evaluation of these two factors on the observed fluidization process.

6.2.2 Effective Sheared Mud Thickness

As a possible representative of the fluidized mud layer thickness, the effective sheared thickness of the bed, d , within which (fluid) mud was sheared by the wave, was calculated according to the diagram presented in Figure 4.2. Results are shown in Figures 6.1, 6.2, and 6.3, where the marker points represent experimental data, and the solid lines are obtained from least squares polynomial fit using these data. The procedure for calculating

d , notes in Chapter 4, is repeated here for convenience:

1. Select an initial value of the shear rate, $\dot{\gamma}_0$, to calculate viscosity, μ , by the power-law equation for viscosity, i.e., by Equation 4.13 ($\mu = \mu_\infty + c\dot{\gamma}_0$).
2. Use the viscosity thus obtained to calculate k from Equation 4.9. The imaginary part of k , i.e., k_i , is the wave damping coefficient.
3. With the recorded wave heights at the two gauges, the measured wave damping coefficient, k_{iexp} , can be obtained from $H_{\#2} = H_{\#1} \exp(-k_{iexp} \Delta l)$, via Equation 4.11, where $H_{\#1}$ is the wave height at gauge #1 and $H_{\#2}$ the height at gauge #2.
4. When k_i obtained from step 2 “matches” k_{iexp} obtained from step 3 by iterating for $\dot{\gamma}$, i.e., $|(k_{iEq.4.11} - k_{iEq.4.9}) < 0.01|$, the selected $\dot{\gamma}$ is assumed to be right, or a new $\dot{\gamma}$ is chosen for Equation 4.13 and the above procedure repeated until k_i and k_{iexp} match.

One example of the calculation for test #9 is given here. The input parameters are: $\mu_\infty = 4.44 Pa.s$, $c = 0.76$, $n = -1.083$, water density, $\rho_1 = 1g/cm^3$, mud density, $\rho_2 = 1.17g/cm^3$ (representative depth-mean value), distance between two gauges $\Delta l = 5.3m$, average bed thickness within the test section, $H_2 = 16.7cm$, water column depth, $H_1 = 35 - H_2 = 18.3cm$, $\sigma = 2\pi/T = 6.28Hz$, $H_{\#1} = 5.0cm$ and $H_{\#2} = 1.8cm$. An iterated value of the shear rate $\dot{\gamma} = 0.01Hz$ was selected to be used in Equation 4.13 to obtain the dynamic viscosity $\mu = 611Pa.s$, which in turn was used in Equation 4.9 to calculate the wave dissipation coefficient k_i that agreed with the one from experimental data obtained from Equation 4.11. The wave-induced horizontal velocity in the mud layer (surface) was determined by Equation 4.12, which together with Equation 4.14 gave the effective sheared thickness $d = 6.6cm$.

Table 6.2 gives the input parameters for all the tests. The wave heights $H_{\#1}$ and $H_{\#2}$, and the test section-average mud thickness H_2 changed with time, i.e., they were not constant within each test. Therefore these parameters are not given in the table. Note

Table 6.2: Input parameters for calculating the effective sheared mud thickness

Test #	μ_{∞} (Pa.s)	c	n	ρ_2 (g/cm ³)	σ (rad/sec)
1	4.44	0.76	-1.083	1.19	6.28
2	4.44	0.76	-1.083	1.19	6.28
3	4.44	0.76	-1.083	1.19	6.28
4	4.44	0.76	-1.083	1.17	6.28
5	4.44	0.76	-1.083	1.17	6.28
6	4.44	0.76	-1.083	1.17	6.28
7	4.44	0.76	-1.083	1.17	6.28
8	4.44	0.76	-1.083	1.17	6.28
9	4.44	0.76	-1.083	1.18	6.28
10	4.44	0.76	-1.083	1.19	6.28
11	4.44	0.54	-0.68	1.18	6.28

that in test #11 the parameters c and n had to be changed, Since under small waves bed deformation was limited to a small upper portion of the bed, and the bed density of that portion was much less than the depth-average density used otherwise, so that the viscosity of that layer was lower than that based on the depth-mean density. Based on this concept, c was reduced (from 0.76 to 0.54) and n (from -1.083 to -0.68) was increased. These reduced values corresponding a density $\rho_2 = 1.12g/cm^3$. The wave frequency used was selected throughout to be 1 Hz (6.28 rad/sec) in the model, which was not exactly equal to those given in Table 5.1, but was acceptably close.

It can be seen from Figures 6.1, 6.2 and 6.3 that, in general, the larger the wave height the thicker the effective sheared thickness, d , and that initially it generally increased relatively rapidly and eventually approached some constant value, d_s , under a given set of flume conditions. In general, values of d_s also increased with the wave height, and the results for the eleven tests are shown in Table 6.3.

6.2.3 Wave Energy Dissipation

Wave energy dissipation per unit of time, ε_D , was determined from Equation 4.34. Figures 6.4, 6.5 and 6.6 present ε_D as a function of time for all the tests. These figures show that typically ε_D was relatively small in the beginning, then increased gradually under

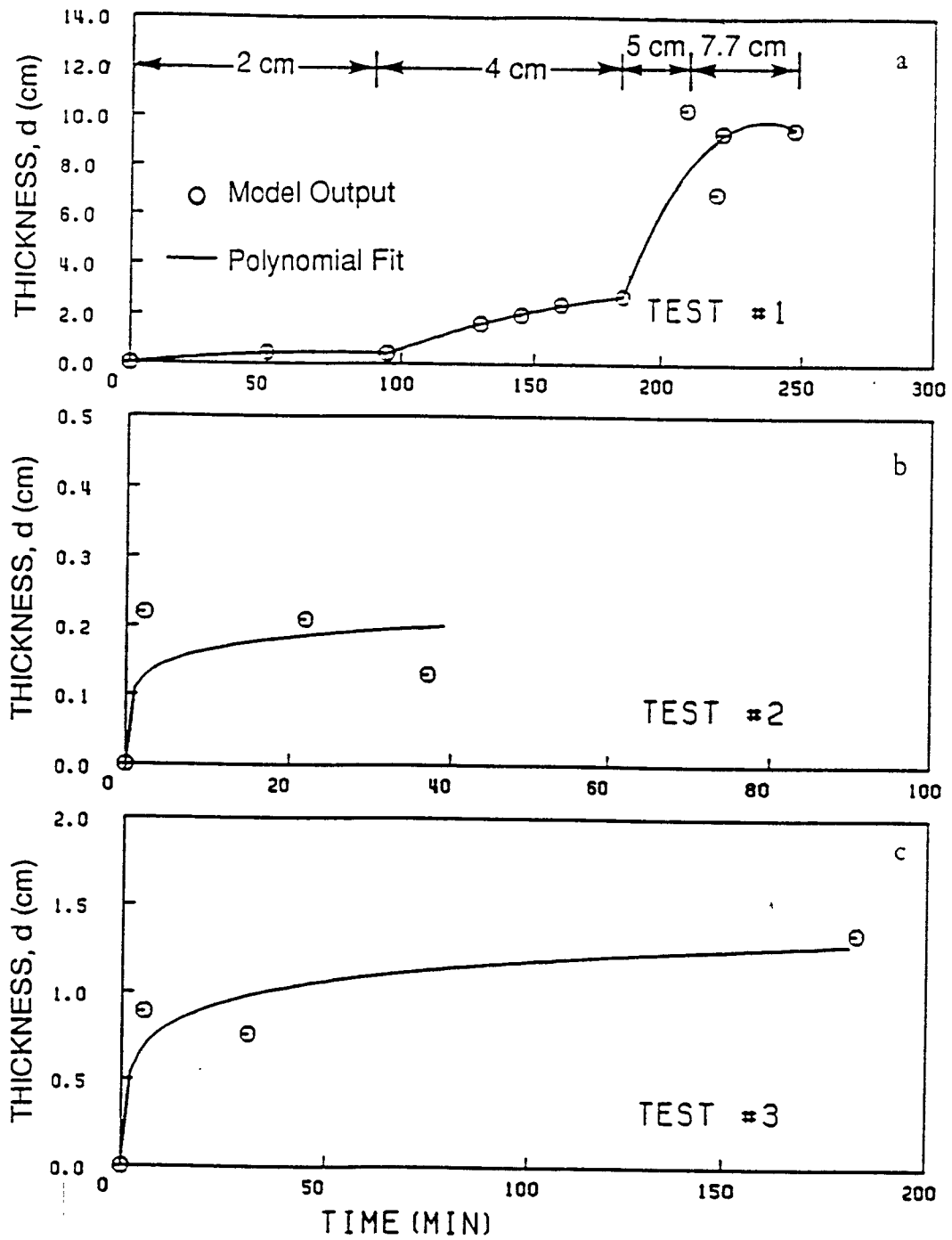


Figure 6.1: Effective sheared mud thickness, d , Tests #1 through #3

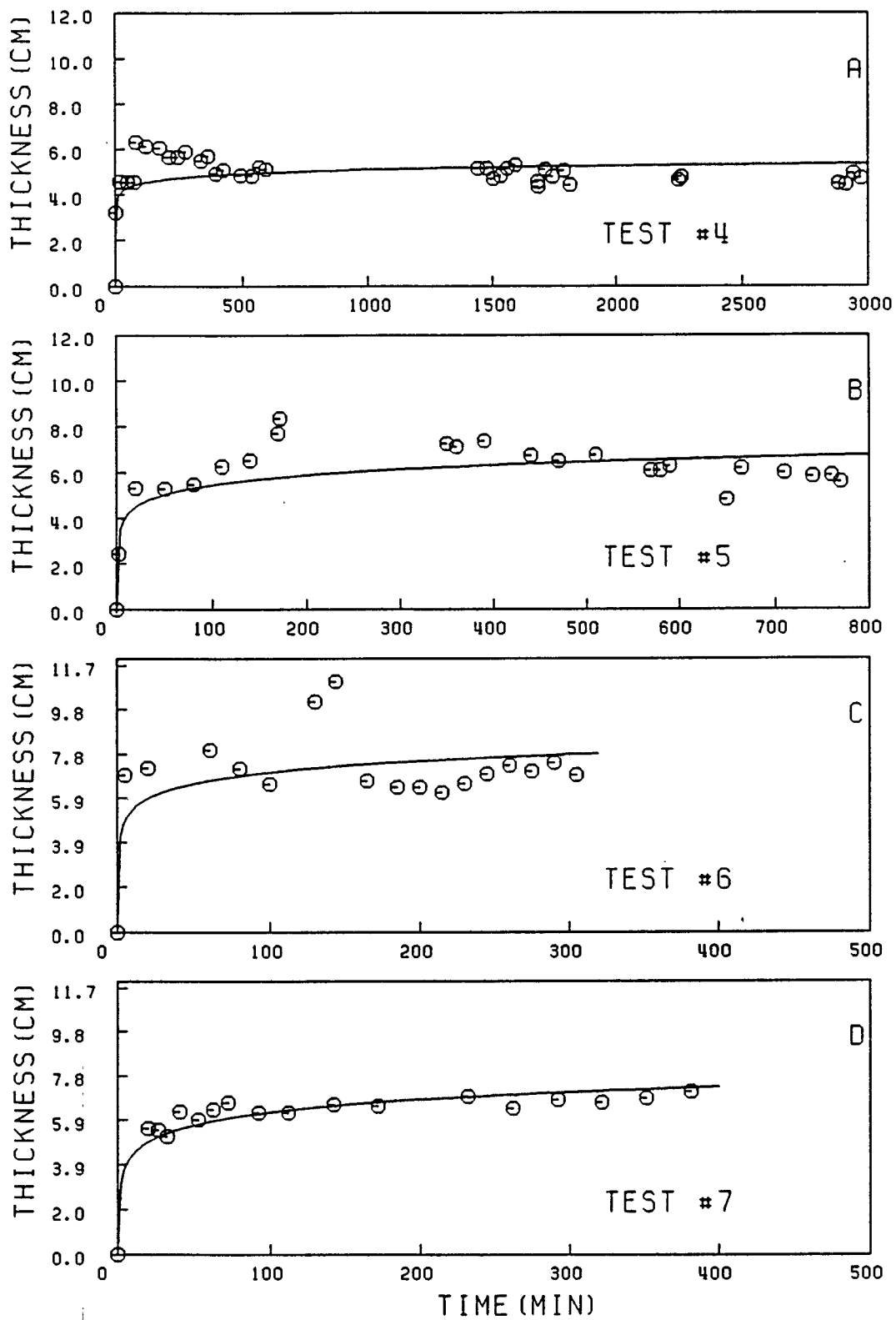


Figure 6.2: Effective sheared mud thickness, d , Tests #4 through #7

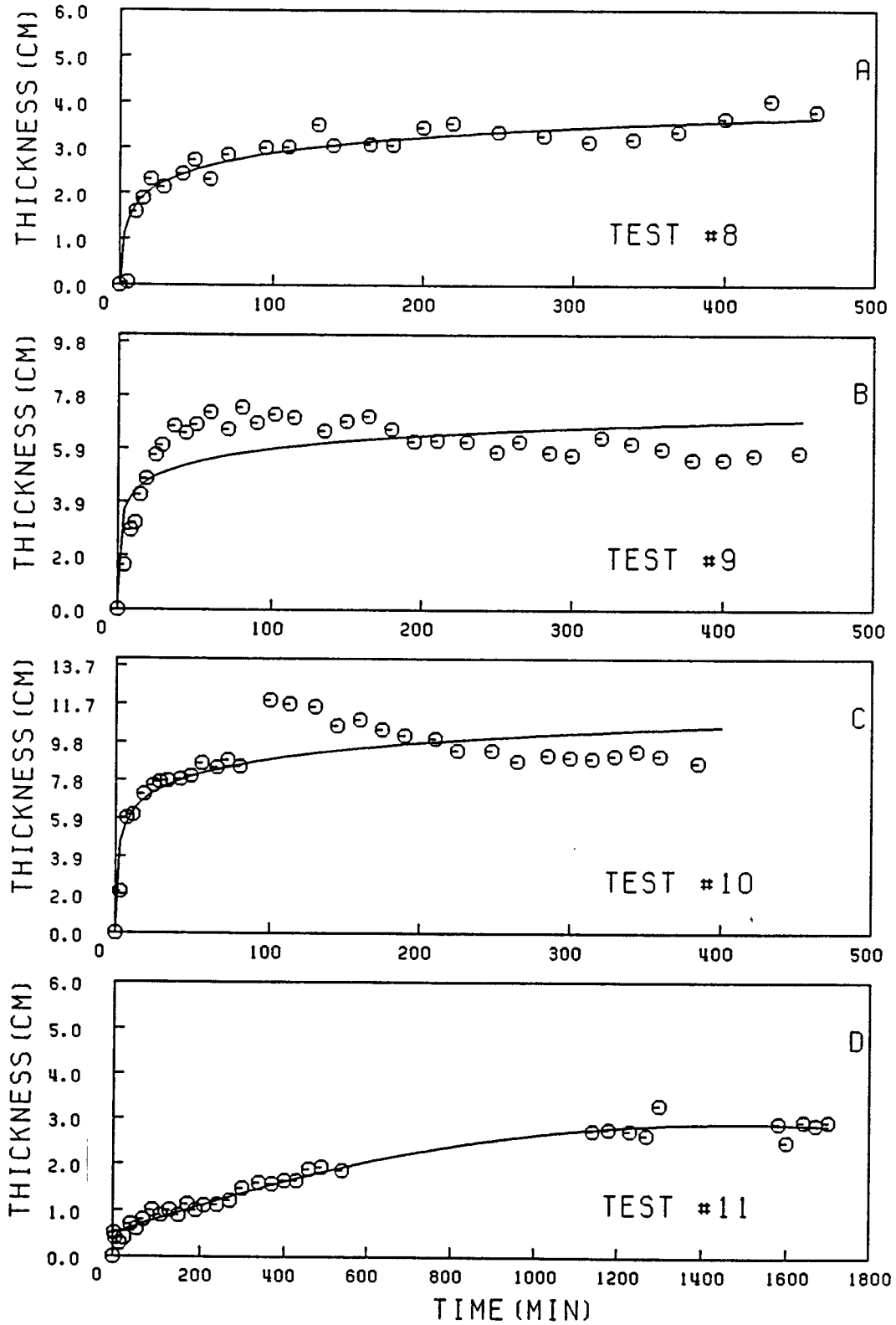


Figure 6.3: Effective sheared mud thickness, d , Tests #8 through #11

Table 6.3: Values of the (representative) constant effective sheared mud thickness, d_s , $\dot{\gamma}$ and μ

Test No.	d_s (cm)	$\dot{\gamma}$ s^{-1} or Hz	μ (Pa.s)
1	9.4	0.043	425
2	0.2	0.017	2634
3	0.7	0.035	680
4	4.9	0.032	728
5	6.6	0.032	770
6	7.8	0.034	662
7	6.8	0.034	670
8	3.6	0.032	750
9	6.1	0.036	630
10	9.2	0.037	575
11	2.8	0.036	600

the wave action to a maximum value, and decreased again to approach some constant value, ε_{D_s} . The respective values of ε_{D_s} for the tests are given in Table 6.4, although since in some tests ε_D did not quite reach the constant value ε_{D_s} , the final experimental value of ε_D has been reported instead. As seen from Equation 4.34, the magnitude of ε_D is controlled by two primary factors, the wave amplitude (squared), a_x^2 , and the wave decay coefficient, k_i , which have been plotted as functions of time for test #9 in Figure 6.7 for further discussion. At the beginning of wave action, the bed had greater rigidity, k_i was comparatively small (although much higher than the representative value $0.02 s^{-1}$, that can be derived from the flume characterization tests using a false rigid bottom described in Section 3.4), and although the wave amplitude was higher, the product of k_i and a_x^2 was still comparatively small. As the fluidization process went on, there was more fluid mud involved in the energy dissipation process, and k_i increased rapidly, which in turn increased ε_D eventhough a_x decreased. Thus more wave energy dissipation occurred when the fluidized mud thickness increased, but there was apparently a limit to it corresponding to a constant value, as the fluid mud thickness approached a constant value as well.

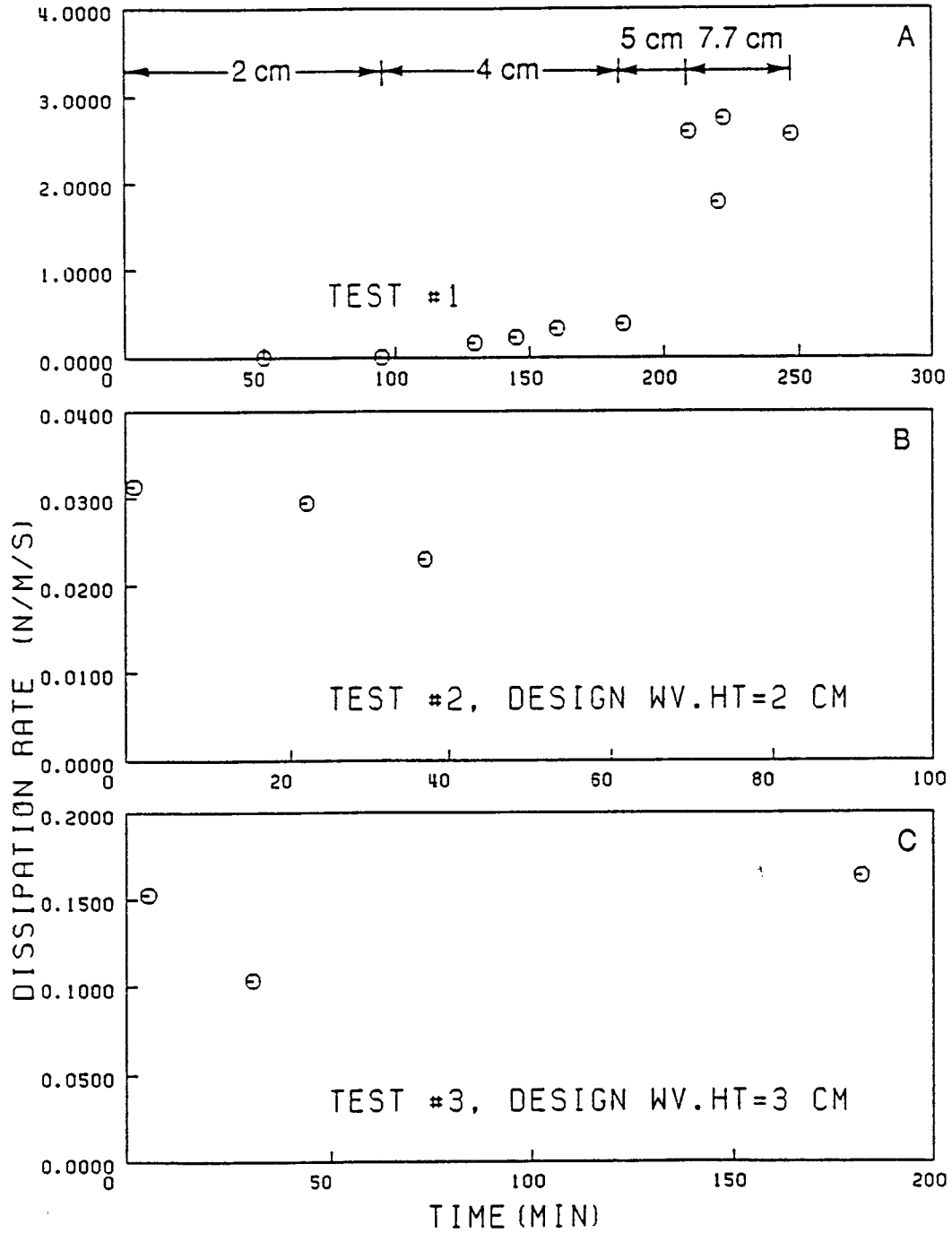


Figure 6.4: Wave dissipation rate, ϵ_D , versus time: Tests #1 through #3

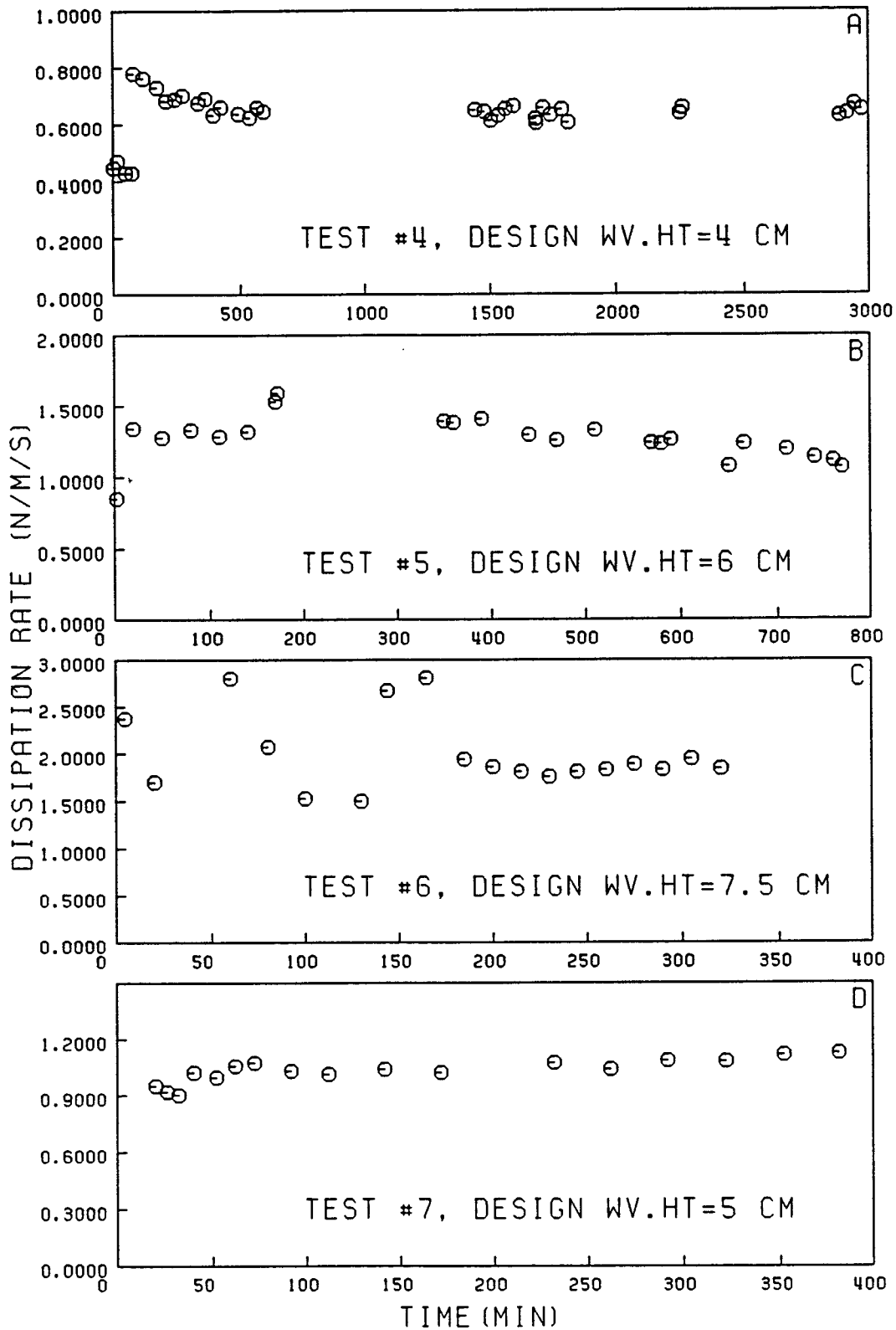


Figure 6.5: Wave dissipation rate, ϵ_D , versus time: Tests #4 through #7. Design wave heights are from Table 5.1

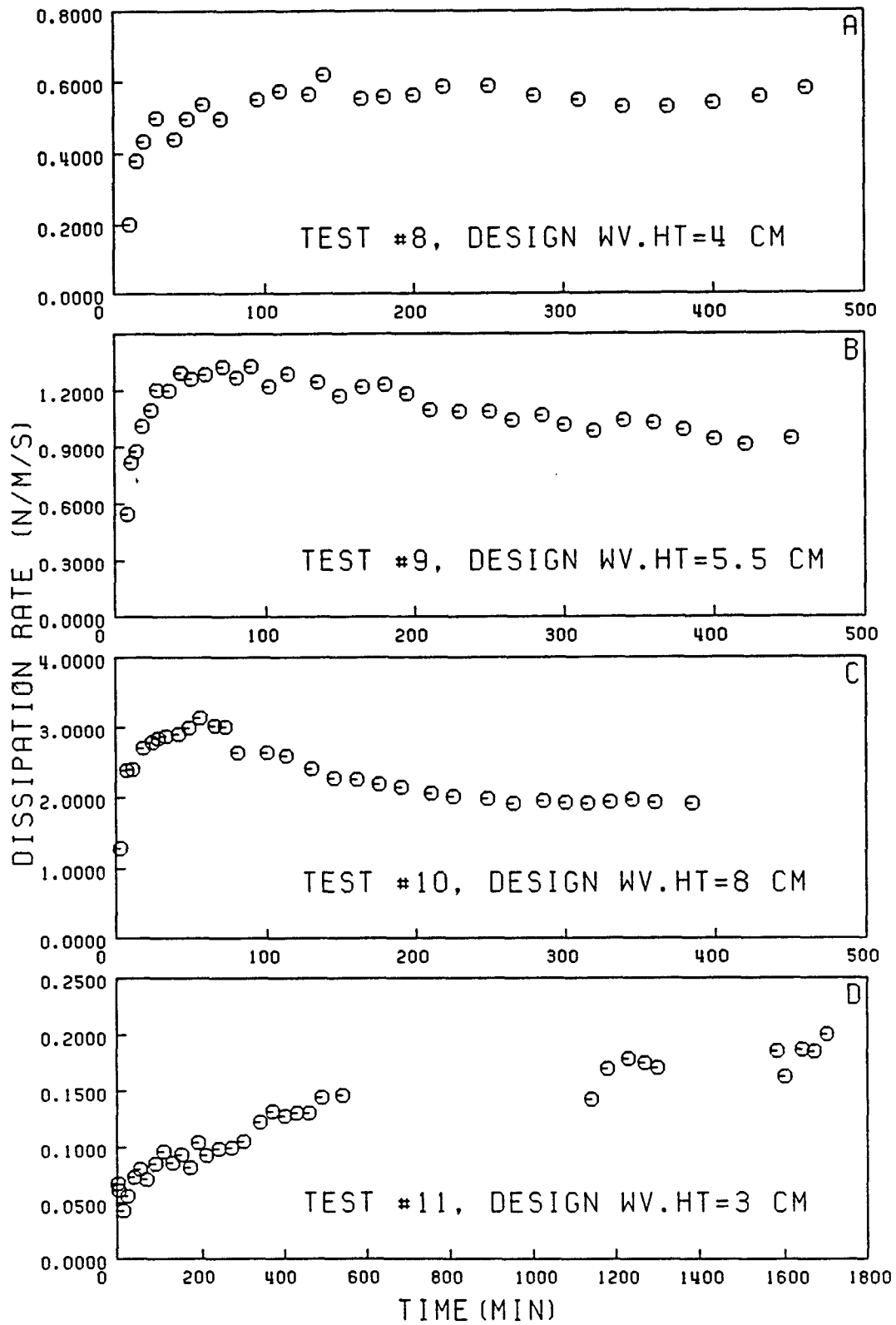


Figure 6.6: Wave dissipation rate, ϵ_D , versus time: Tests #8 through #11. Design wave heights are from Table 5.1

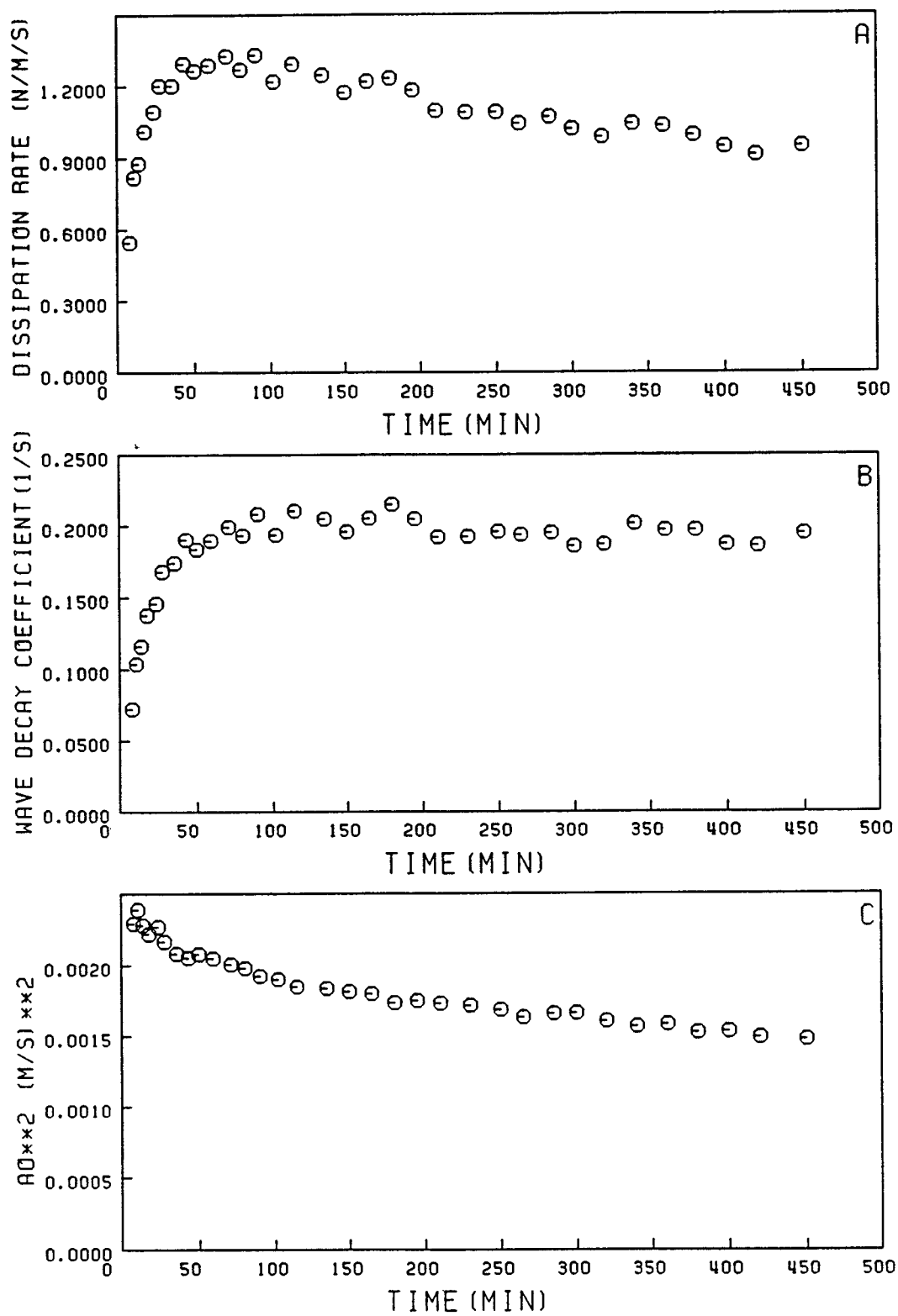


Figure 6.7: ε_D , k_i and a_x^2 versus time: Tests #9

Table 6.4: Representative values of the wave energy dissipation rate, ϵ_{D_s}

Test No.	1	2	3	4	5	6
$\epsilon_{D_s}(N/m/s)$	2.8	0.22	0.15	0.66	1.3	2
Test No.	7	8	9	10	11	
$\epsilon_{D_s}(N/m/s)$	1.1	0.57	1	2.1	0.18	

6.3 Flume Test Results

6.3.1 Effective Stress

The difference between the total and pore water pressures gives the effective stress, σ' (see Equation 2.5), whose time-variation shown in Figures 6.8, 6.9, 6.10 and 6.11 for test #8 through #11, respectively. These figures show that under wave loading the effective stress eventually decreased in all cases except at the 3.1cm level. Thus the upper part of the bed eventually lost its structured matrix, and was thus fluidized, when σ' became zero or nearly zero. For the 3.1cm level, in most cases the effective stress increased under wave action. A possible reason was that the soil particles in the bed were not very tightly packed initially. Under wave action, they were repacked more tightly by shaking and overburden near the rigid flume bottom. This effect can be corroborated from the density change at this level. For example in test #8, 130 mins after wave action the density at the 3.1cm level was $1.19 g/cm^3$, while at 380 mins the density increased to $1.20g/cm^3$.

In test #9, pressure data during the consolidation phase following cessation of wave action were also recorded, and the corresponding time-variation of σ' is shown in Figure 6.9. The results indicate that after waves stopped, the effective stress in the bed increased again, and the bed structure thus exhibited recovery. Table 6.5 gives the initial (time 0) values of σ' at each level and also those at the end of the test after recovery. As might be expected, the recovery was greater at lower elevations than higher, where the fluid state persisted to some extent.

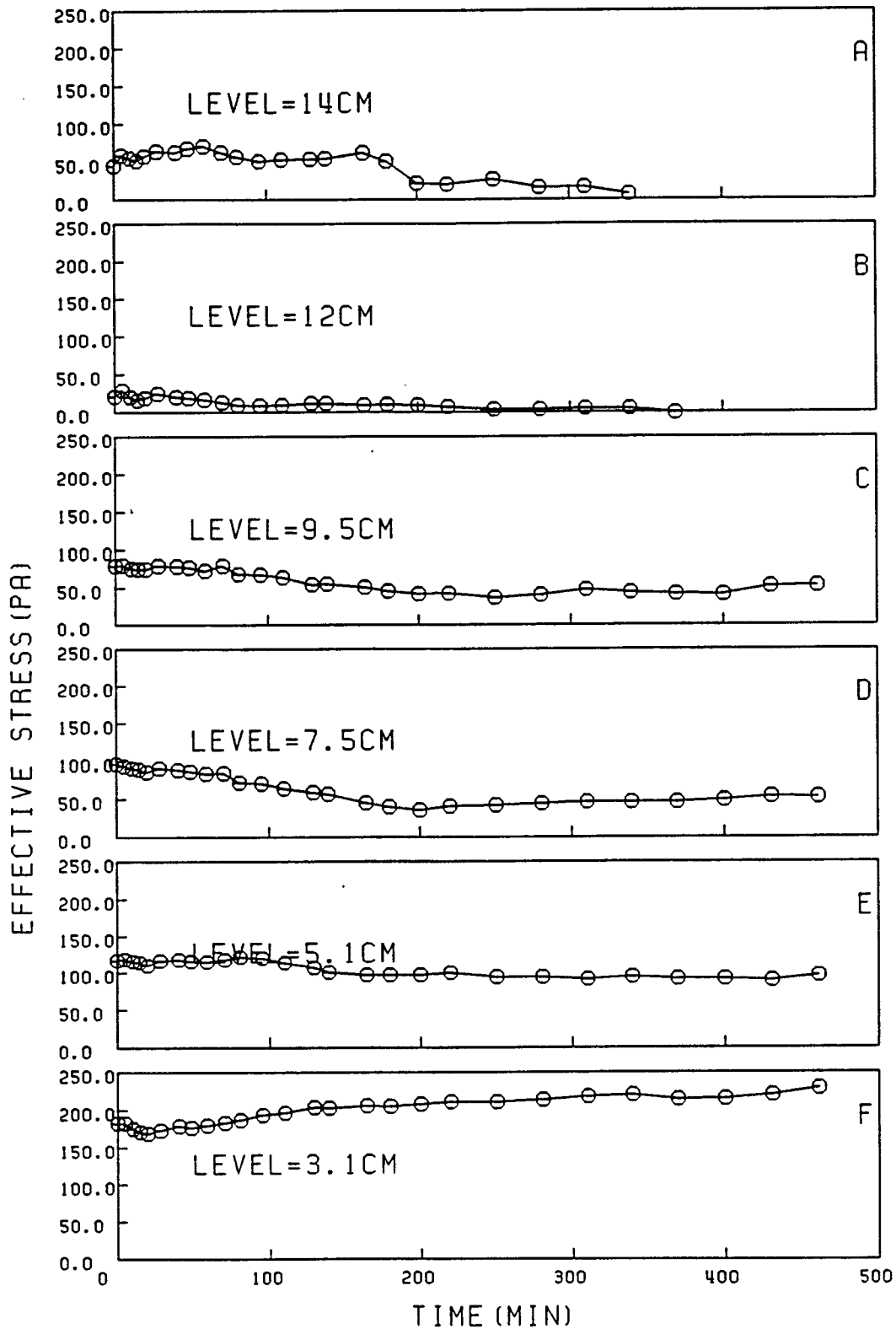


Figure 6.8: Effective stress, σ' , variations with time: Test #8

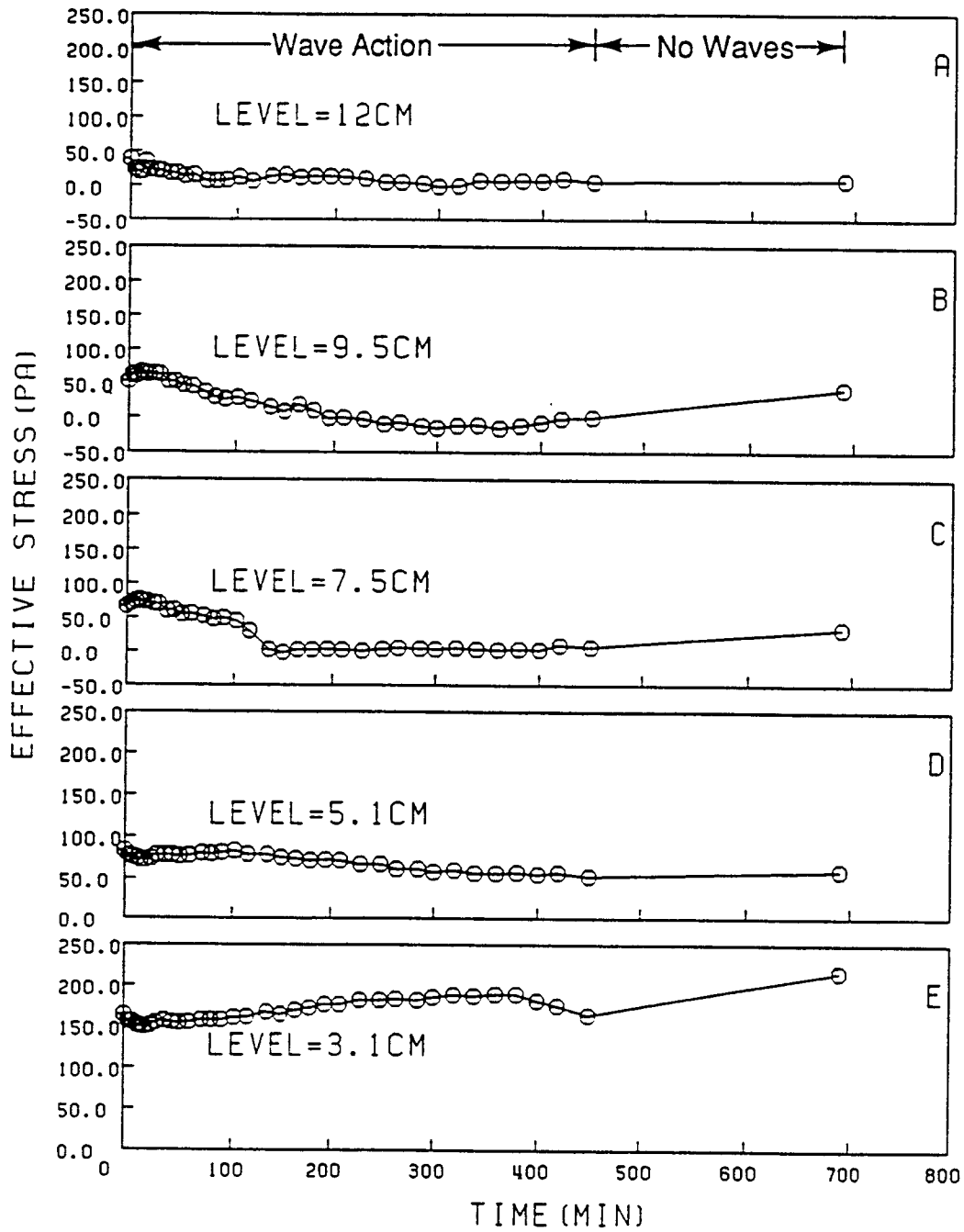
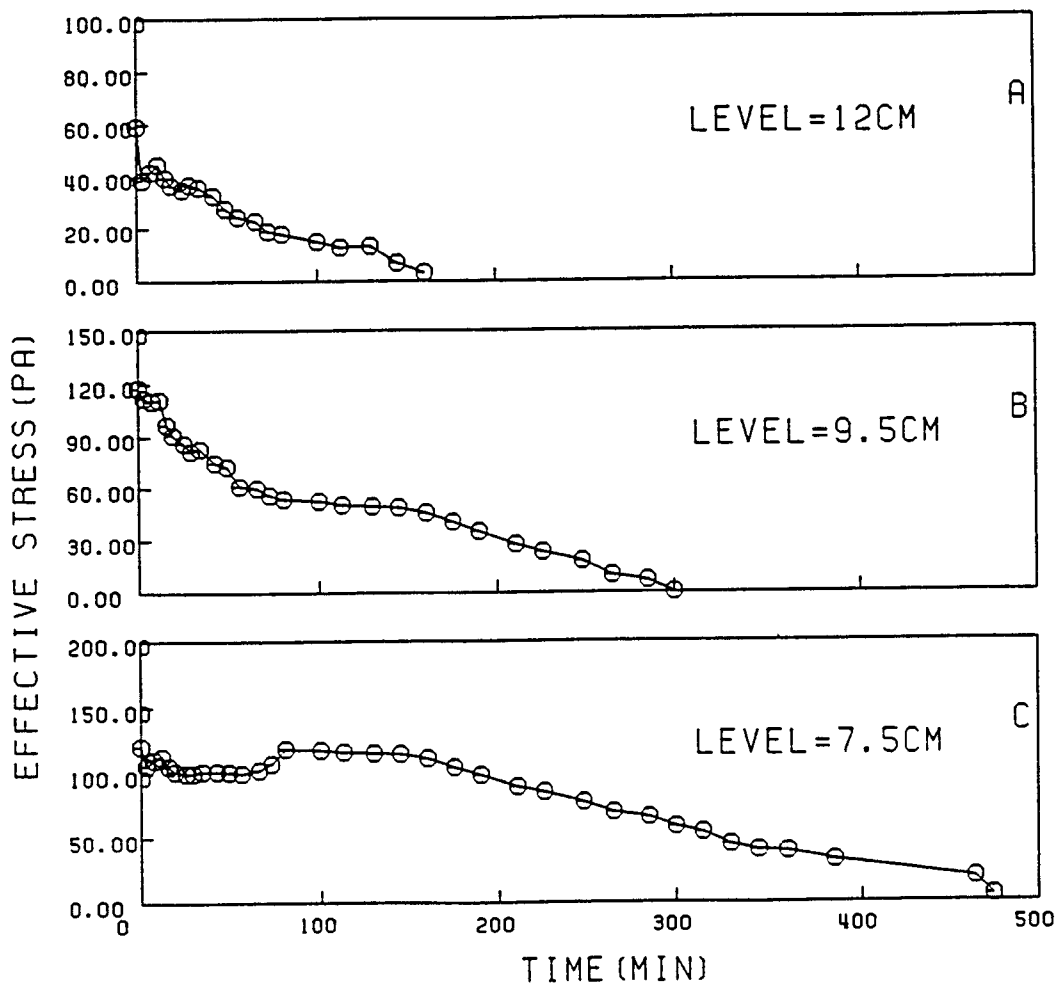


Figure 6.9: Effective stress, σ' , variations with time: Test #9

Table 6.5: Effective stress, σ' , at the beginning and end of Test #9

Elevation(cm)	12.0	9.5	7.5	5.1	3.1
Initial σ' (Pa)	39	53	67	83	163
After waves σ' (Pa)	8	0	7	53	163
Recovered σ' (pa)	8	41	35	59	216

Figure 6.10: Effective stress, σ' , variations with time: Test #10

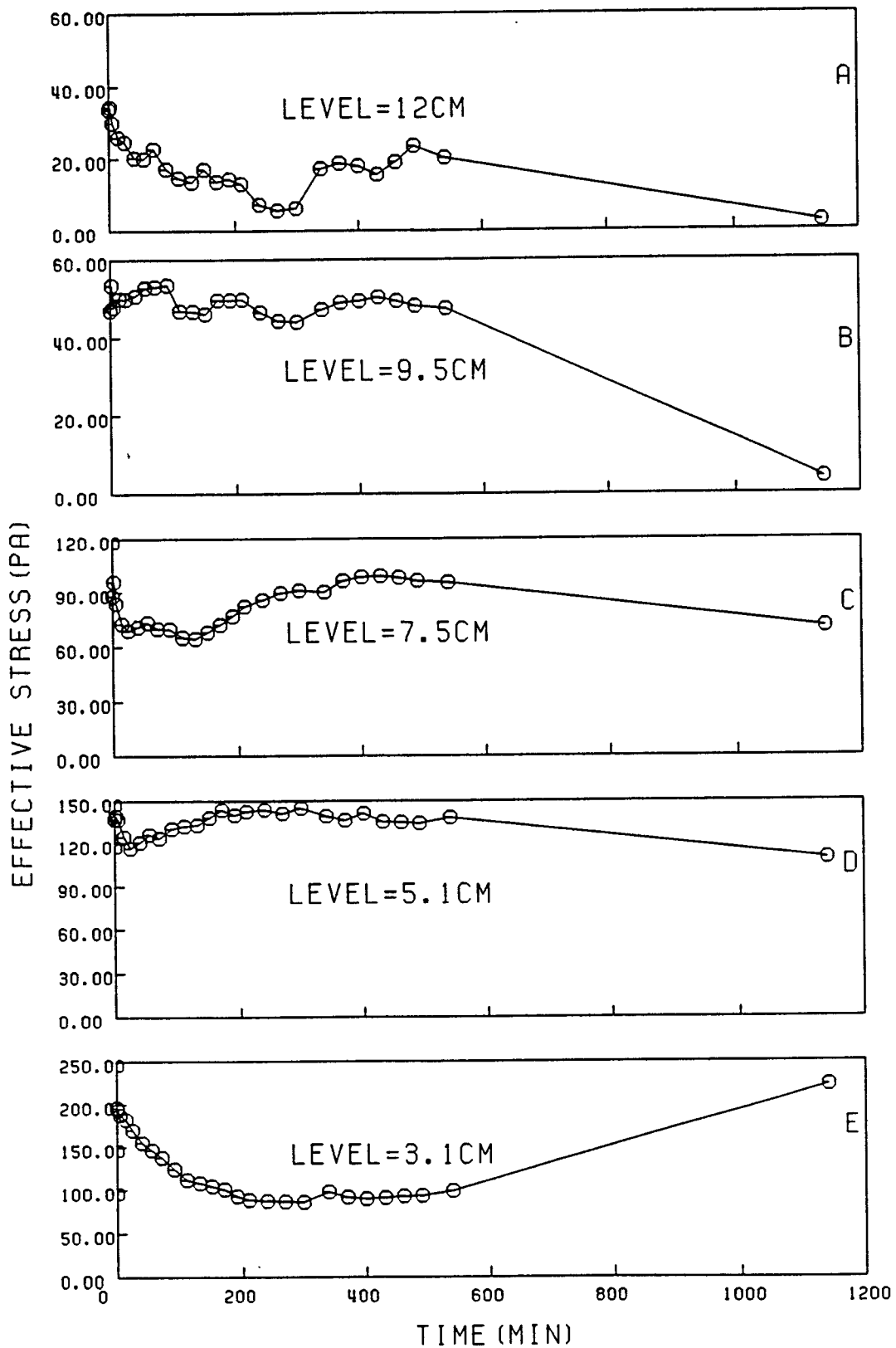


Figure 6.11: Effective stress, σ , variations with time: Test #11

6.3.2 Fluidized Mud Thickness

The level at which the pore water pressure was equal to total pressure, i.e., effective stress $\sigma' = 0$, has been defined as the bed elevation. Above this level a (fluid-supported) fluidized mud layer occurred, whose thickness, d_f , typically increased with continued wave action. In this study $\sigma' = 5Pa$, a relative small value in comparison with the initial values (see Table 6.5), was used to represent the cohesive bed level instead of $\sigma' = 0$ level, which was often difficult to identify, in the σ' versus time plots (Figures 6.8 through 6.11). The time when the bed was just fluidized at each elevation where the pore pressure gauges were located, was found from the effective stress curves, which in turn gave the corresponding bed elevation, H_b , at different times, as shown in Figure 6.12. The water/mud interface is also shown in these figures. At this point it is necessary to explain how the value of time at which fluidization occurred in the test #9 at 7.5cm elevation was obtained. In test #9, the bed at 9.5cm elevation was fluidized at 180 mins, based on this the bed at 7.5cm elevation was assumed fluidized at 360 mins when the effective stress was at its minimum after the time when fluidization occurred at 9.5cm level.

Applying the least squares method to $H_b(t)$ data, the equations for bed elevation as a function of time appear as follows for test #8, #9, #10, and #11, respectively:

$$H_b(t) = 16.6 - 0.0137t + 3.34 \times 10^{-6}t^2 \quad (6.2)$$

$$H_b(t) = 15.5 - 0.0476t + 7.11 \times 10^{-5}t^2 \quad (6.3)$$

$$H_b(t) = 15.0 - 0.0200t + 8.70 \times 10^{-6}t^2 \quad (6.4)$$

$$H_b(t) = 14.8 - 0.0025t \quad (6.5)$$

These functions are shown in Figures 6.12 as dashed lines. The difference between the total mud depth, H_2 and H_b , gives the fluidized thickness, i.e., $d_f(t) = H_2(t) - H_b(t)$, which is plotted in Figure 6.13 and given in Table 6.6. It can be easily seen that during wave action the bed level decreased and the fluidized mud thickness increased.

Generally, a larger wave generated a higher fluidized thickness, as is seen clearly by comparing Figure 6.13(a) (where the design wave height was 4cm; see Table 5.1), (b) (design wave height 5.5cm), and (d) (design wave height 3cm). For the small wave of 3cm height (test #11), the bed elevation decreased from 14.8 to 14.1 cm in 300 mins. When the wave height was 4cm in height, in the same time duration the bed elevation reduced from 16.6 to 12.8cm, and when the wave height increased to 5.5cm, the bed elevation decreased from 15.0 to 7.6cm. The only exception to this trend was test #10 (see Figure 6.13(d), for which the design wave height was 8cm), where in 300 mins for the bed elevation decreased from 15.0 to 9.8cm. This reflected the influence of bed consolidation time. In test #10 the bed consolidation time was 20 hours longer than that in test #9, so that although the wave was higher in test #10 than in test #9, the fluidized mud thickness was smaller. Results from test #8 (Figure 6.13(a)) suggest that at the end of the test, d_f had not attained an equilibrium value. On the other hand, in test #9 (Figure 6.13(b)), which was carried out over the same duration as test #8, d_f is observed to have been approaching a constant value. This contrast between the two tests is consistent with the fact that the wave height in test #9 (5.5cm) was greater than that in test #8 (4cm).

6.3.3 Rate of Fluidization

The bed fluidization rate can be calculated as $\partial H_b / \partial t$, the slope of the curve of bed-elevation versus time shown in Figures 6.12. Taking the derivative of the two equations of the bed elevations, i.e., Equations 6.2, 6.3, 6.4, and 6.5, with respect to the time gives fluidization rates of the beds:

$$\frac{\partial H_b}{\partial t} = 0.0137 - 6.68 \times 10^{-6}t \quad (6.6)$$

$$\frac{\partial H_b}{\partial t} = 0.0476 - 1.42 \times 10^{-4}t \quad (6.7)$$

$$\frac{\partial H_b}{\partial t} = 0.0200 - 1.74 \times 10^{-5}t \quad (6.8)$$

$$\frac{\partial H_b}{\partial t} = 0.00246 \quad (6.9)$$

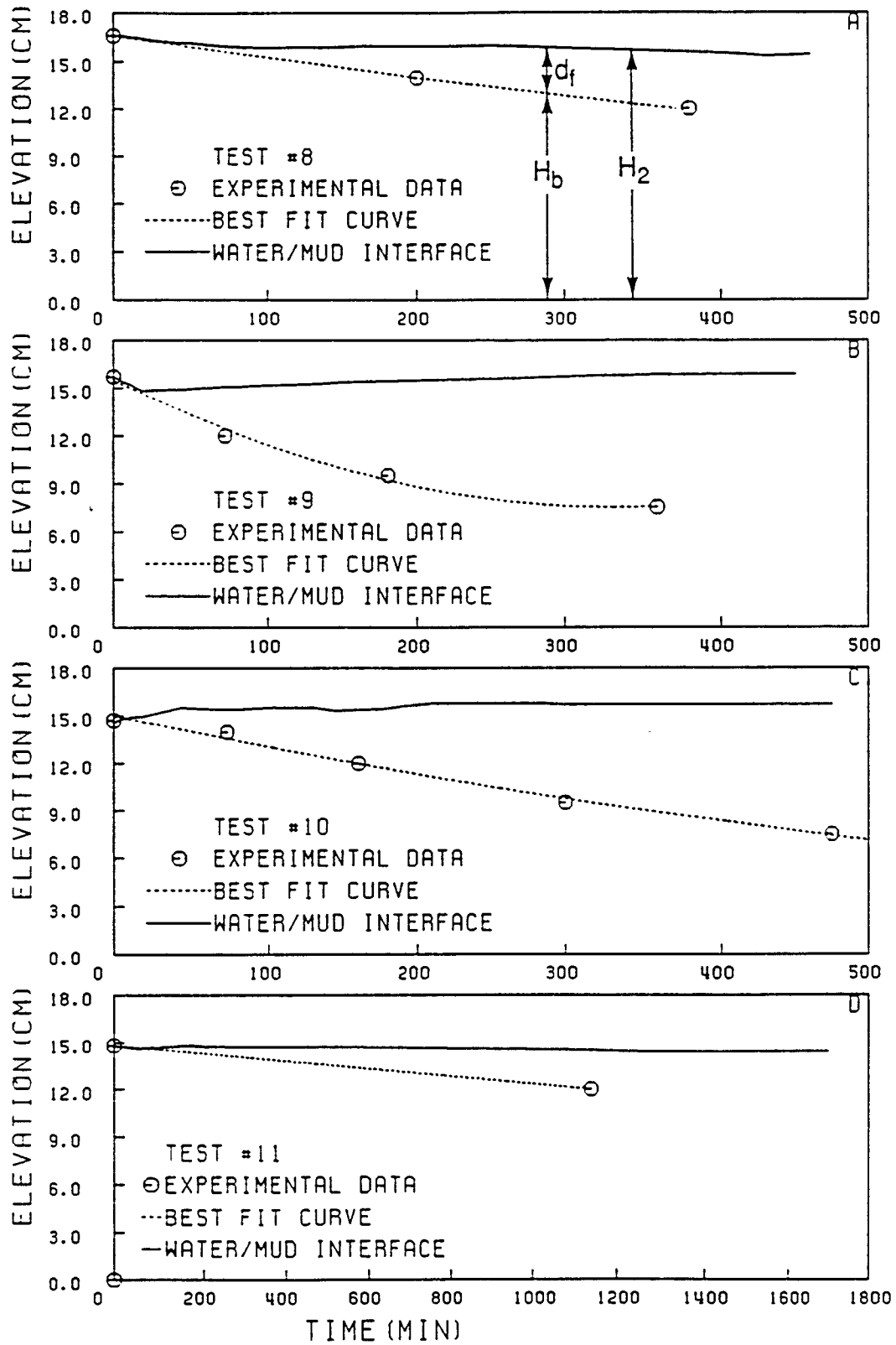


Figure 6.12: Bed elevation, water/mud interface, and fluidized mud thickness in Tests #8 through #11

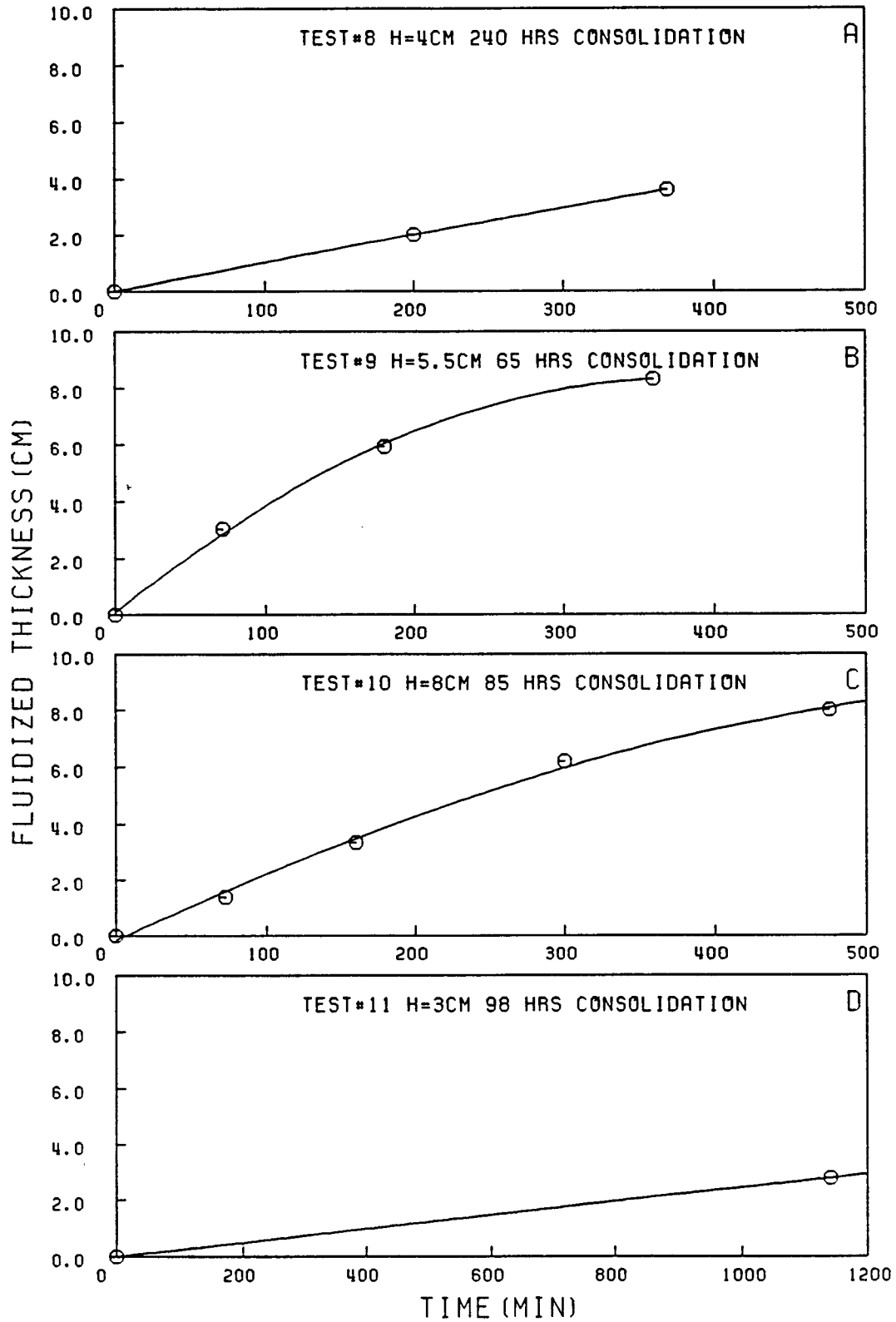


Figure 6.13: Fluidized mud thickness, d_f , variations with time

Table 6.6: Bed elevation and fluidized mud thickness at different times

Test #	Consolidation period (hrs)	Initial density (g/cm^3)	wave height (cm)	time (min)	bed elevation (cm)	fluidized layer thickness (cm)
8	240	1.17	4	0	16.6	0.0
				200	14.0	2.0
				370	12.0	3.6
9	65	1.18	5.5	0	15.7	0.0
				71	12.0	3.05
				180	9.5	5.93
10	85	1.19	8	360	7.5	8.33
				0	14.7	0
				72	14.0	1.4
				160	12.0	3.4
11	90	1.18	3	300	9.5	6.2
				475	7.5	8.0
				0	14.8	0
				1140	12.0	2.8

These relationships are plotted in Figure 6.14.

There are two principal factors that affect the rate of fluidization: the wave height, and the bed consolidation period. By comparing (c) and (d) in Figure 6.14 for which the consolidation periods were approximately the same, it can be seen that the higher wave had a higher fluidization rate, especially at the beginning, which indicates that the larger wave fluidized the bed faster than the smaller one. The effect of consolidation period can be observed by comparing (a) and (b) for which the wave heights were approximately the same. In test #8 in which the bed had been consolidated for 240 hrs, the bed fluidization rate was much smaller than that in test #9. The very high fluidization rate in (b) resulted from the upper layer of the bed which had been softened by the wave already, about 300 mins after wave action began in the two tests. The rate of the fluidization was of the same order in the two tests because the lower part of the bed was in the same state of consolidation in both cases. By comparing test #9 with #10, bed consolidation influence can also be observed, although the wave height in test #10 was much higher than that in test #9.

The rate of fluidization decreased with time in all cases (except in test #11 for which

there were insufficient data to yield any conclusive evidence). At beginning, the fluidization occurred close to the bed surface, so that the wave energy was more concentrated there, which in turn made the bed fluidize faster. As bed fluidized mud thickness increased and fluidization occurred within a thicker mud layer, wave energy was dissipated as it was transmitted downwards, which in turn decreased the fluidization rate.

6.4 Comparison between Model Results and Experiments

6.4.1 Fluidized Mud Thickness, d_f , and Effective Sheared Mud Thickness, d

The measured fluidized mud thickness, d_f , and the model-calculated effective sheared mud thickness, d , are compared in Figure 6.15 to investigate whether d can be a useful representative of d_f . The results indicate a qualitative trend agreement between the two types of thicknesses. Both d_f and d increased under wave action, but d generally increased more rapidly initially than d_f . Two possible causes of the observed discrepancy are as follows. Firstly, the definition of d and its selection as representative of the thickness of fluidized mud layer is to a certain extent an artifact of the scheme for calculating d as presented in Section 4.2. Therefore, there is really no unequivocal justification for comparing d and d_f on physical grounds. On the other hand, however, d and d_f do agree to some extent with the progress of time. Thus comparing calculated d_f as d may not be wholly unjustified. Given this basis, a second cause of discrepancy must be acknowledged. This is due to the selection of the parameters of c , n , and μ_∞ in the mud viscosity model (Equation 4.13). The three parameters used here were for the density of 1.19 g/cm^3 , which was slightly different from the depth-mean mud density in the flume (the depth-mean value been 1.17 or 1.18 g/cm^3 for tests #4 through #11).

The difference in the water wave condition (shallow versus intermediate) between the wave-mud interaction model and the experiments could also account for a part of the discrepancy between d and d_f , as noted in Section 6.2.1. In the model the horizontal velocity at the bottom of the water column was equal to the surface water velocity at the surface ($Z = H_1 + H_2$). However, in reality, the horizontal velocity at the interface in the water

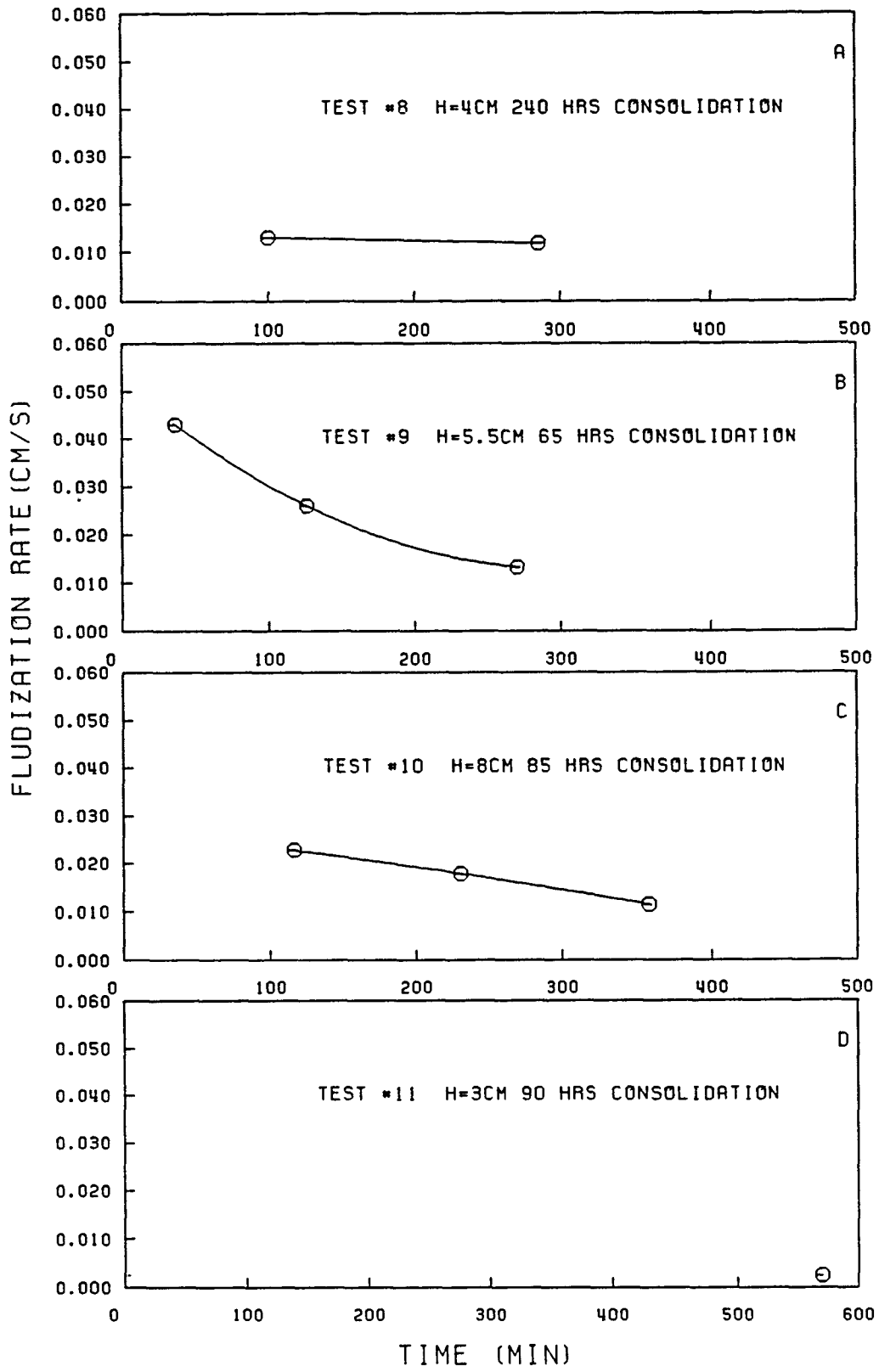


Figure 6.14: Bed fluidization rate, $\partial H_b/\partial t$, versus time

column was smaller than that at the surface due to the intermediate depth as well as the wave boundary layer, hence the horizontal movement at the bed surface was smaller than that obtained from the model. This effect possibly was the cause of $d < d_f$ in general. On the other hand, in the model the vertical acceleration of the fluid particles was assumed to be zero by virtue of the shallow water assumption. The occurrence of vertical motion within the mud matrix would suggest the possibility of more rapid fluidization than in the absence of vertical motion. These two factors oppose each other in terms of their influence on d , hence this limitation would possibly have reduced d relative to d_f , since the shallow water assumption was not quite satisfied.

6.4.2 Fluidization Rate as a Function of Wave Energy Dissipation Rate

Combining the wave energy dissipation rate-time values (Figure 6.6) and the measured bed fluidization rate-time relationships (Equations 6.6 and 6.9) gives the relationship between the bed fluidization rate, $\partial H_b/\partial t$, and the wave energy dissipation rate, ϵ_D . Results from tests #9 and 10 are analyzed. Figure 6.16 shows the best fit curves for test #9 and #10 for the wave energy dissipation-time relationship, where the marker points represent experimental data. The equations of the two curves are as follows:

$$\epsilon_D = 1.52 - 0.0019t - 7.89/t + 1.40 * 10^{-6}t^2 \quad (6.10)$$

$$\epsilon_D = 3.38 - 0.0084t - 6.49/t + 1.20 * 10^{-5}t^2 \quad (6.11)$$

By combining Equations 6.7 and 6.10, and Equations 6.8 and 6.11, the corresponding ϵ_D - t relationships for test #9 and test #10 can be obtained respectively, as shown in Figure 6.17. It is observed that the fluidization rate generally approached zero as ϵ_D decreased. The results indicate that there occurred a depth limit to bed fluidization for the given wave condition, when the fluidization rate equaled zero. The wave energy dissipation rate at that point ($=0.93$ N/m/s and 1.9 N/m/s for tests #9 and #10, respectively) corresponded with the retention of a constant fluidized mud layer in suspension. The higher wave corresponded with a higher wave energy dissipation rate for the same fluidization rate.

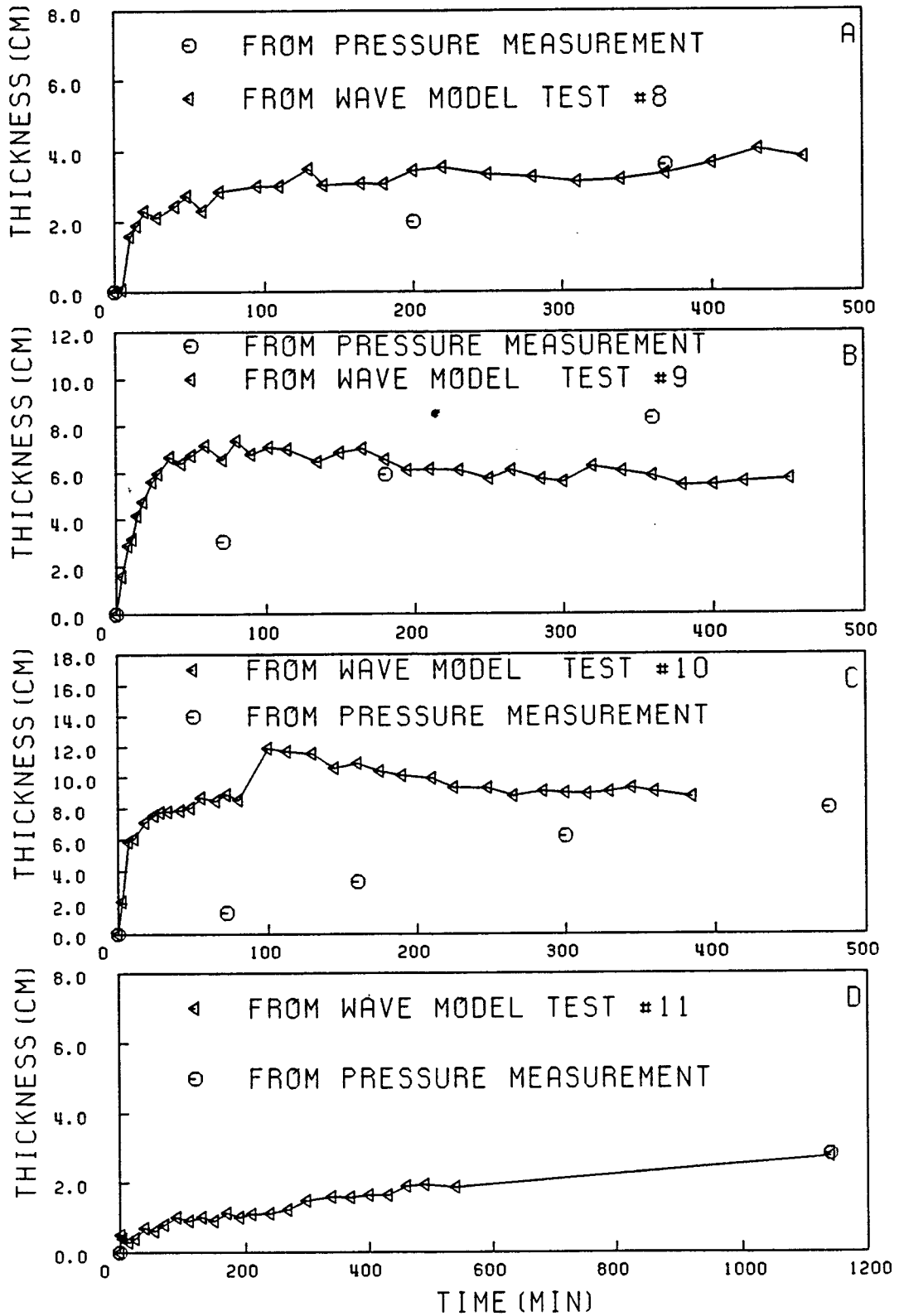


Figure 6.15: Comparison between fluidized mud thickness, d_f , and effective sheared mud thickness, d

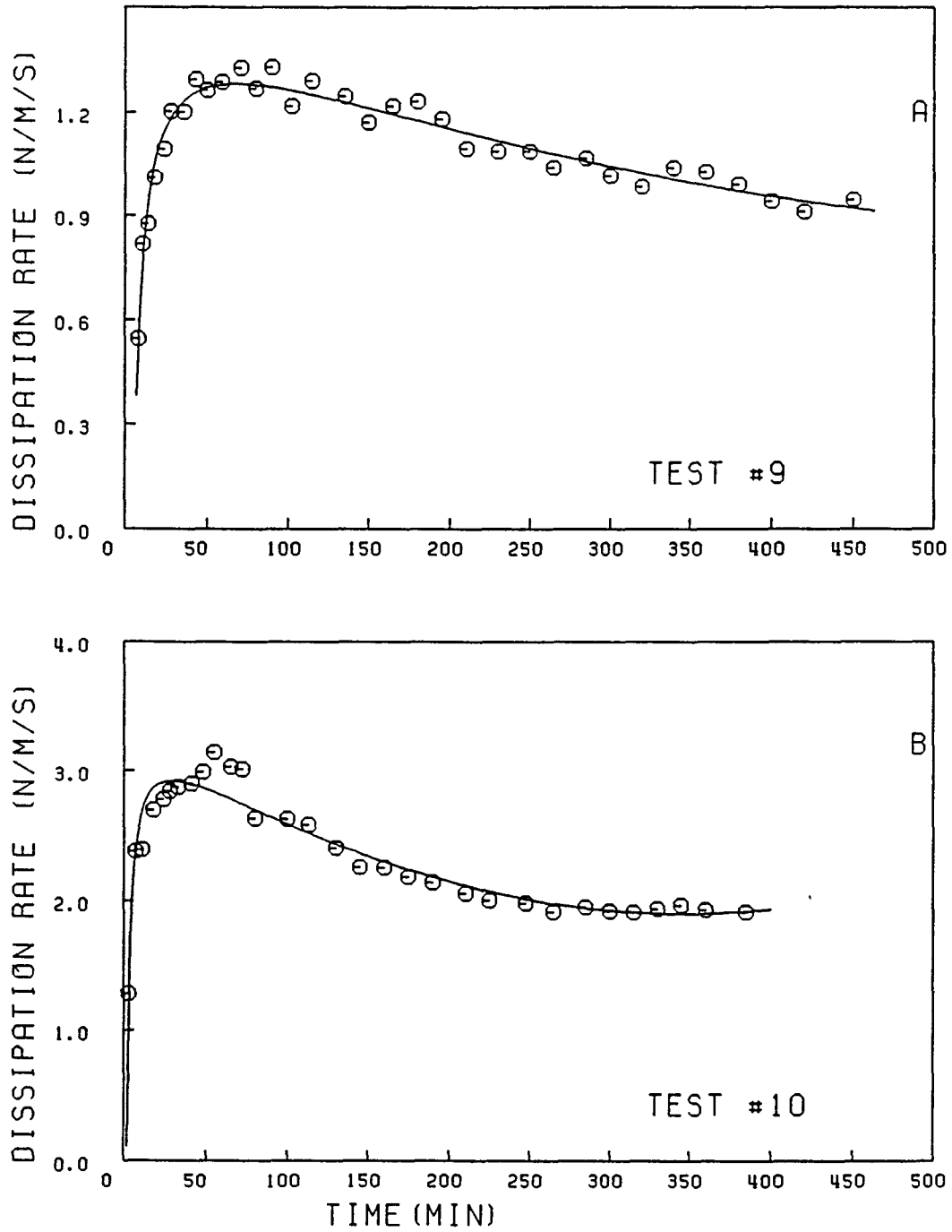


Figure 6.16: Wave energy dissipation rate, ϵ_D , versus time for tests #9 and #10.

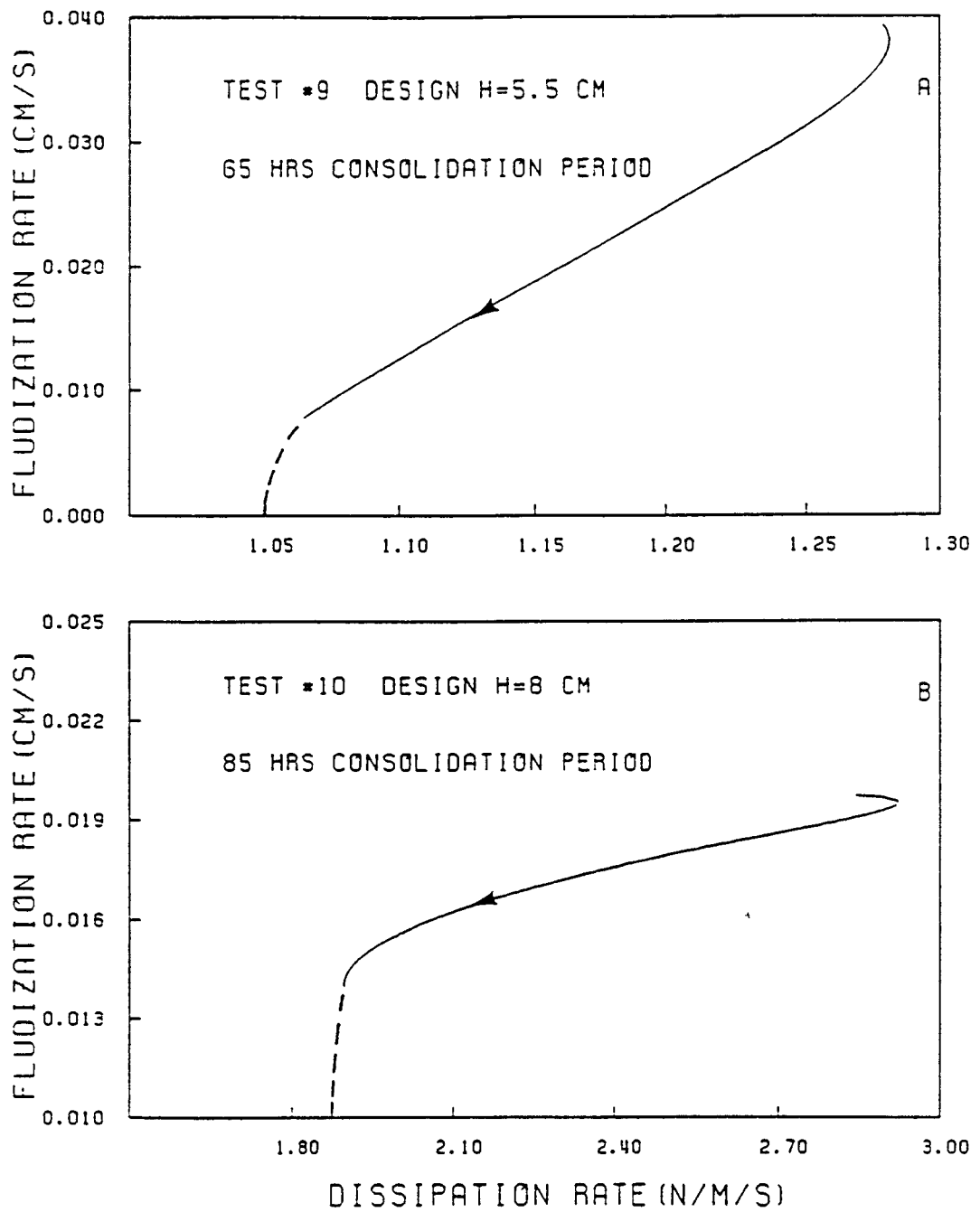


Figure 6.17: Fluidization rate, $\partial H_b / \partial t$, versus wave energy dissipation rate, ϵ_D , tests #9 and #10. Dashed lines indicate extrapolations

CHAPTER 7 CONCLUSIONS

7.1 Conclusions

The following main conclusions from this study are noteworthy:

1. When the water wave traveled over the mud bed, significant wave energy dissipation occurred, primarily due to energy absorption by the bed, which contributed to bed fluidization. The rate and the degree of bed fluidization were dependent on the rate of input of wave energy, hence on the wave height. The larger the wave the faster and more extended was the depth of fluidization.
2. In addition to the wave energy input rate, the time of bed consolidation prior to initiation of wave action was found to be a controlling factor in fluidization. The greater the consolidation the slower the rate of fluidization.
3. During wave action, the pore water pressure typically increased and the effective stress, σ' , decreased. Thus the bed structure was weakened, and when σ' approached zero, fluidization occurred. After wave action ceased, the bed exhibited recovery due to consolidation by losing the excess pore water pressure, thus increasing the effective stress.
4. The rate of bed fluidization gradually decreased with time. During the early stage of wave action the rate of fluidization was higher than at a later time, and eventually approached zero. Thus, although the fluidized mud thickness increased with time initially, there occurred a constant limiting value of the fluidized mud thickness for a given wave condition. This attainment of a steady state condition meant that the rate of energy input equalled the rate of energy dissipation due to viscous dissipation

in the mud, for a given state of the bottom mud consisting of a bed and a fluid mud layer of constant thickness.

5. The rate of wave energy dissipation approached a constant value in many cases. In general, the larger the wave, the higher was this constant value. This observation was consistent with the behavior of the effective sheared mud thickness, a representative fluidized mud thickness, which increased much faster during the early stage of wave action and reached a constant value after a certain time. Also, this constant value generally increased with the input wave energy, for beds of similar consolidation periods.
6. There was an acceptable degree of agreement between the fluidized mud thickness and the effective sheared mud thickness. They both increased with time at a higher rate at the beginning than later, and generally approached constant values, which were in approximate agreement with each other. However, at the beginning the effective sheared mud thickness increased more rapidly than the fluidized thickness. This discrepancy was probably due to of the different definitions of the two types of thicknesses, and the limitations inherent in the hydrodynamic model.
7. For the same fluidization rate, a larger wave corresponded to a higher wave energy dissipation rate for similarly consolidated beds.

7.2 Significance of the Study

Time and resource limitations in this study permitted only a preliminary examination of the complex manner in which the cohesive soil bed is fluidized under wave action. Nevertheless, even though in a limited way, the mechanism by which fluidization proceeds and is eventually sustained by progressive waves has been described in quantitative terms. For a given wave frequency, the effects of wave height and bed consolidation period on the rate of fluidization and the ultimate fluid mud depth have been identified. The basis of this work therefore should allow the development of quantitative procedures for determining the

thickness of the prototype fluid mud layers, e.g., during storm wave action.

An important improvement in methodology required over what was used in this study is in the model for calculating the rate of wave energy dissipation. It is essential that an improved wave-mud interaction model be not restricted to the shallow water condition, and that the viscoelastic properties of mud, as opposed to viscous alone, be represented in an appropriate manner by incorporating an improved rheological description of mud behavior under dynamic loading. Finally it should be noted that a more robust system for measuring the pressures than was available in this study must be incorporated in future experimental design.

BIBLIOGRAPHY

- Cross, M. M. (1965). Rheology of non-Newtonian fluids: A new flow equation for pseudo-plastic systems. *J. Colloid. Sci.*, 20, 417-437.
- Dean, R. G., and Dalrymple, R. A. (1984). Water wave mechanics for engineers and scientists. Prentice-Hall, Inc., Englewood Cliffs, New Jersey, 353pp.
- Goda, Y., and Suzuki, Y. (1976). Estimation of incident and reflected waves in random wave experiments. *Proc. 15th Coastal Engrg. Conf.* ASCE, New York, 828-845.
- Inglis, C. C., and Allen, F. H. (1957). The regimen of the Thames estuary as affected by currents, salinities, and river flow. *Proc. Inst. Civil Engrs.* London, 7, 827-868.
- Jiang, F. and Mehta, J. A. (1991). Some observations on fluid mud response to waves. *In: Dynamics and exchanges in estuaries and the coastal sea.* Prandle, D. (ed), Springer-Verlag, New York, 351-376.
- Kendrick, M. P., and Derbyshire, B. V. (1985). Monitoring of a near-bed turbid layer. *Report SR 44*, Hydraulics Research, Wallingford, United Kingdom. 19pp.
- Krone, R. B. (1962). Flume studies of the transport of sediment in estuarial shoaling processes. *Final Report*, Hydraulic Engineering Laboratory and Sanitary Engineering Research Laboratory, University of California, Berkeley. 118pp.
- Maa, P.-Y. (1986). Erosion of soft mud by waves. Ph.D. Dissertation, University of Florida, Gainesville, 296pp.
- Mehta, A. J. (1989). On estuarine cohesive sediment suspension behavior. *J. Geophys. Resch.*, 94(C10), 14303-14314
- Nichols, M. M. (1985). Fluid mud accumulation process in an estuary. *Geo-Marine Letters*, 4, 171-176.
- Parchure, T. M. (1984). Erosional behavior of deposited cohesive sediments. Ph.D. Dissertation, University of Florida, Gainesville, 321pp.
- Parker, W. R. (1986). On the observation of cohesive sediment behavior for engineering purposes. *In: Estuarine cohesive sediment dynamics.* Mehta, A. J. (ed), Springer-Verlag, Berlin, 270-289.
- Perloff, W. H. and Baron, W. (1976). Soil mechanics: Principles and applications. Ronald Press Company, New York, 724pp.
- Ross, M. A. (1988). Vertical structure of estuarine fine sediment suspensions. Ph.D. Dissertation, University of Florida, Gainesville, 188pp.

- Ross, M. A., Lin, C.-P., and Mehta, A. J. (1987). On the definition of fluid mud. *Proc. Natl. Conf. Hydraulic Engrg.*, ASCE, New York, 231-236.
- Ross, M. A., and Mehta, A. J. (1989). On the mechanics of lutoclines and fluid mud. *J. Coastal Resch.*, SI(5), 51-61.
- Sisko, A. W. (1958). The flow of lubricating greases. *Ind. Eng. Chem.*, 50, 1789-1792.
- Sowers, G. F. (1979). *Introductory soil mechanics and foundations: Geotechnical engineering*. 4th edition, Macmillan, New York, 621pp
- van Rijn, L. C. (1985). The effect of waves on kaolinite/sand beds. *Report M2060*, Delft Hydraulics Laboratory, Delft, The Netherlands. 46pp.
- Wells, J. T. (1983). Dynamics of coastal fluid muds in low-, moderate-, and high tide-range environments. *Can. J. Fisheries and Aquatic Sci.*, 40(suppl. 1), 130-142.
- Wikinson, W. L. (1960). *Non-Newtonian fluids, fluid mechanics, mixing and heat transfer*. Pergamon Press, New York, 138pp.

PART II: *IN-SITU* RHEOMETRY FOR DETERMINING THE DYNAMIC RESPONSE
OF BED

By

David J.A. Williams and P. Rhodri Williams

LIST OF FIGURES

2.1	Shear wave transducer.	3
2.2	Shear wave rig: plan and side views.	4
2.3	Ancillary equipment. Key to figure: 1) PC-AT microcomputer, 2) D/A, A/D and timebase modules, 3) signal outputs to shear wave rig, 4) signal selector from shear wave rig and 5) shear wave rig.	5
3.1	The virtual gap geometry. The virtual gap (width ΔX) is formed by the difference between wave paths of length X_1 and X_2	9
3.2	The determination of V and δ using the virtual gap geometry: curve 1, stress at plate A (calculated); curve 2, displacement of plate A (measured); curve 3, stress at plate C (measured); curve 4, stress at plate B (measured).	9
4.1	Rig pressure response for a water depth of 300 mm, water wave height of 50 mm and (nominal) frequency of 2 Hz.	13
4.2	Spectral analysis (polar FFT) of superposed rheometer responses (shear wave frequency = 1.8 kHz, water wave frequency = 1 Hz, water wave amplitude = 40 mm, and elapsed time under wave loading = 100 seconds). Vertical axis magnitude is arbitrary.	14
4.3	Superposed shear wave signals in the time domain (experimental conditions as in Figure 4.2).	15
6.1	Variations of $G'/G(0)$, $G''/G(0)$ and $V/V(0)$ as functions of δ for the selected rheological model.	20

LIST OF TABLES

5.1	Shear wave velocity V in the presence of 40 mm and 20 mm water waves	18
6.1	Temporal response of sediment to progressive water waves in terms of model parameters	21

CHAPTER 1 INTRODUCTION

1.1 Preamble

The erosion of mud by water waves has a particularly important role in cohesive sediment transport, and the significance of understanding the mechanisms involved in wave-cohesive sediment interaction in coastal and estuarine environments is recognized (Mehta, 1988; 1991). Wave-fluidized cohesive material will, for example, be available for transport by surface erosion combined with tidal currents with self-evident consequences for the transport and distribution of contaminants sorbed on to the constituent particles. Thus an improved understanding of the structural response of cohesive sediment beds to wave action in a range of wave environments is essential if prediction of the likely depth of fluidization is to be made, and a knowledge of cohesive sediment rheology (deformation and flow behavior) is of particular significance in this context.

The viscoelastic nature of concentrated cohesive suspensions and sediments is recognized (James et al., 1988; Williams and Williams, 1989a; 1989b). However, studies of cohesive sediment rheology are complicated by both their non-linear, dissipative, dispersive viscoelastic nature and the limitations of standard rheometric techniques. The latter induce sample disturbance and importantly are unable to recreate *in-situ* stresses particularly in the case of beds undergoing dynamic stressing. This situation is exemplified in the dynamical behavior of a viscoelastic sediment under progressive wave loading in a flume; data from such studies may be unrealistic in terms of bed properties. Rheometric techniques appropriate to the study of the viscoelastic properties of cohesive particulate systems have been identified, and it is demonstrated that the technique of shear wave propagation offers considerable promise in this context (Williams and Williams, 1989a), particularly when utilizing virtual gap geometry (Williams and Williams, 1992).

The design and construction of an *in-situ* rheometer, which utilizes shear wave propagation, and its use in preliminary studies of sediment/wave interaction in a flume are briefly described in the next chapter. This *in-situ* rheometry involves the generation and detection of small amplitude plane shear waves by the piezoelectrically stimulated wave generating/detecting surfaces of transducers. The inability of shear waves to propagate over significant distances in the absence of a volume filling (continuous) structure makes them well suited to studying the wave-induced transition of cohesive sediment bed layers from viscoelastic materials with measurable mechanical rigidity to non-Newtonian shear thinning suspensions of fluid-supported flocs. This allows a rheological parameterization of the point of incipient fluidization of a sediment under wave action and provides a useful adjunct to the work of Ross and Mehta (1989), who identified this structural state with negligible effective stress in a sediment layer. Part I of this report, a study of the influence of waves on the structural state of cohesive soil beds in flumes, specifically sheds light on the relationship between the rate of bed fluidization and the rate of dissipation of wave energy.

For a sediment with a fractional volumetric concentration of solids $\phi \geq \phi_c$, where ϕ_c is the critical volume-filling concentration, the virtual gap rheometer (VGR) utilizes the sensitivity of shear wave velocity to the sediment structure (through mechanical rigidity) and induced strain of the bed due to wave loading. The VGR has physical dimensions which allow its incorporation into flume experiments while causing minimum disturbance of sediment. It operates at frequencies 0(2000 Hz), thereby permitting an evaluation of the (virtually) instantaneous rheological state of the bed when dynamically responding to water waves with frequencies (typically) ca. 1 Hz.

1.2 Investigation

This report provides an account of work done to determine the dynamic response of cohesive sediment bed to progressive wave loading, and provides validation of the *in-situ* rheometric technique. Particular attention is given to the influence of wave height on temporal changes in the dynamical behavior. To this end tests were conducted in a wave flume (see Part I, Table 5.1, for typical test conditions) using regular (monochromatic) waves at 1 Hz (nominal) frequency with heights of 20 mm and 40 mm.

CHAPTER 2 RHEOMETRY

2.1 In-situ Rheometry

As noted in the previous chapter the *in-situ* rheometric techniques used in this work are based upon the generation and detection of small amplitude, high frequency plane shear waves. Shear waves are generated and detected by transducers incorporating piezo-ceramic “bimorph” elements bonded to miniature steel plates which serve as the generating/detecting surfaces (length 12 mm; width 4 mm; thickness 100 μm ; see Fig. 2.1).

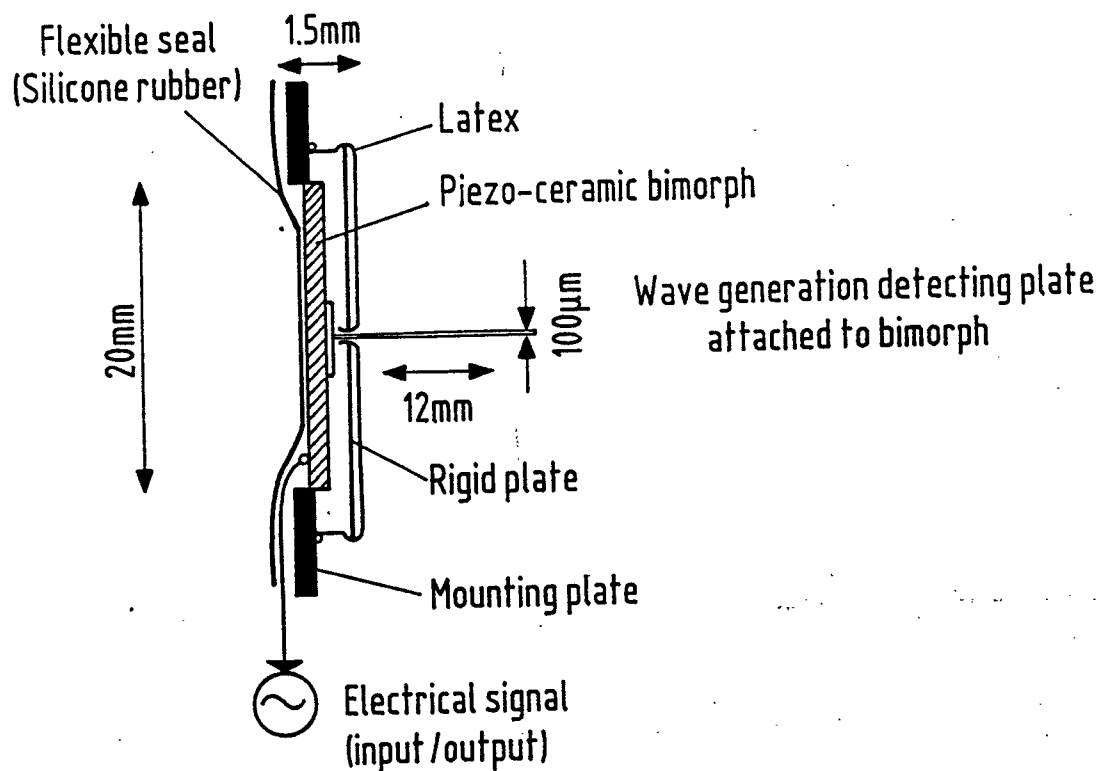


Figure 2.1: Shear wave transducer.

Wave generation is accomplished by exploiting the piezoelectric effect wherein an a.c. voltage at the desired test frequency (typically in the audio range) is applied to the ceramic element whose corresponding deformation causes the desired transverse motion of the attached plate (or wave surface). The shear waves travel in opposite directions along two paths of unequal length to impinge upon, and be reflected by, the wave detecting surfaces. Motion of the latter, induced by shear wave arrivals, produces electrical output signals by the inverse piezoelectric effect. Knowledge of the two physical path lengths (and by difference, of the requisite virtual gap) and phase of wave arrival from the common generating source allows the calculation of shear wave phase velocity V .

2.2 Shear Wave Rig

In the present work three transducers were mounted in series horizontally; two such sets were mounted vertically on the same steel and perspex frame at preset locations above a metal base plate bonded to the wave flume base (Fig. 2.2). The vertical locations were at 23 mm and 53 mm, respectively, above the flume test section base.

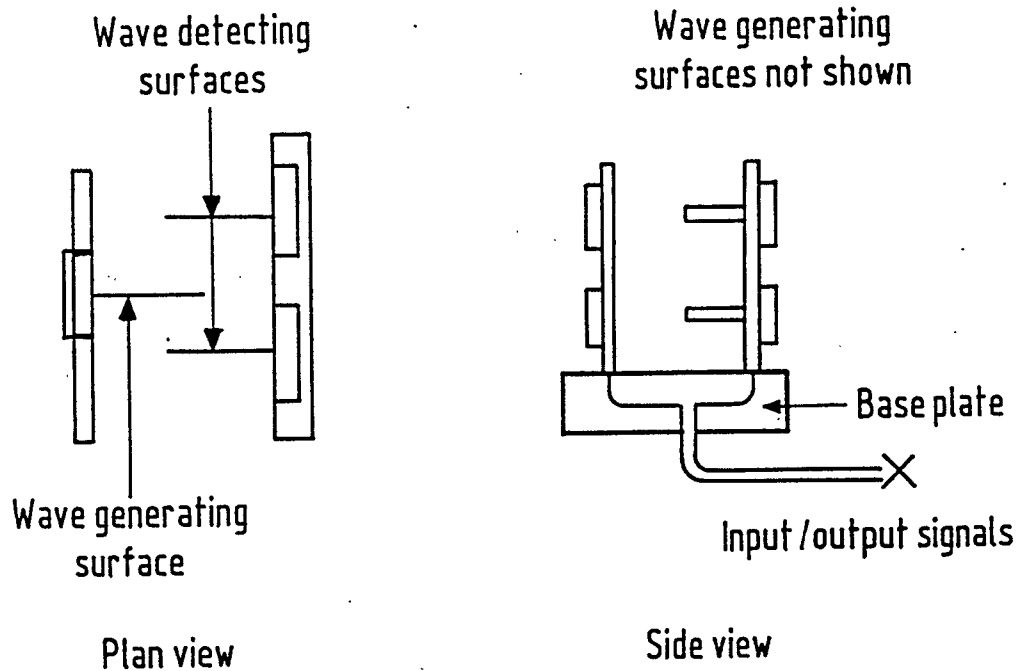


Figure 2.2: Shear wave rig: plan and side views.

Each receiving transducer (Fig. 2.2) has a dual facility in that shear wave detection is accomplished by an element which simultaneously responds to shear wave arrival and dynamic pressure changes in its vicinity within a sediment bed. The resultant transducer output has the form of a (pressure) amplitude-modulated shear wave signal wherein pressure variation and shear wave propagation may be studied separately by Fourier spectral decomposition. These pressure changes may be induced by water wave loading. It is worth noting that the latex covering (shown in Fig. 2.1) is replaced in the case of the generating transducers by a stiff rubber seal to minimize the generation of extraneous acoustic energy in response to the impressed voltages. The transducers thereby allow the direct study of strain induced variation of elastic and dissipative bed properties under a range of pre-erosional dynamic conditions.

2.3 Ancillary Equipment

The equipment used for the generation, detection, recording and analysis of shear waves is shown in Fig. 2.3.

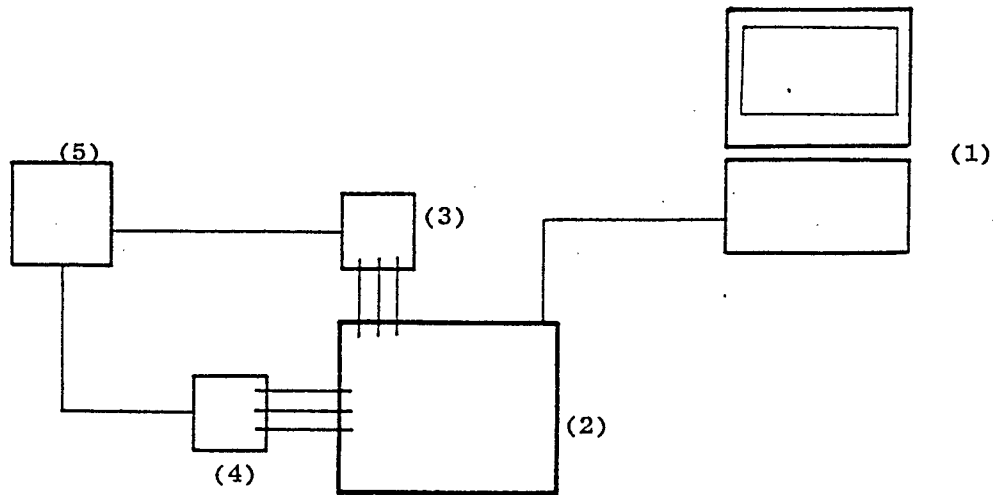


Figure 2.3: Ancillary equipment. Key to figure: 1) PC-AT microcomputer, 2) D/A, A/D and timebase modules, 3) signal outputs to shear wave rig, 4) signal selector from shear wave rig and 5) shear wave rig.

Test wave forms were generated using 1–50 μ sec time steps in a 20 MHz 80286/287–based PC–AT microcomputer, using a digital signal processing program (DADiSPV 2.0, DSP Development Corp., MA) and stored in digital form in a DA 4070, 12–bit, 5 MHz D/A converter with $\pm 10V$ output. The D/A output was fed to the wave–generating transducers under control of a 4010, 10 MHz timebase, triggered by the PC.

Received wave forms, typically in the 0–100 mV range, were stored in 256 KB RAM buffers in 4040, 8 bit, 10 MHz A/D converters (4070 4010 and 4040 supplied in Microlink 4000 Series, Biodata Ltd., U.K.) before being loaded in 8/16 bit integer format into the PC storage (80 MB IDE) for subsequent analysis.

2.4 Signal Processing and Data Analysis

All received test wave forms were analyzed using the following procedures.

Signals were averaged to improve signal to noise ratios before being passed through a highpass (digital) filter with cut–off frequency 160 Hz to eliminate low frequency electrical and mechanical noise (e.g. from the flume wave maker, associated electronics, cooling and lighting systems, etc.) Shear wave velocities were calculated using a Fast Fourier Transform (FFT) based cross–correlation technique (see Brigham, 1988); multiple sequential correlations were performed on selected test signals at 2048, 8192 and 32768 point sample lengths. It is to be noted that the virtual gap technique for shear wave velocity determination is unaffected by convolution of test signals using symmetric filters.

CHAPTER 3
THEORETICAL BASIS

3.1 Definitions of G' and G''

In this discussion, basic knowledge of rheology is assumed. We begin by noting that the x-propagation of a plane shear wave in a viscoelastic medium of density ρ in the x-z spatial domain is governed by the equation of motion:

$$\frac{\partial^2 x}{\partial t^2} = \frac{1}{\rho} \frac{\partial \tau}{\partial z} \quad (3.1)$$

Let the shear stress, $\tau = G^* \gamma$, where γ is the strain and $G^* = G' - iG''$, where G' is the storage modulus (or dynamic rigidity) and G'' is the loss modulus (Barnes et al., 1989). We further note that $G''/G' = \tan \delta$, where δ is the phase angle between τ and γ . Next, since $\gamma = \partial x / \partial z$, Eq. (3.1) can be expressed as

$$\frac{\partial^2 x}{\partial t^2} = \frac{G^*}{\rho} \frac{\partial^2 x}{\partial z^2} \quad (3.2)$$

which is the required shear wave equation. The general solution is

$$x = A_0 \exp(-\Gamma_x) \exp(-i\omega t) \quad (3.3)$$

where A_0 is the wave amplitude at $z=0$, and Γ is the complex wave propagation constant such that

$$\Gamma^2 = -\frac{\rho\omega^2}{G^*} \quad (3.4a)$$

or

$$G^* = -\frac{\rho\omega^2}{\Gamma^2} \quad (3.4b)$$

It is convenient to set

$$\Gamma = k_i + ik_r \quad (3.5)$$

so that

$$x = A_0 \exp(-k_i z) \exp[-i(\omega t + k_r z)] \quad (3.6)$$

where $i = \sqrt{-1}$. From Eq. (3.6) we recognize $k_r = 2\pi/\lambda$ to be the shear wave number ($\lambda =$ shear wave length), and k_i as is the wave attenuation coefficient. Also, $1/k_i$ is the distance in the direction of wave propagation over which the wave amplitude decreases by a factor e .

From Eqs. (3.4a) and (3.5) we have

$$G' = \rho \omega^2 \frac{k_r^2 - k_i^2}{(k_r^2 + k_i^2)^2} \quad (3.7a)$$

$$G'' = \rho \omega^2 \frac{2k_r k_i}{(k_r^2 + k_i^2)^2} \quad (3.7b)$$

Equations (3.7a) and (3.7b) take on simplified forms for special cases, e.g. non-ideal solids (linear viscoelastic materials) with low attenuation, i.e. $k_i/k_r \ll 1$. Then

$$G' = \rho V^2 \quad (3.8a)$$

$$G'' = 2\rho V^2 \frac{k_i}{k_r} \quad (3.8b)$$

where the shear wave phase velocity $V = \omega/k_r$.

Thus for linear viscoelastic systems, G' and G'' may be obtained from Equations (3.7a) and (3.7b) by measurement of k_r and k_i for known test frequency (ω) and sample density (ρ).

3.2 Shear Wave Velocity Determination

For determination of V , let A, B and C be parallel plates in a linear viscoelastic medium (Fig. 3.1). A undergoes continuous forced harmonic displacement in its own plane, generating plane shear waves which travel towards B and C. B and C are at distances X_1 and X_2 from A such that $X_1 > X_2$. Thus a "virtual gap" CB' of width ΔX is created, where $\Delta X = X_1 - X_2$ and $\Delta X \ll X_1, X_2$.

Plates B and C may function as linear force sensing devices with negligible motion (e.g. using piezo-ceramic crystals), producing voltage signals in response to the harmonic motion of A, the common source of shear waves. The displacement of A may be measured (e.g. by a non-contacting displacement transducer). Under steady state conditions, the time varying form of the stress responses at B and C (also harmonic for a linear viscoelastic material) will be as shown in Fig. 3.2.

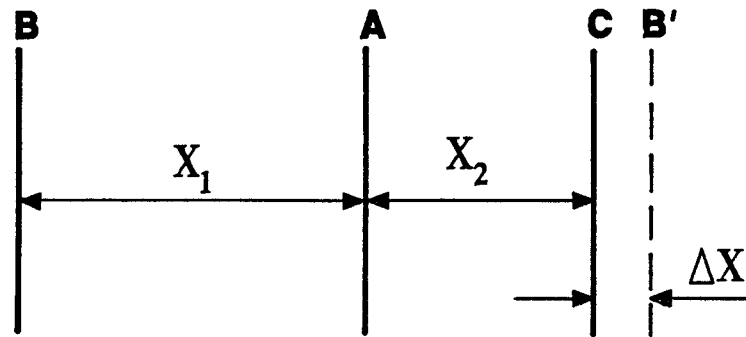


Figure 3.1: The virtual gap geometry. The virtual gap (width ΔX) is formed by the difference between wave paths of length X_1 and X_2 .

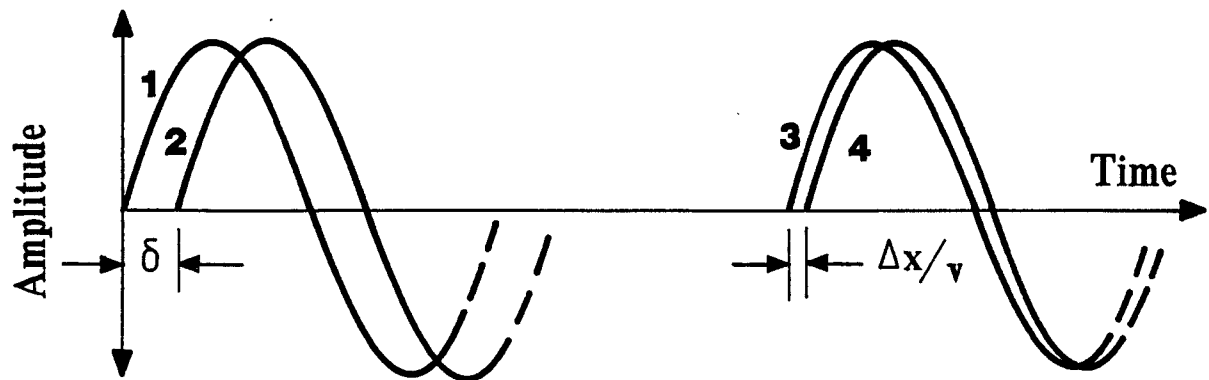


Figure 3.2: The determination of V and δ using the virtual gap geometry: curve 1, stress at plate A (calculated); curve 2, displacement of plate A (measured); curve 3, stress at plate C (measured); curve 4, stress at plate B (measured).

The shear wave phase velocity is given by

$$V = \Delta X \omega / \Phi_1 \quad (3.9)$$

where Φ_1 is the phase angle between curves 3 and 4 (see Fig. 3.2) such that $\lambda = 2\pi \Delta X / \Phi_1$.

3.3 Voigt and Maxwell Models

The rigidity modulus, G' and the loss modulus, G'' , are related in specific ways to the elastic and the viscous components of constitutive rheological models, depending upon the form of the model. The two basic, easy to use models are the Voigt (solid) model and the Maxwell (fluid) model, whose canonical forms are:

Voigt:

$$\tau = G\gamma + \mu\dot{\gamma} \quad (3.10)$$

Maxwell:

$$\tau + \left(\frac{\mu}{G}\right)\dot{\gamma} = \mu\dot{\gamma} \quad (3.11)$$

For the Voigt model it can be shown that

$$G = G' = \rho V^2 \quad (3.12a)$$

$$\mu = \frac{\tan \delta}{\omega} \rho V^2 \quad (3.12b)$$

For the Maxwell model, the relevant relationships are:

$$G' = \frac{G\omega^2\tau^2}{1 + (\omega\tau)^2} \quad (3.13)$$

$$G'' = \frac{G\omega\tau}{1 + (\omega\tau)^2} \quad (3.14)$$

$$\tan \delta = 1/\omega\tau \quad (3.15)$$

where τ is the relaxation time. Further,

$$G = (1 + \tan^2 \delta) \rho V^2 \quad (3.16a)$$

$$\mu = \frac{1 + \tan^2 \delta}{\omega \tan \delta} \rho V^2 \quad (3.16b)$$

Note therefore that for the undisturbed bed, i.e. $\delta = 0$, $G = \rho V^2$, which is the Voigt relationship (Eq. 3.12a).

CHAPTER 4 EXPERIMENTAL CONSIDERATIONS

4.1 Materials

The sediment used in flume tests was an aqueous (50/50 by weight) mixture of a kaolinite and an attapulgite, prepared to give a bulk density ρ of ca. 1380 kg/m³. Details of the physico-chemical characteristics of these clays and their preparation as aqueous slurries are given in Part I, Section 3.1.

4.2 In-situ Rheometry

The rheometer was mounted in the test section of the wave flume approximately 7m downstream of the wave-maker and adjacent to the pressure transducers and density probe tapings (Part I, Fig. 3.18). The rheometer was located 30 mm from the observation wall panel of the flume and its base plate bonded by silicon adhesive to the test section floor. Electrical connections to/from the rheometer were by ribbon cable bonded to the recessed base plate and waterproofed coaxial cables sealed to the side wall of the flume.

4.3 Shear Wave Velocities

Shear wave velocities are reported herein for a vertical section 28 mm above the flume base. As noted previously, shear wave frequency and displacement amplitude of the shear wave generating surface were controlled by a PC-AT microcomputer and Microlink 4000 data acquisition system. Data were stored on sixty 3.5" (1.44 MB) diskettes and subsequently analyzed on a 80486/50 based PC-AT and HP/Apollo 9000.730 workstation using Dadisp v3.0B software.

Shear wave velocity, V , was measured by recording the stress responses caused by impingement and reflection of the continuous shear waves at the receiving surfaces of the

rheometer. The virtual gap configuration of the rheometer (physical wave path lengths of 13.0 mm and 13.1 mm) causes a phase delay between stress responses at the two receiver surfaces from which V is calculated (see Equation 3.9), the virtual gap width being set (fixed) at 100 microns prior to installation in the flume.

All reported velocities were related to the instantaneous peak pressure at each vertical location (under water wave action) in the bed by recording the pressure induced modulation of the shear wave signals (e.g., Fig. 4.1).

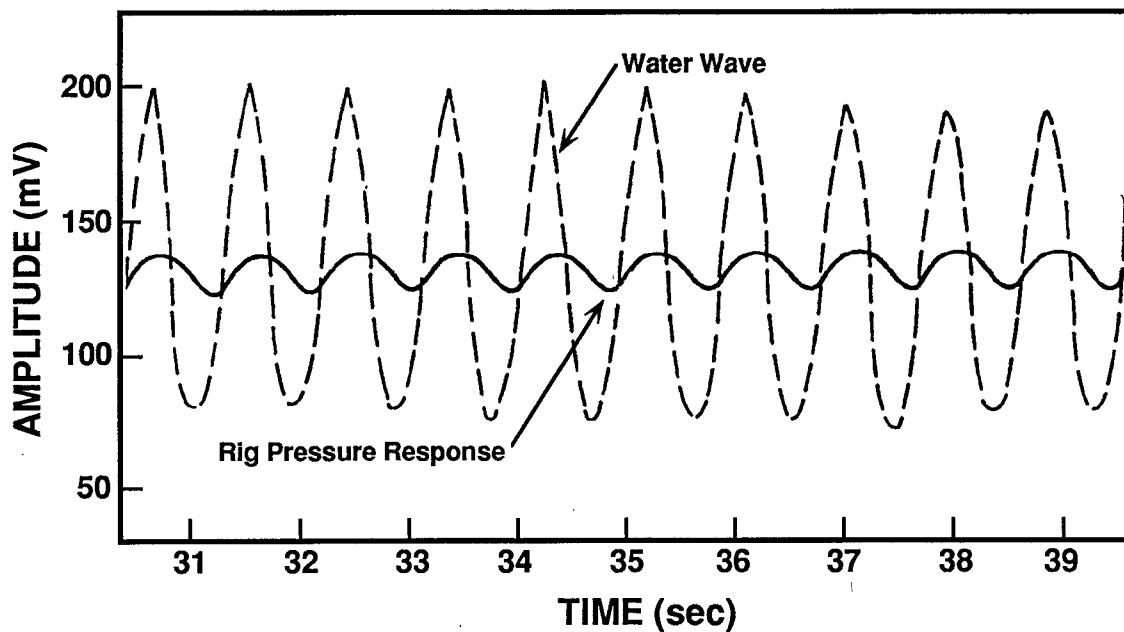


Figure 4.1: Rig pressure response for a water depth of 300 mm, water wave height of 50 mm and (nominal) frequency of 2 Hz.

A spectral analysis (Polar Fast Fourier Transform) of the rheometer response is shown in Fig. 4.2; the superposed shear wave signals (frequency 1.8kHz) are clearly seen and are found to be free of any significant mechanical or electrically generated distortion. By representing the signals in the time-domain the phase delay, Φ_1 , between shear wave arrivals of the spatially separated sensors of the instrument is clearly seen (Fig. 4.3). It should be noted (see Williams and Williams, 1992) that due to the requisite disposition of receiving

surfaces in the partial standing wave field generated by reflection of waves in the rheometer, the stress amplitude of the leading wave (1 in Fig. 4.3) is the smaller despite being closer to the wave-generating surface.

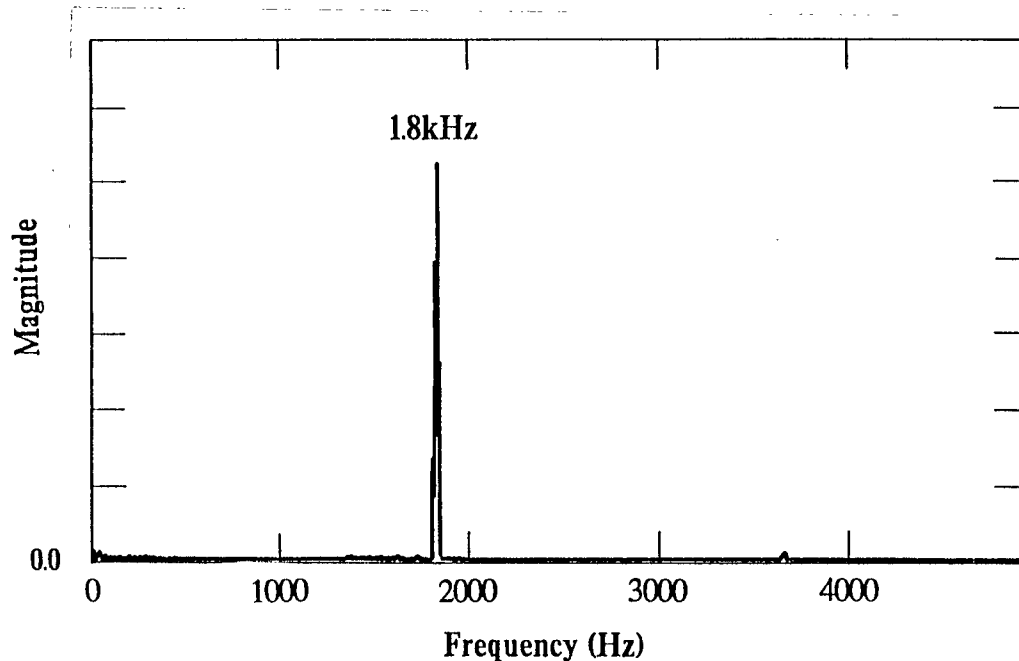


Figure 4.2: Spectral analysis (polar FFT) of superposed rheometer responses (shear wave frequency = 1.8 kHz, water wave frequency = 1 Hz, water wave amplitude = 40 mm, and elapsed time under wave loading = 100 seconds). Vertical axis magnitude is arbitrary.

Stress responses (with D/A output to the wave-generating element in the range 5 to 10 volts) produced a linear viscoelastic response for shear waves propagating in the bed 48 hrs after installation of the rheometer (and in the absence of water waves), the measured shear wave velocity being sensibly independent of shear wave amplitude. Lower voltages produced stress responses with inadequate signal to noise ratio. Cross-correlation of these signals proved unable to resolve phase angle adequately; accordingly all reported velocity measurements were obtained using the maximum D/A output (10 volts) to ensure adequate resolution.

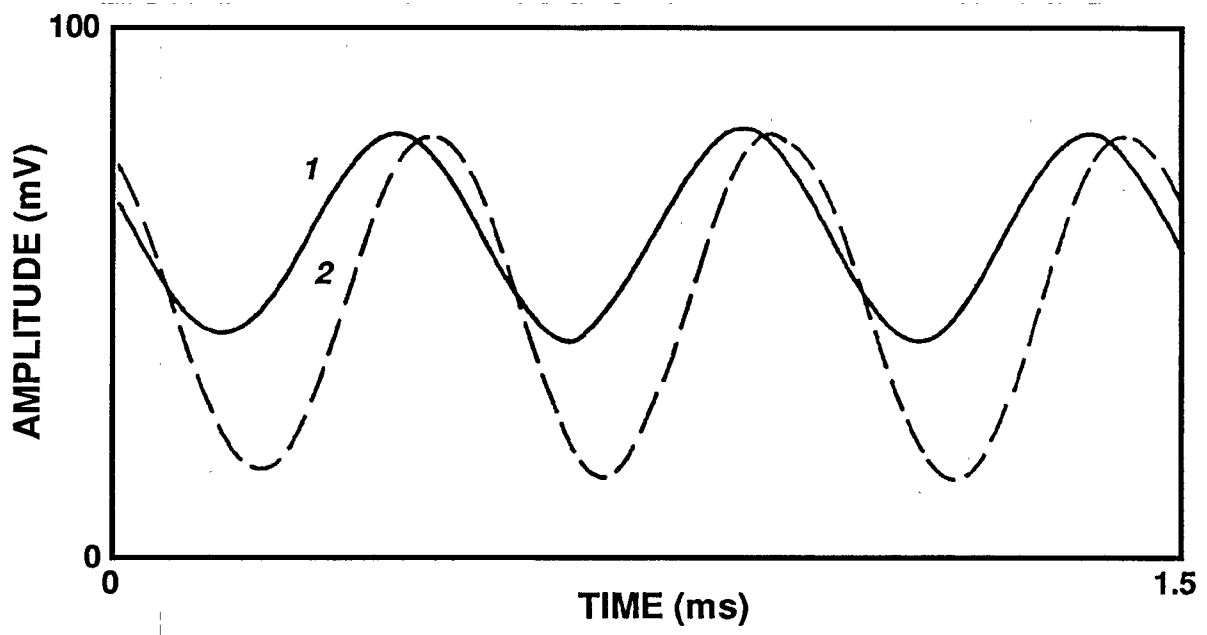


Figure 4.3: Superposed shear wave signals in the time domain (experimental conditions as in Figure 4.2).

CHAPTER 5 FLUME EXPERIMENTS

5.1 Initial Condition

A sediment bed was formed by pouring clay slurry around and over the rheometer to a depth of approximately 200 mm and the sediment allowed to stand undisturbed for 48 hrs with a few mm of overlying flume water. The shear wave velocity determined for this bed after 48 hrs was 3.1 m/s (time delay between wave forms 32 microseconds) giving an apparent bed rigidity (see Equation 3.12a) of ca. 13000 Pa.

This provides a useful estimate of V for this sediment in an “undisturbed” state, i.e. a state not influenced by a history of water wave motion and the concomitant disturbance/modification of bed structure. It is appropriate to assume a Voigt solid response of the bed material in this state. The value of V is of course uniquely determined by the physico-chemical properties of the clay minerals (see Part I), slurry preparation technique and the degree of consolidation achieved by the sediment after 48 hrs. It is of interest to note that the value is typical of concentrated clay suspensions (see Williams and Williams, 1989b).

For tests with water waves the flume was filled with water to a depth of 350 mm (above the base of the flume) and the bed allowed to stand for 16 hrs. Subsequently a series of tests were performed to determine suitable water wave amplitudes for prolonged, systematic studies. The water wave frequency was fixed nominally at 1Hz and two water wave amplitudes (20 mm and 40 mm) were found to provide reasonably linear water waves without causing excessive (visually determined) bed disturbance. When large amplitude (often > 50 mm – 60 mm) waves were employed the bed suffered considerable disruption with significant quantities of sediment appearing in the water column. The rapid disruption of bed structure rendered these wave conditions unsuitable in terms of the study objectives.

5.2 Preliminary Tests with 20 mm Water Waves

A series of tests at 20 mm water wave amplitude were made in which considerable disruption of the bed occurred due to incorrect adjustment wave-maker and which precluded a detailed analysis. However, (for reference) a shear wave velocity of 0.8 m/s was recorded shortly (minutes) after these runs were concluded. This corresponds to an apparent bed rigidity of ca. 1000 Pa., which value is the lowest recorded during this work and apparently corresponds to that of a bed "disturbed" (visually determined) by wave action but which has not undergone subsequent consolidation.

5.3 Tests with 40 mm Water Waves

Twenty hrs after completion of the preliminary tests of Section 5.2, a series of tests were made with 40 mm water waves. This series was begun by recording V in the absence of a water wave (time zero). A phase delay of 49 microseconds gave an apparent bed rigidity of ca. 6000 Pa. (wave velocity 2 m/s), which value is significantly lower than that of 13000 Pa noted previously for an "undisturbed" bed. Subsequently, water waves were generated and V recorded after 100, 1600 and 3600 seconds, respectively. It should be noted that the time required to transfer data from the MICROLINK 4000 memory buffers to the PC-AT precluded more than one measurement at less than 1000 seconds and that the shear wave generator was only activated at the instants of data acquisition.

The decline in shear wave velocity with elapsed time under water wave loading is shown in Table 5.1.

5.4 Tests with 20 mm Water Waves

The tests reported in Section 5.2 were followed by a series of tests with 20 mm water waves. These tests were begun approximately 30 minutes after completion of the runs with 40 mm water waves and as with the latter tests V was initially recorded at time zero. Subsequently V was recorded after 100, 1600 and 3600 seconds, respectively (Table 5.1). No valid data could be obtained from the measurements at 1600 and 3600 seconds, as the signal response from one of the receiver plates appeared too strongly attenuated to analyze

Table 5.1: Shear wave velocity V in the presence of 40 mm and 20 mm water waves

Time under water wave loading (sec)	V (m/sec)	
	40 mm	20 mm
0	2.0	1.4
100	1.8	1.5
1600	1.5	0.8 ^a
3600	1.4	—

^aValue is based on the observations in Section 5.2 and is probably for elapsed time < 1600 sec.

satisfactorily. It should be noted that in these latter measurements the bed in the immediate vicinity of the rheometer was seen to slope appreciably due to withdrawal of sediment for associated (Part I) density measurements. Attempts to measure V at a lower frequency (1 kHz) after 7200 seconds were unsuccessful for the same reason.

CHAPTER 6 ANALYSIS AND DISCUSSION

6.1 Shear Wave Velocity

The results (previous chapter) clearly reveal that the temporal response of a cohesive sediment bed to continuous periodic stressing by progressive water waves is satisfactorily monitored by the use of the continuous shear wave propagation technique. The dynamic response is identified with changes in shear wave velocity, V . To provide further insight into the way in which energy transmitted to the sediment by the water wave is partitioned, it is useful to consider a linear viscoelastic model. We choose the Maxwell model, for which, in the initial undisturbed state ($\delta = 0$), according to Eq. (3.16a),

$$G(0) = \rho V(0)^2 \quad (6.1)$$

where (0) refers to the initial ($t = 0$) state. The rheology of naturally occurring cohesive sediments will undoubtedly demand a more complex model involving a distribution of relaxation times and strengths, which distribution is likely to be a function of time. However, the simple model chosen here captures and illustrates the essential physics of the dynamic processes involved in wave-sediment interaction.

Under wave loading, the rheological characteristics, represented by G' and G'' (Eqs. 3.13 and 3.14), will change relative to those in the initial state. Hence

$$G' = \frac{G(0) \omega^2 \tau^2}{1 + (\omega\tau)^2} \quad (6.2)$$

$$G'' = \frac{G(0)\omega\tau}{1 + (\omega\tau)^2} \quad (6.3)$$

Consequently, from Eq. (3.15)

$$\frac{G'}{G(0)} = \frac{1}{1 + \tan^2 \delta} \quad (6.4)$$

$$\frac{G''}{G(0)} = \frac{\tan \delta}{1 + \tan^2 \delta} \quad (6.5)$$

and note that

$$\frac{G'}{G'} = \tan \delta \quad (6.6)$$

For an elastic material $\delta = 0$, hence $G' = G(0)$ and $G'' = 0$. For $\delta = \pi/4$, $G' = G'' = 0.5G(0)$.

Finally for $\delta = \pi/2$, $G' = G'' = 0$.

$G'/G(0)$, $G''/G(0)$ and $V/V(0)$ are plotted as functions of δ in Figure 6.1, in the range of $0 \leq \delta \leq 90^\circ$ using the following solution procedure for $V/V(0)$:

- (a) Select δ in the range 0° to 90° .
- (b) Generate $G'/G(0)$, $G''/G(0)$ pairs from Eqs. (6.4) and (6.5).
- (c) Obtain k_r/k_i from Eqs. (3.7a,b).
- (d) Solve Eqs. (3.7a) and (6.2) for $V/V(0)$ ¹.

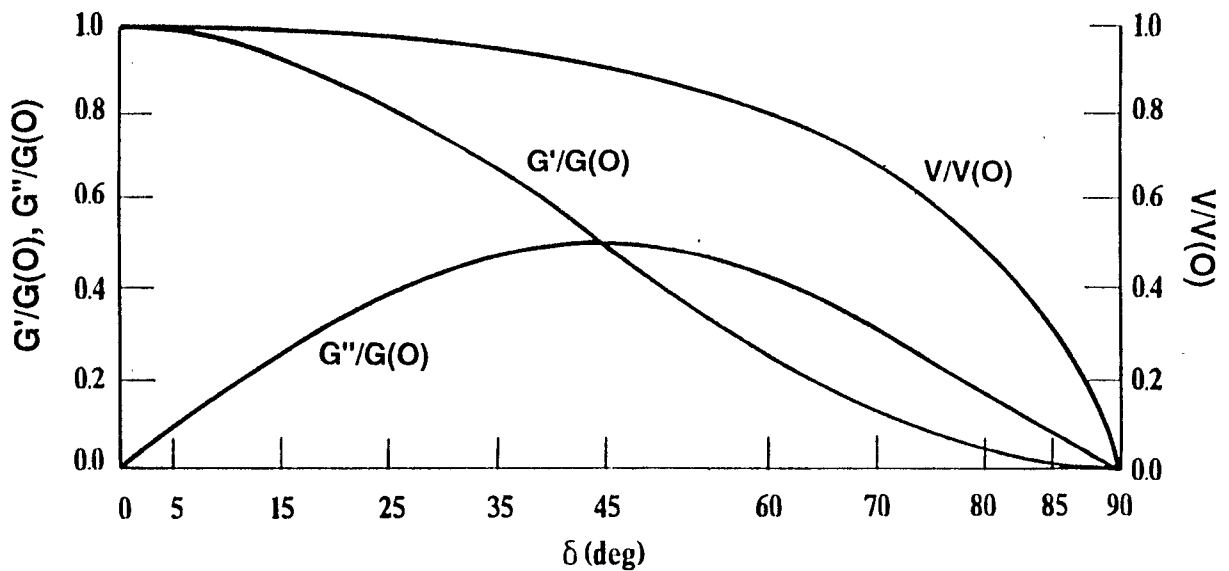


Figure 6.1: Variations of $G'/G(0)$, $G''/G(0)$ and $V/V(0)$ as functions of δ for the selected rheological model.

¹See Appendix for the solution for $V/V(0)$.

Table 6.1: Temporal response of sediment to progressive water waves in terms of model parameters

Elapsed time, t (sec)	$V(t)/V(0)$	δ (deg)	G' (Pa)	G'' (Pa)	G^a (Pa)
(a) 40 mm water waves					
0	1	0	5520	0	5520
100	0.9	45	2760	2760	4471
1600	0.75	67	851	2008	3105
3600	0.7	70	622	1711	2705
(b) 20 mm water waves					
0	0.7	70	622	1711	2705
100	0.75	67	851	2008	3105
1600	0.4	85	42	485	883

$^aG = \rho V^2$, where V is obtained from Table 5.1 and $\rho = 1380 \text{ kg/m}^3$. Values of G other than $G(0) = 5520 \text{ Pa}$ are given for comparative purposes only.

The velocity change $[V/V(0)]$ is less than 9% as δ varies throughout the range $0 < \delta < 45^\circ$. Further, $V/V(0)$ is only about 5% when $G''/G(0)$ has developed 94% of its ultimate maximum value; it is merely 1% when $G''/G(0)$ is $G''(\text{max})/2G(0)$.

This model provides the requisite qualitative features as $G'' = G(0)$ at $\delta = 0$ and $G'' \rightarrow 0$ as $\delta \rightarrow 90^\circ$. The model thus serves to illustrate the more basic features of the range of viscoelastic response which must be considered in wave-sediment interaction and its consequences for *in-situ* rheometry based upon measurements of shear wave velocity.

6.2 Temporal Response of Bed in Terms of Model Parameters

The value of V for $t = 0$ (see Table 5.1) is taken to be $V(0)$, and G', G'' at subsequent times are generated [given $G(0) = 5520 \text{ Pa}$] from $V(t)/V(0)$, the variation of which show interesting features (Table 6.1). It should be noted that for the purposes of model analysis, the runs with 40 mm and 20 mm water waves have been regarded as part of a continuous temporal change in bed properties from a common, initial, undisturbed condition [row 1, Table 6.1 (a)]. Any change in bed rheology in the short interval between the two sets of measurements is neglected.

With elapsed time under wave loading the bed passes through successive rheological states from the initially undisturbed elastic solid [$G' = G(0)$], becoming progressively less elastic but increasingly viscous. Ultimately bed elasticity will practically disappear and the response will become wholly viscous. These analyses identify the transition from a predominantly elastic sediment ($G' > G''$, $0^\circ < \delta < 45^\circ$) to a material in which viscous dissipation of energy is the dominant dynamic process ($G'' > G'$; $45^\circ < \delta < 90^\circ$).

The inadequacy of reliance of velocity determination unaccompanied by attenuation measurement to monitor rheological change is clearly demonstrated by the G value at the bed transition; an apparent decline in shear rigidity of only 19% is indicated (from 5520 Pa at $t = 0$ to 4471 Pa at $t = 100$ sec), whereas G' has actually declined by 50%.

The small changes in V accompanying rheological change highlight the sensitivity of $V(= \sqrt{G/\rho})$ to density changes in beds approaching fluidization. When density information may be difficult to obtain and absolute values of G' , G'' are not required, the measurement of δ will be useful in determining the dynamical state of the bed.

We further consider what useful information might be obtained from velocity measurements in the range $45^\circ < \delta < 90^\circ$ (see Figure 6.1). As $V \rightarrow 0$ ($G' \rightarrow 0$), at the fully fluidized condition, the disappearance of shear rigidity might be taken as an indication of incipient erosional behavior. It is noteworthy that $V/V(0)$ falls to 0.20 to 0.30 for G' in the range of typically reported bed erosion stresses (about 10 Pa). The advisability of using $V = 0$ as a guide to incipient fluidization/pre-erosional behavior may therefore be questionable.

6.3 Concluding Remarks

- 1) The validity (linear response; unambiguous shear wave phase velocity determination; shear wave frequency \gg water wave frequency) and utility of an *in situ* rheometer for monitoring sequential rheological states occasioned by periodic stressing of 1 Hz water waves of moderate amplitude (≤ 40 mm) has been confirmed.
- 2) Analysis of these rheological states in terms of a simple linear viscoelastic model has demonstrated the need for techniques which permit the determination of G' , G'' by

multiple (simultaneous) frequency techniques (currently being developed; see Williams, Williams and Williams, 1992) to be incorporated into future water wave- sediment interaction studies.

BIBLIOGRAPHY

- Barnes H A, Hutton J F and Walters K (1989). *An introduction to rheology*. Elsevier, Amsterdam.
- Brigham E O (1988). *The FFT and its applications*. Prentice-Hall, Englewood Cliffs, NJ.
- James A E, Williams D J A and Williams P R (1988). Small strain, low shear rheometry of cohesive sediments, in *Physical Processes in Estuaries* (Eds. Dronkers, J and W van Leussen), pp. 488-500, Springer-Verlag, Berlin.
- Mehta A J (1988). Laboratory studies on cohesive sediment deposition and erosion, in *Physical Processes in Estuaries* (Eds. Dronkers, J and W van Leussen), pp. 427-445, Springer-Verlag, Berlin.
- Mehta A J (1991). Understanding fluid mud in a dynamic environment, *Geo-Marine Letters*, 11, 113-118.
- Ross M A and Mehta A J (1989). On the mechanics of lutoclines and fluid mud, *J Coastal Research*, Special Issue No. 5, 51-61.
- Williams P R and Williams D J A (1989a). Rheometry for concentrated cohesive suspensions, *J Coastal Research*, Special Issue No. 5, 151-164.
- Williams D J A and Williams P R (1989b). Rheology of concentrated cohesive sediments, *J Coastal Research*, Special Issue No. 5, 165-173.
- Williams P R and Williams D J A (1992). The determination of dynamic moduli at high frequencies, *J Non-Newtonian Fluid Mechanics*, 42, 267-282.
- Williams P R, Williams D J A and Williams R L (1992). Determination of mechanical relaxation spectra of concentrated colloidal dispersions by high frequency rheometry, paper presented at the XIth International Congress on Rheology, Brussels, Belgium. (To be published, Elsevier, Amsterdam).

APPENDIX: SOLUTION FOR $V/V(0)$

From Eqs. (3.7a), (6.1) and (6.4)

$$\left[\frac{V}{V(0)} \right]^2 = \frac{(k_r^2 + k_i^2)^2}{k_r^2(k_r^2 - k_i^2)} \cdot \frac{1}{(1 + \tan^2 \delta)} \quad (\text{A.1})$$

From Eqs. (3.7b), (6.1) and (6.5)

$$\left[\frac{V}{V(0)} \right]^2 = \frac{(k_r^2 + k_i^2)^2}{k_r^2 \cdot 2k_r k_i} \cdot \frac{\tan \delta}{1 + \tan^2 \delta} \quad (\text{A.2})$$

Combining Eqs. (A.1) and (A.2) by eliminating $V/V(0)$ and letting $n = k_i/k_r$

$$n = \frac{-1 \pm \sqrt{1 + \tan \delta}}{\tan \delta} \quad (\text{A.3})$$

in which the '+' solution is realistic. Hence

$$n = \frac{\sqrt{1 + \tan \delta} - 1}{\tan \delta} \quad (\text{A.4})$$

Inserting in Eq. (A.1)

$$\frac{V}{V(0)} = \cos \delta \frac{(1 + n^2)}{\sqrt{1 - n^2}} \quad (\text{A.5})$$

Representative values of $V/V(0)$ are as follows:

δ (deg)	n	$V/V(0)$
0	0	1
$\pi/4$	0.414	0.9
$\pi/2$	0	0